International Journal of Antennas and Propagation

Advanced Antenna Array Development for mm-Wave Communications

Lead Guest Editor: Diego Caratelli
Guest Editors: Bart Smolders, Renato Cicchetti, and Luciano Mescia

Advanced Antenna Array Development for mm-Wave Communications

International Journal of Antennas and Propagation

Advanced Antenna Array Development for mm-Wave Communications

Lead Guest Editor: Diego Caratelli
Guest Editors: Bart Smolders, Renato Cicchetti, and Luciano Mescia

Contents

Hindawi
International Journal of Antennas and Propagation
Volume 2023, Article ID 9831204, 1 page
https://doi.org/10.1155/2023/9831204

Erratum

Erratum to "Miniature Dual-Band Substrate Integrated Waveguide Slotted Antenna Array for Millimeter-Wave 5G Applications"

Fei-Peng Lai, Lu-Wu Chang, and Yen-Sheng Chen

Department of Electronic Engineering, National Taipei University of Technology, Taipei 10608, Taiwan

Correspondence should be addressed to Yen-Sheng Chen; yschen@ntut.edu.tw

Received 16 December 2022; Accepted 16 December 2022; Published 3 February 2023

In the article titled "Miniature Dual-Band Substrate Integrated Waveguide Slotted Antenna Array for Millimeter-Wave 5G Applications" [1], an error in the affiliations was introduced during the production process. The affiliations in the article have been corrected as above.

References

[1] F. P. Lai, L. W. Chang, and Y. S. Chen, "Miniature Dual-Band Substrate Integrated Waveguide Slotted Antenna Array for Millimeter-Wave 5G Applications," *International Journal of Antennas and Propagation*, vol. 2020, Article ID 6478272, 10 pages, 2020.

Hindawi
International Journal of Antennas and Propagation
Volume 2021, Article ID 5514972, 19 pages
https://doi.org/10.1155/2021/5514972

Review Article

A Review of Synthesis Techniques for Phased Antenna Arrays in Wireless Communications and Remote Sensing

Stanislav Ogurtsov,[1] **Diego Caratelli**,[1,2] **and Zhe Song**[1,2]

[1]*Department of Research and Development, The Antenna Company, 5656 AE, Eindhoven, Netherlands*
[2]*Department of Electrical Engineering, Eindhoven University of Technology, 5600 MB, Eindhoven, Netherlands*

Correspondence should be addressed to Diego Caratelli; d.caratelli@tue.nl

Received 15 January 2021; Accepted 1 September 2021; Published 27 September 2021

Academic Editor: Luciano Mescia

Electronically controlled antenna arrays, such as reconfigurable and phased antenna arrays, are essential elements of high-frequency 5G communication hardware. These antenna arrays are aimed at delivering specified communication scenarios and channel characteristics in the mm-wave parts of the 5G spectrum. At the same time, several challenges are associated with the development of such antenna structures, and these challenges mainly originate from their intended mass production, contemporary manufacturing technologies, integration with active RF chains, compact size, dense circuitry, and limitations in postmanufacturing tuning. Consequently, 5G antenna array designers are presented with contradictory design requirements and constraints. Furthermore, these designers need to handle large numbers of designable parameters of the antenna array models, which can be computationally expensive, especially for repetitive and adaptive simulations that are required in design optimization and tuning. Antenna array synthesis, namely, the process of finding positions, orientation, and excitation of the array radiators, is a challenging yet crucial part of antenna array development. This process ensures that the performance requirements of the antenna array are met. Therefore, there is a need for reliable yet fast automated computer-aided design (CAD) and synthesis tools that can support the development of 5G antenna array solutions, from the initial prototyping stage to the final manufacturing tolerance analysis. This paper presents an overview of recent advances in antenna array synthesis from the viewpoint of their applicability to the design of electronically reconfigurable and phased antenna arrays for wireless communications and remote sensing.

1. Introduction

Phased antenna arrays play a pivotal role in the development of upcoming 5G communication systems. Owing to spatial filtering and real-time pattern adaption capabilities, antenna arrays exhibit excellent wireless channel characteristics that are instrumental in achieving high data rates and reliable quality of service, especially in the millimeter-wave frequency range of the 5G spectrum [1–5]. For decades, the phased arrays have been developed as rather bulky, expensive, stationary, or onboard antenna systems for radars, satellite, and cellular wireless communications [6–8].

Recent advances in electromagnetic (EM) computer-aided design (CAD) software [9–12], antenna manufacturing technologies [13–15], solid-state electronics in silicon-based technologies [16–19], millimeter-wave test instrumentation, and computational tools such as graphics processing units, allow for the development and industrialization of compact and cost-effective active phased antenna arrays with integrated electronically controllable beamformers. These products are suitable for 5G applications that are not just associated with base stations of network cells but also with extenders, repeaters, access points, and mobile terminals [1–3]. Each application requires a tailored antenna array performance.

Thus, antenna designers need reliable and versatile array design procedures that can address challenging problems relevant to the synthesis of radiation patterns based on different masks, while handling multiple antenna performance parameters simultaneously, with a reasonable

demand in terms of computational resources and time. Robust techniques should be able to perform syntheses with array models for different levels of complexity, ranging from distributions of isotropic uncoupled radiators to rigorous electromagnetically characterized models of array apertures where antenna mutual coupling effects are properly addressed [20, 21]. The use of a specific antenna array synthesis technique can be maximized by implementing a user-friendly interface and enabling software integration with commonly used electromagnetic computer-aided design (CAD) tools [9–12].

The antenna array synthesis is an automated process of identification or optimization of a specific antenna array model, namely, a procedure for determining the dimensional parameters and the (amplitude and/or phase) excitation tapers across the array aperture and terminals that are useful to meet given performance requirements. This ensures that the performance requirements, associated with the radiation pattern masks, are met in a certain antenna operational state. These requirements are usually essential in instances such as those occurring when pointing the main lobe along a certain direction in transmit (Tx) mode or while enforcing pattern nulls in specific angular sectors in the receive (Rx) mode.

The antenna characteristics considered in the framework of an array synthesis procedure include but are not limited to

- Radiation pattern properties over spatial directions, such as the main lobe half-power beamwidth (HPBW), null-to-null beamwidth, sidelobe level (SLL), grating lobe intensity, and front-to-back ratio (FBR)
- Power-related figures of merit such as peak directivity, gain, total efficiency, effective aperture, and antenna temperature
- Circuital characteristics at the array terminals, such as scattering parameters (input reflection and coupling coefficients) and active (apparent) impedance

Depending on the selected synthesis method or its particular realization, one or a few antenna parameters affect the array design goal function. Other characteristics can be controlled by incorporating specific constraints in the problem formulation. While certain antenna array features, primarily main lobe shape and sidelobe levels, can be evaluated using simple analytical techniques, total efficiency and scattering parameters can only be evaluated using full-wave electromagnetic modeling.

The development, realization, and applications of antenna array synthesis is an expanding research area, and several novel studies have emerged in the technical literature and new dedicated CAD tools have been introduced in the market. Therefore, providing an up-to-date detailed overview of this subject could be a rather ambitious task. Nevertheless, in this study, we have attempted to review the performance of phased antenna arrays in 5G applications through the perspective of an engineer.

2. Iterative Synthesis Methods

2.1. Iterative Fourier Transform Method for Array Pattern Synthesis. Most of contemporary approaches for the numerical synthesis of antenna array patterns are based on the dimensioning of the radiating aperture and evaluation of the excitation tapers through suitable optimization processes. Said approaches are aimed at the minimization of a given objective function that encodes the design specifications and targeted radiation pattern masks. The major differences between optimization procedures can be highlighted through various factors such as the objective function, modeling fidelity, selection of numerical minimization algorithm, and incorporation of design constraints. Both gradient-based and population-based (metaheuristic) optimizers have their own advantages and limitations. Optimizers developed as population-based algorithms are widely used to overcome problems in antenna array synthesis. A different approach for array pattern synthesis is referred to as the iterative Fourier transform (IFT) or iterative fast Fourier transform (IFFT) method. Such technique is rooted in the fundamental relations between antenna array quantities.

The benefits of the IFT method for phased array synthesis were first highlighted in Ref. [22], to the best of our knowledge, as an application of the error reduction algorithm [23]. In Ref. [22], a block diagram of the IFT was presented as it applies to antenna array synthesis. In addition, in Ref. [22], a detailed matrix-vector formulation of the IFT was listed, and it presented criteria for algorithm convergence, which was numerically studied and demonstrated through a power pattern synthesis. This study considered an eight-element linear array with the main lobe directed toward a desired signal and targeted pattern nulling in six discrete directions of jammers of different intensities. In Ref. [22], the potential benefits of the IFT based on two-dimensional discrete Fourier transforms for the synthesis of arbitrarily shaped planar array apertures were discussed.

An illustration of the application of the IFT method to design a synthetic aperture radar (SAR) antenna was given through transmit (Tx) and receive (Rx) pattern syntheses subject to masks concerning the main beam gain ripple, gain slope, and SLLs [24]. Taper syntheses in the short dimension of the SAR antenna were conducted for 48 elements with a separation of 0.7λ, with λ denoting the free-space wavelength. The Tx and Rx patterns were subsequently synthesized with different degrees of freedom (phases for the Tx pattern, amplitudes, and phases with five-bit control for the Rx pattern) to finally generate a two-way pattern of the prescribed characteristics [24].

The similarities between the IFT method and those used for the phase-less synthesis of reflector antennas as well as alternation/successive projection methods have been reported in Ref. [24]. The four essential steps of the IFT method were outlined in Ref. [24], unfortunately without a proper description of the implementation details, in particular, those related to pattern adaptation. The IFT method was further developed to solve synthesis problems of large phased planar arrays [25]. In fact, the IFT (IFFT) method

was specifically developed to handle typical sizes, aperture shapes, requirements, operation modes, and underlying EM interactions of large naval and military phased arrays.

The IFT method is based on the fact that the array factor (AF) and excitation taper are related to each other through a truncated series of direct and inverse Fourier transforms, respectively. A direct Fourier transform (FT) performed on the AF simultaneously produces all the entries of the excitation taper. An inverse FT performed on the excitation taper simultaneously produces AF values for sampled direction cosines [25]. These two stages are performed sequentially and iteratively using fast Fourier transforms (FFTs) with the adaptation of the newly computed data sets to the enforced requirements and design constraints (AF pattern masks, amplitude-only or phase-only taper, and on/off-element state) before being used as the input to the following stage. Only the excitation coefficients corresponding to the grid of the array elements are supplied to the inverse FFT at each iteration. A block diagram of the IFT algorithm is presented in Figure 1.

The IFT method is outlined as follows. The AF of a planar antenna with a rectangular aperture can be defined as a truncated double series of a two-dimensional discrete inverse FT [25]:

$$\mathrm{AF}(u,v) = \sum_{m=0}^{M-1}\sum_{n=0}^{N-1} a_{mn} e^{j2\pi\left(ms_x u + ns_y v\right)}, \tag{1}$$

where $u = \sin\theta\cos\phi$, $v = \sin\theta\sin\phi$, s_x and s_y are, respectively, the x- and y-directional uniform element spacings normalized to the free-space wavelength λ, a_{mn} is the excitation taper entries, and M and N are the number of elements in the x- and y-directions, respectively. The AF is a periodic function of the direction cosines with the u- and v-periods determined by the array element spacings as $-0.5/s_x < u < 0.5/s_x$ and $-0.5/s_y < v < 0.5/s_y$, respectively. Thus, relevant information about the AF can be retrieved by sampling over the rectangle of the direction cosines. For element spacings smaller than a half-wavelength, the AF extends to the invisible space of the direction cosines. At the same time, a part of the (u,v)- direction resides out of the visible space. Therefore, the AF extension into the invisible space must be included in the calculation of the excitation taper entries using direct FFT to avoid degradation of sidelobe characteristics in the process of beam scanning and/or raising of the operating frequency [25].

The IFT method is successfully applied to the synthesis of low-SLL patterns. The first step is the calculation of the AF along the K^2 far-field directions using an initial excitation taper for a given array aperture with $M \times N$ elements. Any excitation taper that causes a reasonably shaped main lobe can be used as the initial one. Subsequently, the pattern of the calculated AF is compared with that of the pattern mask. The AF pattern values above the sidelobe mask are reduced in amplitude to match the mask levels. The AF values below the mask levels and those corresponding to the main lobe remain unaltered. Subsequently, the AF dataset corrected in this way is provided as the input to the direct FFT, which yields the updated excitation taper for the next iteration. The

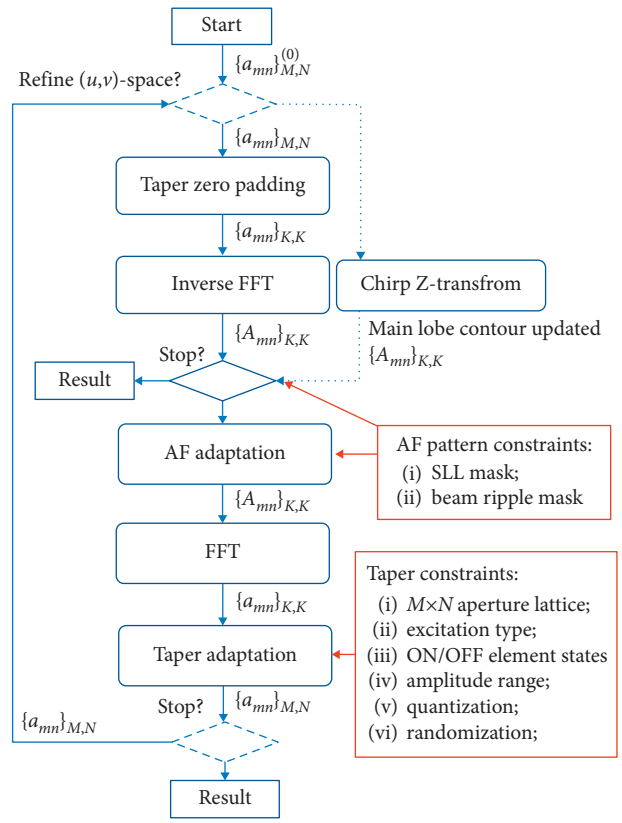

Figure 1: Diagram of the error reduction algorithm [22–24] and IFT method [25–35] as applied to planar phased antenna array synthesis.

updated excitation taper has K^2 entries, although only $M \times N$ of those actually populate the array aperture. The excessive entries should be removed, and iterations should be continued if a complex-valued taper is allowed. If the required pattern characteristics are to be achieved by means of an amplitude-only or phase-only synthesis, the excess information (e.g., computed phase values in the amplitude-only synthesis or nonuniform amplitudes in the phase-only synthesis) is restored to the initial values before proceeding to the next iteration.

Because the main lobe contour, which is corresponding to the first nulls, typically widens as the sidelobes decrease from iteration to iteration, there might be a need to recalculate the main lobe contour repeatedly and with high accuracy, that is, with a refined sampling of the (u,v)-space. A two-dimensional chirp Z-transform can serve as an effective solution to overcome the aforementioned problems [25]. The violations of the sidelobe mask and/or the power content of the excitation taper outside the array aperture are typically used for convergence monitoring and/or termination criteria.

The IFT method is also applicable to triangular array lattices upon affine transformation mapping the original grid onto a suitable Cartesian one [26, 36]. The effectiveness and robustness of the IFT method, along with its ability to synthesize, at very modest computational costs, ultra-low sidelobe sum, and difference patterns for array apertures of

various shapes and comprising a very large number of elements have been demonstrated in various examples [25, 26]. A few examples of the amplitude-only synthesis of ultra-low sidelobe (better than −71 dB) sum and difference patterns for circular and elliptical array apertures with triangular lattices comprising 5797 and 5509 elements, respectively, have been reported in Ref. [25]. Examples of the achieved pseudocontour patterns are shown in Figure 2.

Here, the computational burden and quality of the results for array apertures of different sizes have been studied for different sidelobe requirements, including additional ring-level sidelobe masks with amplitude-only synthesized tapers and nulling sectors with complex excitation tapers. It has been reported that patterns with SLLs smaller than −81 dB were synthesized in 20 minutes and patterns with sidelobes below −61 dB were obtained in just a few minutes. The synthesis was carried out on a PC with an Intel Pentium 4 processor with 1 MB L2 cache operating at 2.8 GHz and equipped with 512 MB RAM.

The IFT method can effectively alleviate the gain and SLL degradation in ultra-low sidelobe sum and difference patterns caused by array element failures (up to 30% of array elements). This has been demonstrated through numerical examples of a circular X-band 5800-element array where failed elements were randomly selected across the aperture [27]. It is worth noting that such compensation synthesis can be carried out on conventional laptop computers in relatively short computational times [27].

Another useful application of the IFT method is the synthesis of thinned linear arrays featuring minimal SLLs [28]. Thinning synthesis was performed by setting the amplitudes of the elements with the highest intensity to those with respect to the predefined filling factor (FL) and by setting the amplitudes of other elements to zero during each iteration between the two FFT stages [28]. The fast computational speed (owing to the use of forward and backward FFT) enabled a large number of trials starting with random initializations, for example, 10000 [28], to find the global optimum in terms of SLLs for a given aperture size and FL. The method has been successfully applied to planar half-wavelength-spaced circular apertures with extensions from 25 to 100 wavelengths and subject to 30 and 40% FLs [29], as illustrated in Figure 3. The IFT method shows similar and even lower SLLs, as shown in Table 1 [29], as compared to the statistical density taper approach [37], while the former technique yielded results in a few minutes per case and with 50 trials for each case.

In a recent study, thinning with amplitude tapering syntheses were performed for large circular array apertures (up to approximately 133 wavelengths), which were capable of sum (with 10 dB dynamic range for the synthesized amplitudes) and difference (with 15 dB dynamic range for the synthesized amplitudes) low-sidelobe patterns with and without the addition of nulling sectors [30], as depicted in Figure 4. It should be noted that the difference pattern syntheses of thinned planar array apertures were reported in scientific literature for the first time in Ref. [30].

A significant benefit of the IFT method for array synthesis problems is the ease of implementation owing to the adoption of well-established computational routines and programming environments [31]. Furthermore, the IFT method is at the core of the commercially available specialized environment for the design and analysis of phased array antennas, APAS [38].

A hybrid IFT and taper density technique [39], termed the IFT density taper (IFTDT) technique, is used for thinning of square and circular arrays [40]. In the IFTDT, the IFT method is used to identify the optimal locations of the active (ON) array elements within every aperture ring while minimizing the SLLs [40].

To prevent degradation of the synthesized array pattern in the process of beam scanning not only at the frequency of synthesis but also at higher frequencies, the SLL requirements have to be enforced upon visible and invisible spaces. The synthesis of scan- and frequency-invariant linear and planar arrays featuring ultra-low SLLs using the IFT method has been explained in Ref. [32]. A useful formula based on the FT shift and scale properties, which is applicable to aperiodic lattice arrays, has been presented in ref. [32]. This formula defines the (u, v)-region to perform a scan and frequency robust syntheses:

$$u^2 + v^2 \leq (1 + \sin\theta_m)^2 \left(\frac{f_h}{f_0}\right)^2, \tag{2}$$

where θ_m is the targeted maximum scan angle, f_h is the highest operating frequency, and f_0 is the synthesis frequency. Formula (2) extends the region of the direction cosines to perform the taper synthesis by including the part of invisible space which enters visible space when the main beam is scanned to the maximum scan angle and/or the frequency is increased to the highest operation frequency [32].

A randomization of quantization errors was included in the IFT iterations that performed linear array amplitude-only and phase-only syntheses. This approach was capable of alleviating SLL degradation due to the amplitude and phase quantization introduced by discrete control components of beamforming chains [33].

The IFT method does not account for the mutual coupling effects between antennas [25–33, 38, 39]. On the other hand, it has been concluded that, in planar arrays with 2000 and more elements, mutual coupling corrupts SLLs and other pattern characteristics only to a limited, acceptable, and often negligible extent [34, 35]. Therefore, IFT syntheses are reliable when applied to large apertures (>2000 elements). At the same time, the impact of coupling becomes more apparent as the number of array elements decreases. In particular, it has been observed on the IFT synthesis results that SLLs lower than −45 dB cannot be realized for arrays comprising less than 500 elements if mutual coupling effects are neglected [34].

2.2. Iterative Matrix Inversion Approach for Array Factor Pattern Synthesis. Another iterative approach for linear array pattern synthesis was proposed in Ref. [41]. This approach is similar to the IFT method with respect to the

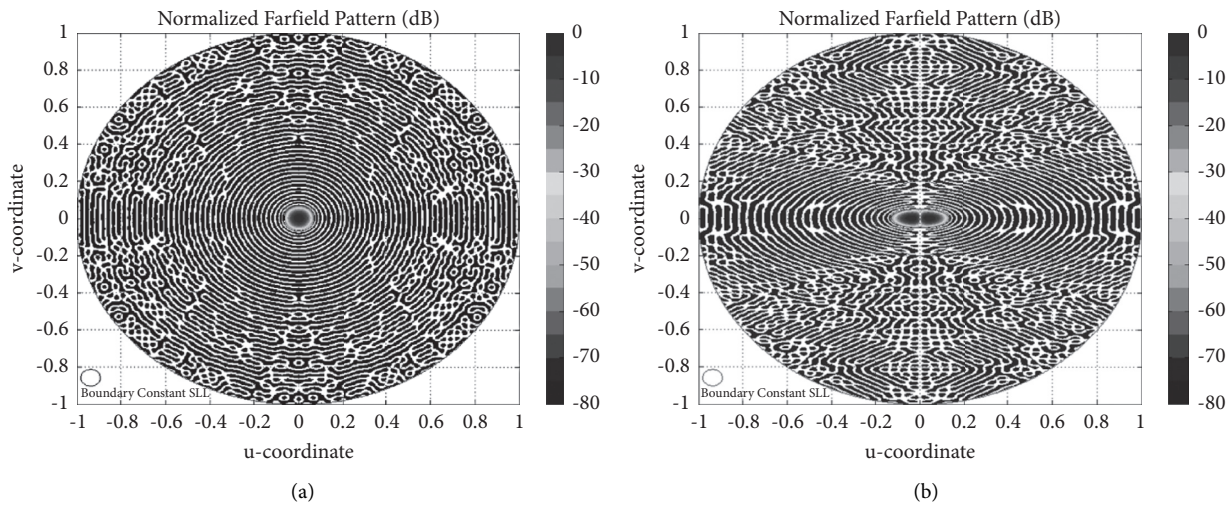

Figure 2: Pseudocontour plots [25]: (a) sum pattern of a 1.3 m circular array with 5797 elements operating at 10 GHz; (b) azimuth difference pattern of a 1.9 m × 1.3 m elliptical aperture with 5509 elements operating at 10 GHz. Both patterns, obtained through amplitude-only IFT synthesis, feature a SLL of −71 dB. The array elements are arranged in a triangular grid.

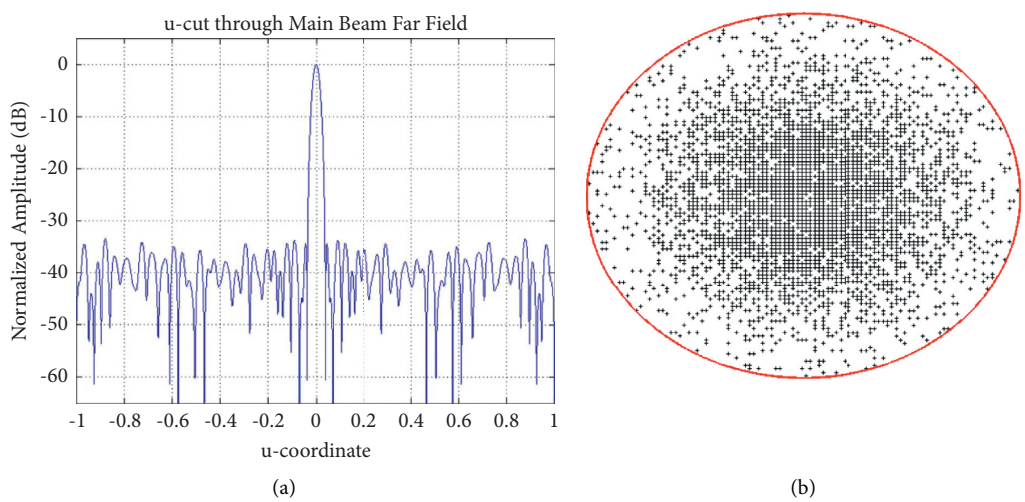

Figure 3: A thinned circular aperture array having a diameter of 50λ and based on a 0.5λ spaced square grid with 40% FL. The IFT synthesis results [29]: (a) pattern cut; (b) array architecture with 3116 ON-elements across the aperture.

following factors: (i) iterative computation of the AF pattern from the currently available excitation coefficients, (ii) adapting the computed AF to the required sidelobe mask leaving the far-field samples of the main lobe intact, and (iii) computing the updated excitation taper from the adapted (corrected) AF. A flow diagram of this approach is presented in Figure 5. Contrary to the IFT technique, the approach in Ref. [41] uses information regarding sidelobe peaks, including their angular locations and alternating signs.

The angular locations of the sidelobe peaks are determined and updated iteratively, and then used for computing the excitation taper by solving a suitable system of linear algebraic equations. Such linear system can be solved by means of matrix inversion as described in Ref. [41]. This procedure has been applied to the synthesis of sum patterns of equally spaced centrosymmetric linear arrays comprising up to 38 elements; only a few iterations were needed to achieve the targeted SLLs. As shown in Ref. [41], the number of pattern maxima should match the number of elements in the array. In general, such matching requires numerical experiments to adjust the spacing and/or the number of elements. The same approach has been demonstrated for the synthesis of equally rippled sidelobe patterns relevant to nonuniformly spaced scanning linear arrays; a representative example with 15 elements spanning seven wavelengths is reported in Ref. [42].

The approach in Refs. [41, 42], wherein the iterative procedure is performed through the inversion of a square system matrix, can serve as an effective solution for the synthesis problem, as highlighted in Ref. [43]. In the latter, however, pattern syntheses with complex-valued far-field samples and with far-field samples specified only in magnitude were considered as least square sense solutions for over-determined systems, i.e., when the number of far-field samples is larger than the number of array elements. In

Table 1: The IFT synthesis method: applications and selected features.

Array aperture	Pattern	Elements/ size	Synthesis	Variables	Work
Linear	Sum	8	1 desired direction + 6 discrete deep nulls	NA	[22]
Linear	Shaped Tx Shaped Rx	48	Main lobe shape, sector SLLs ≤ −33 dB, −50 dB	Phases in Tx, phases and amplitudes in Rx, 5-bit control for both	[23]
Circularly shaped with triangular lattice	Sum	5797	≤−71 dB SLL, Chebyshev sidelobes	Unconstrained amplitudes	[25]
Circularly shaped with triangular lattice	Sum	5797	Five level SLLs, −40 dB to −80 dB	Unconstrained amplitudes	[25]
Circularly shaped with square lattice	Sum	3413	Three level SLLs with four rectangular nulling sectors	Unconstrained amplitudes	[25]
Elliptically shaped with triangular lattice	Azimuth difference	5509	≤−71 dB SLL, mostly Chebyshev sidelobes	Unconstrained amplitudes	[25]
Circularly shaped with triangular lattice	Sum, Azimuth difference	5800	−51 dB SLL sum pattern, −48 dB SLL difference pattern, pattern recovery with 5, 10, and 30% failed elements	Constrained amplitudes, 8-bit quantization	[27]
Linear, thinned symmetrically and asymmetrically	Sum	200	SLL minimization with different fill factors (FL), e.g., −24.8 dB SLL achieved with 10,000 trials for 77% FL	On/off element states	[28]
Thinned circularly shaped 0.5-λ-spaced	Sum	7788, 9386	SLL minimization with 30% and 40% FL	On/off element states	[29]
Thinned circularly shaped 0.5-λ-spaced	Sum	25, 50, 100, and 133.3 λ	SLL minimization over the entire (u, v)-cell	10 dB range continuous amplitudes for ON elements, 15 dB amplitudes with nulling	[30]
Thinned circularly shaped 0.5-λ-spaced	Azimuth difference	25, 50, 100, and 133.3 λ	SLL minimization over the entire (u, v)-cell	20B range continuous amplitudes for ON elements	[30]
Linear	Sum	31, 61, 100, 200	SLL minimization with phase randomization	Phases with 3-to-8 bit resolutions	[33]
Linear	Sum, difference	40, 120	SLL minimization with amplitude randomization	20 dB amplitude range with, 4,5,6-bit resolutions	[33]

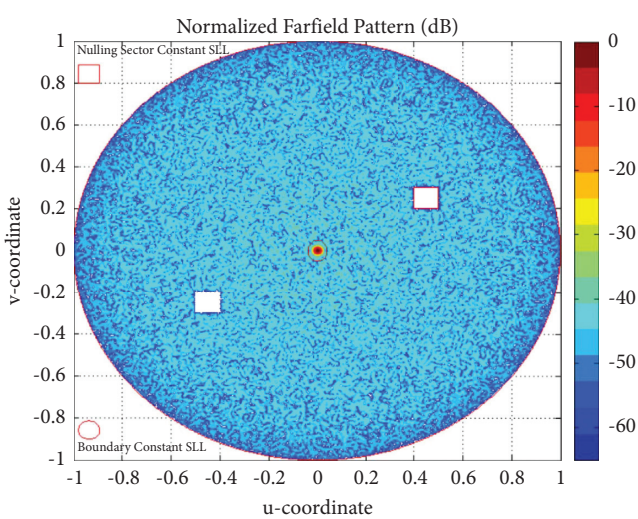

Figure 4: Sum pattern [30] of a thinned 100λ circular array with 0.5λ spaced square lattice and 30% FL as synthesized through the IFT technique with an amplitude-only taper. The pattern features a SLL of −40 dB and two 65 dB depth nulling sectors.

numerical examples of both synthesis cases in Ref. [43], the far-field samples were defined only over the angular quadrant that covered the main lobe.

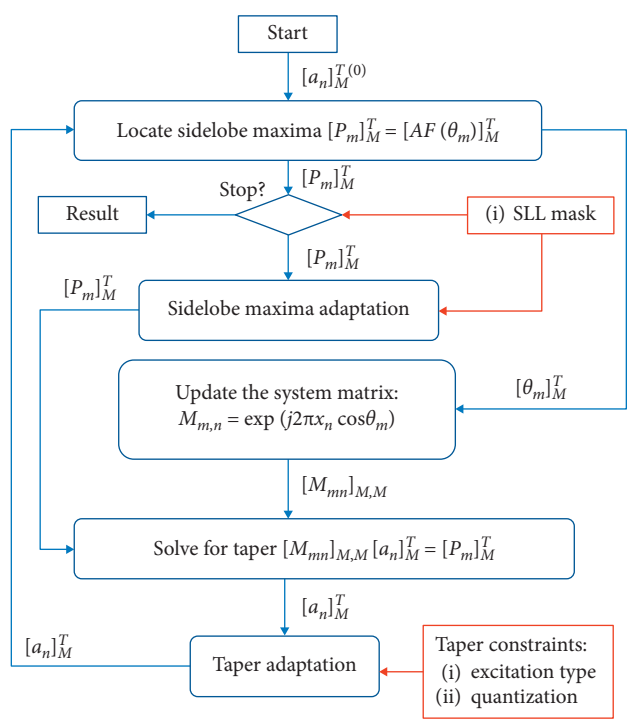

Figure 5: Block diagram of the linear array pattern synthesis technique detailed in Refs. [41, 42].

It is worth noting that the described iterative methods are based on the AF and are not suitable for antenna array syntheses that are associated with additional radiation pattern requirements, such as those relevant to maximal directivity and polarization characteristics. Furthermore, these methods do not account for the nonidentical far-fields of array-embedded elements.

2.3. Array Pattern Synthesis Using Gradient-Based Optimization. The use of population-based algorithms such as genetic algorithms (GAs) and particle swarm optimizers (PSOs) for antenna array synthesis is usually justified by the presence of multiple local optima of the objective function (which, in turn, is related to the AF) over the design space. In such scenarios, gradient-based algorithms are typically considered to be useful for optimization in the vicinity of nominal design. At the same time, numerical examples have demonstrated that array pattern synthesis, when formulated as an optimization problem, does not benefit from the use of population-based algorithms in handling AF-based objective functions. As opposed to contemporary practices, it has been found that array pattern synthesis through gradient-based optimization, combined with a smart random search, provides similar results as compared to population-based techniques, while offering a definitive advantage from a computational standpoint [44–46].

To improve the computational effectiveness of gradient-based optimization and avoid trapping in local minima, it is advisable to (i) utilize analytical derivatives of the objective function, wherever available and (ii) to introduce a reasonable degree of randomness in the solution process.

Analytical expressions can be easily derived for the AF pattern and directivity functions, by using equation (2.30) in [44] for linear array directivity. The smart random search [45] linearly combines a randomly generated point x_{rand} with the current best design x_{best} such that the search procedure is biased towards the global best design as the iteration count i gets closer to the maximum number of iterations $i_{\max}$ allowed for the random search stage [44]:

$$\mathbf{x}^{(i+1)} = \lambda^{(i)}\mathbf{x}_{\text{rand}} + \left(1 - \lambda^{(i)}\right)\mathbf{x}_{\text{best}}, \tag{3}$$

where the scalar $\lambda^{(i)}$ is forced to decay with the iterations, for example, $\lambda^{(i)} = 1 - i/i_{\max}$. Formula (3) was established empirically. Its numerical efficiency for array syntheses has been validated through the heuristic approach described below.

Numerical studies have been conducted on different end-fire linear arrays with $N = 10$, 20, and 40 radiating elements using the corresponding Hansen–Woodyard (H-W) designs as the initial solution proxies [47]. The standard sequential quadratic programming (SQP) algorithm, implemented in the MATLAB *fminimax* routine, was the main optimization engine [48]. For each case, the array synthesis was completed after only a few hundred objective function evaluations, instead of thousand iterations, which is typically required by population-based methods such as GAs or PSOs. The design cases presented in Refs. [44, 45] were aimed at achieving the following goals:

SLL reduction and AF directivity maximization with uniform interelement separation and progressive phase shift as variables

SLL reduction with variable element-specific progressive phase shifts (i.e., with N-1 variables)

SLL reduction with nonuniform element spacing and element-specific progressive phase shifts (i.e., with 2N-2 variables)

SLL reduction with an additional 20 dB suppression over the first sidelobe sector of the H-W design combined with constrained nonuniform element separation and element-specific progressive phase shifts

It is worth noting that the random search stage was necessary for cases with 20 and 40 element arrays wherein element separations and phase shifts were used as variables. In other cases, a direct gradient optimization was sufficient.

The efficiency of the discussed approach has also been illustrated with two synthesis examples of a boresight linear array, one featuring a sum pattern with additional deep nulling sectors, and another featuring a low-sidelobe symmetrical sector-beam pattern in Refs. [44, 46]. In these examples, the array patterns were synthesized using the same number of array elements, the same number of design variables, and the same pattern masks as in the synthesis examples tackled in ref. [49] using Taguchi's method. It should be noted that in the case of the low-sidelobe sum pattern with additional nulling sectors, the gradient-based search technique combined with analytical derivatives [44, 46] yielded the final result after only 300 cost function evaluations without the need of resorting to a random search. Furthermore, the array pattern synthesized using the gradient-based search, shown in Figure 6(a), significantly outperforms the pattern obtained through Taguchi's method (Figure 3 in [49]) in terms of both peak SLL (PSLL) and nulling sector depth.

For symmetrical sector-beam pattern synthesis, the gradient-based search combined with the analytical derivatives of the cost function yielded an optimal solution with a −28.7 dB PSLL after 1500 cost function calls, as shown in Figure 6(b), while the Taguchi's method produced a pattern featuring a −25 dB PSLL (see Figure 6 in [49]) after 4920 cost function calls. The first 1000 cost function calls (out of 1500) in the gradient-based synthesis of the sector-beam pattern in Refs. [44, 46] were invested on the smart random search stage. The same sector-beam pattern problem was synthesized using a particle swarm optimizer [50], where a solution with characteristics similar to the solution generated using Taguchi's method was obtained after 16000 cost function calls.

The gradient-based optimization was used along with analytical derivatives and smart random search (where necessary), also for array synthesis that included array radiators with different far-field and S-parameter characteristics. In such situations (usually when the number of array elements is smaller than 500), full-wave EM simulation tools should not only be used for verification of the final results but also for the main steps in the design process. At the same

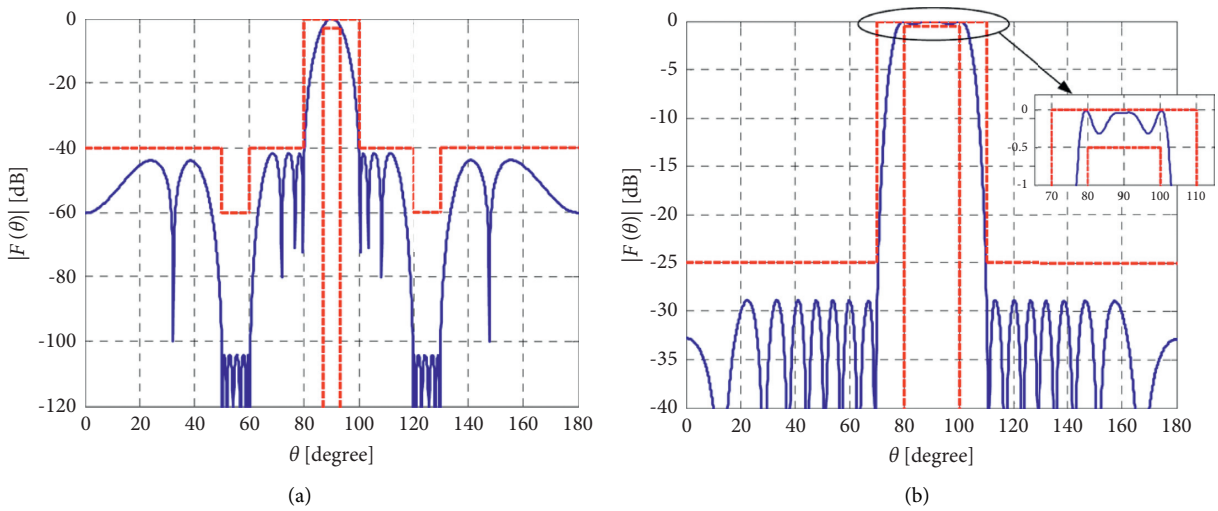

Figure 6: Examples of AF patterns synthesized using a gradient-based optimizer enhanced with analytical derivatives and smart random search [44, 46]: (a) sum pattern; (b) sector-beam pattern.

time, a gradient-based optimizer can efficiently be used to adjust AF-based models during the prototyping stage [44, 51, 52], e.g., as depicted in the flowchart of Figure 10.17 in Ref. [44] or Figure 4 in Ref. [51]. In addition, gradient-based search methods have been used in the simulation-based design of low-sidelobe arrays for the following tasks [53]:

To find the corporate feed architecture and constrained power-split ratios of the feed junctions (see Step 2 in Figure 7)

To optimize the EM-based response-surface model (smooth kriging surrogate) of array feed junctions, using the Matlab *fmincon* routine [48] (see Step 5 in Figure 7)

To fix the SLL degradation due to coupling and interactions within the feed connected to the array aperture (see Step 9 in Figure 7)

It is worth noting that the gradient-based routines can not only successfully optimize smooth surrogate models, as depicted in Figure 7, but also optimize the original high-fidelity models (configured from accurately simulated far-fields [54]), e.g., the models of planar apertures depicted in Figure 8, which require higher computational costs, mostly due to the acquisition of accurate far-field characteristics.

3. Deterministic Array Pattern Syntheses with Nonperiodically Distributed Antenna Elements

3.1. Synthesis Based on the Auxiliary Array Pattern (AAP). The design of sparse antenna arrays is receiving huge attention mainly thanks to meaningful advantages such as a reduced number of antenna elements, reduced weight, and complexity of feeding networks, as well as a larger average interelement separation which alleviates thermal and parasitic EM-coupling effects. In addition, properly synthesized arrays with aperiodic element separations produce no main lobe replicas in the visible space, even while scanning. Nonperiodic architectures can also mitigate cost-related issues for conformal antenna arrays, which offer compelling advantages in terms of electronic beam scanning, visual unobtrusiveness, and noninterference with the aerodynamic characteristics of the host body (e.g., aircraft, satellites, and different categories of terrestrial vehicles). The design of conformal arrays, however, poses additional challenges compared with planar topologies. It should be noted that the adoption of population-based techniques for the synthesis of sparse arrays with nonperiodically distributed radiators in problems with a significant number of unknowns usually results in very large synthesis times. In this context, deterministic methods are preferable.

A method based on the concept of the auxiliary array pattern (AAP) function was developed to analytically determine the optimal element density and excitation tapering distributions to mimic a given radiation pattern [55–57]. Thus, the array sparseness can be conveniently tuned to meet the design requirements in terms of minimum separation between different antenna elements and maximal array aperture size. This approach does not require optimization or iterative procedures to perform the synthesis, thus reducing the design time.

The AAP approach has been elaborated further to handle conformal array apertures [58, 59] subject to different pattern masks and structure constraints, similar to those illustrated in Figures 9–12. It has been proven that this procedure allows for complex synthesis problems, subject to specific requirements associated with pattern magnitude and phase masks, maximum aperture size, minimum interelement spacing, or maximum number of power levels to be operated in the beam-forming network. These requirements need to be addressed in a straightforward and computationally inexpensive manner [59].

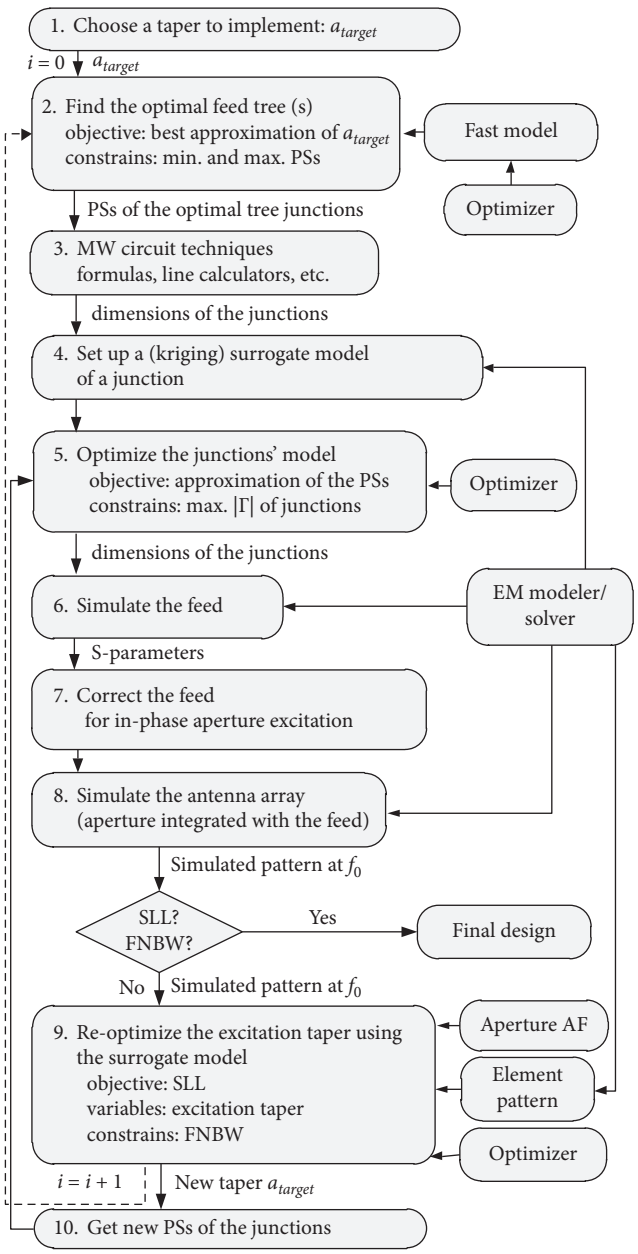

Figure 7: Process diagram of a surrogate-assisted design of low-sidelobe linear arrays inclusive of corporate feeding network [53]. PS stands for the feed junction split ratio, $|\Gamma|$ denotes the general reflection coefficient at the junction input, **a** stands for the excitation taper, and f_0 is the working frequency. The AF is used at Steps 2 and 9. A more general realization of the design process can search for and implement a new optimal architecture after Step 9.

3.2. Synthesis Using the Array Dilation Technique (ADT). The Array Dilation Technique (ADT) is another deterministic approach which has been recently proposed in ref. [60]. At a conceptual level of description, the ADT stretches a linear array in analogy to an elastic strip, thus leading to aperiodicity and sparsity in the linear array lattice. As presented, the ADT handles isophoric symmetric linear arrays, namely, centrosymmetric arrays with uniform excitation. Thus, it does not rely on any excitation tapering; instead, it modifies the interelement spacings in a uniformly fed array with an originally uniform lattice. The ADT achieves comparatively lower SLLs for optimal thinning levels [61] as compared to previously published approaches [60]. The ADT is a noniterative method that can be used to determine the nonuniform separations between array elements so as to yield the lowest possible SLL for a particular partitioning and impose constraints on the interelement spacing. The ADI dilates the linear array lattice according to Ref. [58]:

$$d_n = d_0 \left\{ 1 + \frac{\alpha_J}{N_t} \left(|n| - 1 \right) \right\}, \tag{4}$$

where d_0 is the initial element separation, N_t is the total number of elements in the modified lattice, the index n runs over half of the element separations, and α_J is the dilation parameter in a given partitioning, such that the element separation d_n in that particular lattice part varies from d_0 to $\alpha_J\, d_0$. In Ref. [60], α_J took values from {0, 1, 2, 3, 4}.

The value for the innermost element separation (one separation for the even number of elements and two separations for the odd number) was set to d_0 in the numerical studies. Array lattice geometries corresponding to different combinations of dilation parameter values were enumerated for a given number of array elements and the initial (innermost) separation d_0 (both representing the original lattice). Each lattice geometry was characterized by AF directivity, HPBW, SLL, PSLL, average SLL, first sidelobe intensity, and average element separation. In particular, AF directivity was assessed using analytical expressions [62]. Several case studies have demonstrated that ADT can be used for syntheses of isophoric linear array lattices with minimal possible SLLs. The array geometry with the lowest peak SLL is identified among the enumerated array geometries [60]. The range of the direction cosines (see equation (2)), over which the enumerated array SLLs were evaluated, was not specified in Ref. [60].

The various test cases included the following:

Low-SLL synthesis with 17, 37, and 2000 elements subject to no constraints on the array length and starting from a half-wavelength-spaced lattice

Low-SLL synthesis with 17, 37, and 2000 elements and fixed array lengths starting from a half-wavelength-spaced lattice

Synthesis for grating lobe suppression with 37 elements starting from a wavelength-spaced lattice

A comparison of the ADT-synthesized linear arrays with respect to PSLL and other performance characteristics (where available) was given, and results were obtained using several other methods [60], where the ADT-synthesized arrays demonstrated similar or even better characteristics. Selected ADT-synthesized lattices were implemented and simulated as array apertures comprising cavity-backed microstrip patch antennas; their scan performance has also been demonstrated experimentally. A noticeable feature of ADT-synthesized linear arrays is that, although their

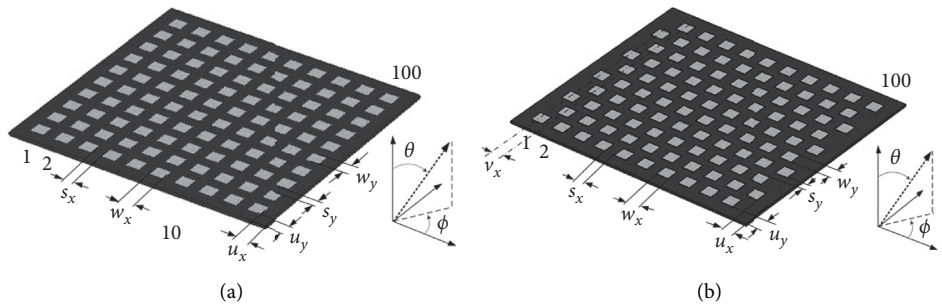

Figure 8: Planar array apertures comprising 100 linearly polarized microstrip patch antennas: (a) Cartesian grid; (b) triangular grid. Phase-only syntheses for reduced SLLs were performed using EM-simulated models in Ref. [54].

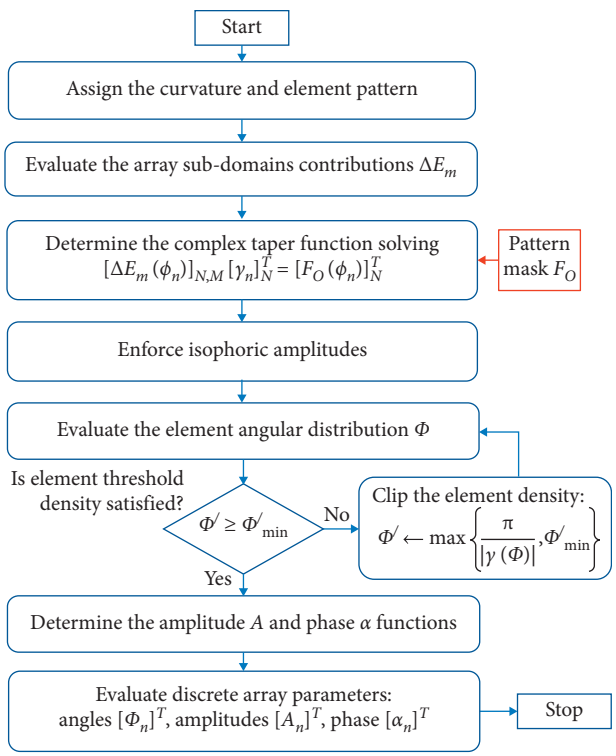

Figure 9: Diagram of the AAP technique for conformal array synthesis with constraints on the structure layout [58].

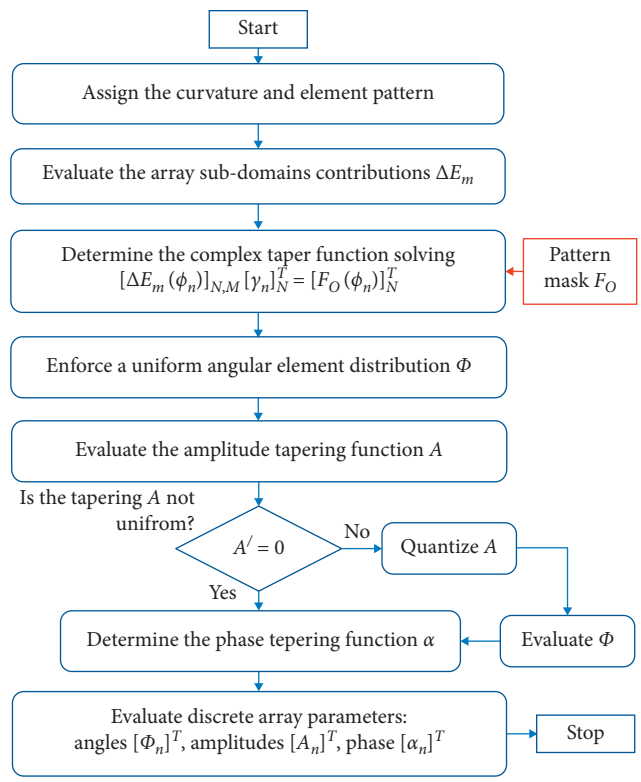

Figure 10: Diagram of the AAP technique for array synthesis with a quantization of the excitation amplitude [58].

scanned AF patterns show a definite degradation of the PSLL, wide angular sectors with low SLL persist next to the main lobe, as illustrated in Figure 13.

4. Phased Array Pattern Synthesis with Nonidentical Array Element Far Fields

It can be inferred from recent scientific publications on the development of phased antenna arrays for 5G applications [63–76] that array pattern synthesis requires the selection or evaluation of the following parameters and characteristics for the initialization of the synthesis procedure: the number of array elements, the aperture size, the separation between array elements (cell size), the array aperture lattice, as well as the detailed design of the individual array element including the relevant stack-up, polarization (single or dual per element), and spatial orientation along the radiating aperture. Such settings are aimed at system-level specifications and account for the adopted (or designed) beamforming integrated circuit (BFIC) solution and the host printed circuit board (PCB) manufacturing technology (including dimensional restrictions defined by the PCB design rules). In the context of array pattern synthesis, the adopted BFIC delivers a certain gain range, amplitude, and phase-control resolutions and errors in Tx and Rx mode. The design of Wilkinson's divider/combiner networks typically stays out of the scope of radiation pattern synthesis in the case of active phased arrays with fully RF beamforming chips.

In a phased-array development process, pattern synthesis serves as an effective means to fill a reliable and operation-mode-specific scan table to meet the required design specifications concerning several factors, such as effective isotropic

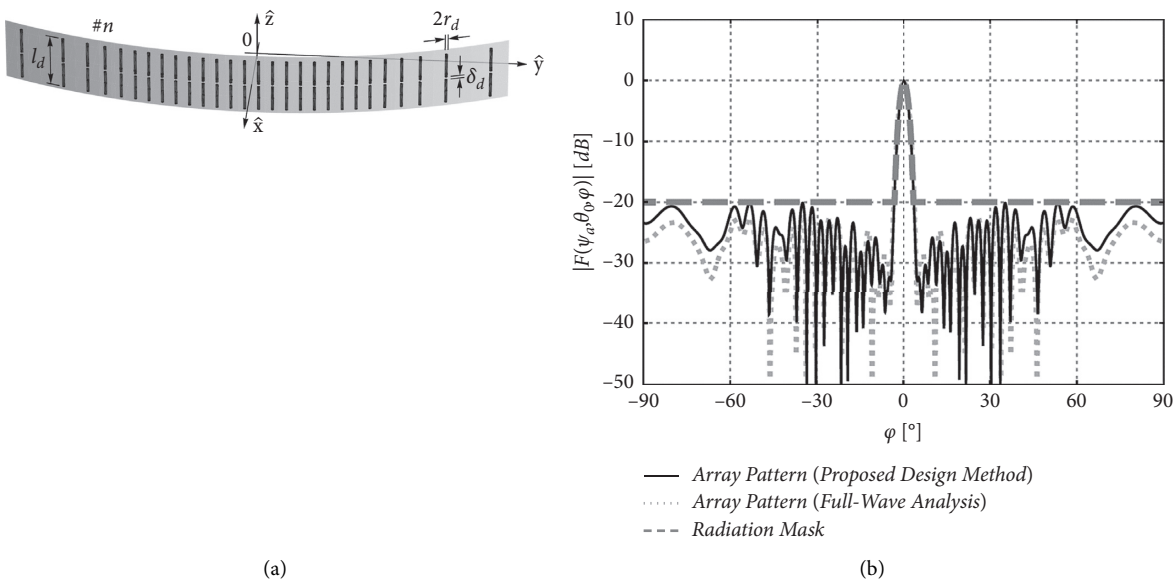

Figure 11: Synthesized sparse 24λ-long arc array aperture with curvature radius of 30λ and 28 antenna elements that features an HPBW of 6 degrees and SLL of −20 dB [59]: (a) physical implementation where each array element is a 0.425λ long dipole antenna with 0.0125λ radius and 0.005λ feeding delta gap; (b) magnitude of the array radiation pattern.

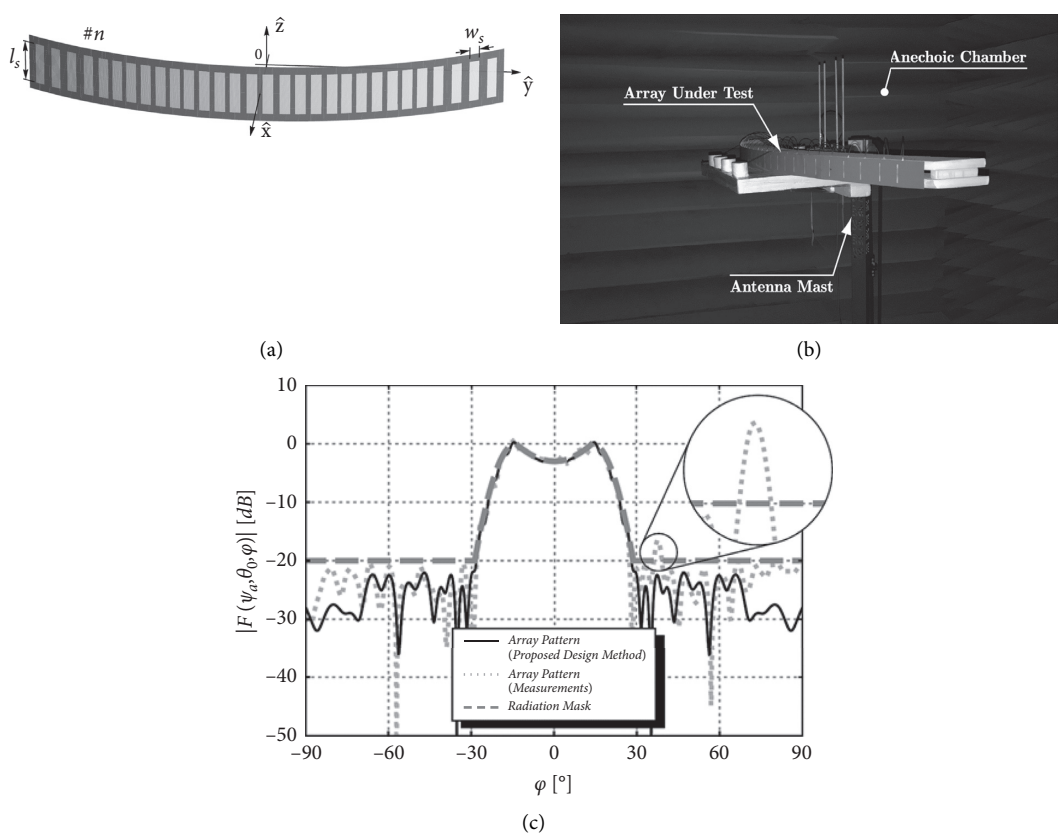

Figure 12: Synthesized sparse 23λ-long arc array aperture with curvature radius of 21λ and 30 antenna elements that features an isoflux radiation pattern [59]: (a) physical implementation based on 0.607$\lambda \times$ 0.0367λ slot antennas; (b) 5 GHz prototype under test; (c) synthesized and measured array radiation patterns.

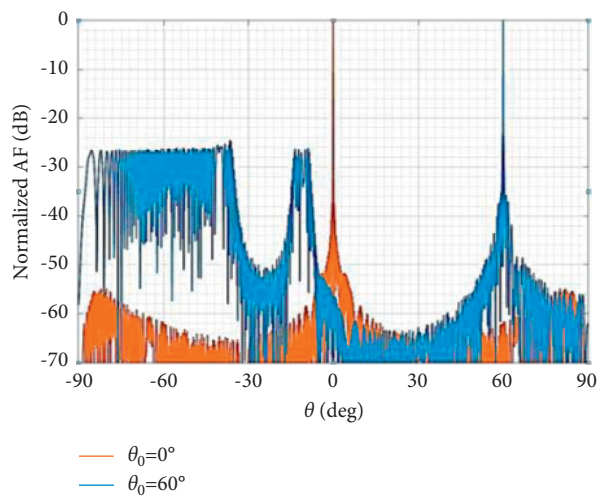

Figure 13: Normalized AF patterns featured by an isophoric 2000-element sparse linear array with antenna separation $d_0 = 0.5\lambda$ at the scan angles of 0 and 60 degrees [60]. The array was synthesized with no constraint on the overall length, which, eventually, was extended up to 1344.2λ.

radiated power (EIRP), polarization purity, cross-polarization interference and discrimination, scan range, scan loss, and active reflection coefficients. Note that, wherein the array aperture dimensions are fixed, the excitation tapers appear to be the only essential degrees of freedom in the synthesis procedure. While 5G base stations operating at sub-cm and mm-wave frequencies are likely to require 64 to 256 (or more) radiating elements per array aperture so as to achieve the desired peak EIRP level, 5G customer premise equipment (CPE) operating at sub-cm and mm-wave frequencies is expected to rely on phased arrays with approximately 8 to 32 radiating elements. Thus, the differences in terms of embedded element far-field characteristics can be significant and should be properly accounted for.

In such circumstances, a reusable accurate EM model for phased array synthesis, illustrated in Figures 14 and 15, can be implemented on the basis of the superposition principle, through a complex-valued vectorial summation over all the array aperture inputs:

$$\mathbf{E}(\mathbf{r}) = \sum_n a_n \mathbf{E}_n(\mathbf{r}), \tag{5}$$

where the summation index n runs over the antenna elements in the case of single-polarization radiators and over the antenna input ports in the case of radiators supporting dual, supposedly orthogonal, polarizations.

In (5), $\mathbf{E}$ stands for the total electric field; $\mathbf{E}_n$ stands for the EM-simulated (or measured) electric fields due to the separate excitation of the input port n at the relevant BFIC TX-output/RX-input pin, and a_n is the complex wave exciting the n-th port, namely, the n-th entry of the excitation taper, at the frequency of operation f_0. Note that the field terms $\mathbf{E}_n$ in (4) are evaluated in the same coordinate reference system (a default option of the state-of-the-art EM simulation environments) such that the phase correction associated with the radiator location is directly embedded in $\mathbf{E}_n$. It should also be noted that the radial vector r is defined, for all the $\mathbf{E}_n$, starting from the origin of the adopted coordinate system.

Therefore, the summation in (5) allows quantifying the field-related characteristics at the working frequency f_0 at any point $\mathbf{r}$ in space, including the near-field region. In the far-field region, it is convenient to cast (5) in the following form:

$$\mathbf{E}(\theta, \phi) = \sum_n a_n \mathbf{E}_n(\theta, \phi), \tag{6}$$

where the distance r is regarded as a parameter. In practice, r is set equal to a certain value (i.e., $r = 1$ m) during the post-processing of the EM-simulated data for the evaluation of the general far-field quantity $\mathbf{E}_n$.

Moreover, state-of-the-art simulation environments also allow for the embedded far-field distributions to be computed by referring to an element-specific (local) coordinate system, such that the phase terms associated with the element locations across the aperture can be evaluated as

$$\mathbf{E}(\theta, \phi) = \sum_n a_n \mathbf{E}_n(\theta, \phi) e^{\mathbf{jk}\cdot\mathbf{R}_n}, \tag{7}$$

where the wave propagation vector $\mathbf{k} = k\ [u, v]^T$ incorporates the direction cosines, $\mathbf{R}_n$ denotes the location of the n-th element along the array aperture, and the complex far-field term $\mathbf{E}'_n$ is computed referring to the location of the n-th element parametrized through the shift vector $\mathbf{R}_n$.

Equation (7) can be simplified into AF with the assumption of identical far fields E_n, by moving the far fields out of the sum. On the other hand, an accurate modeling of the electromagnetic field characteristics of phased arrays is only possible using (5)–(7). Such EM-based modeling is necessary to reliably quantify cross-polarization interference/discrimination, especially for apertures that simultaneously generate beams with orthogonal polarization

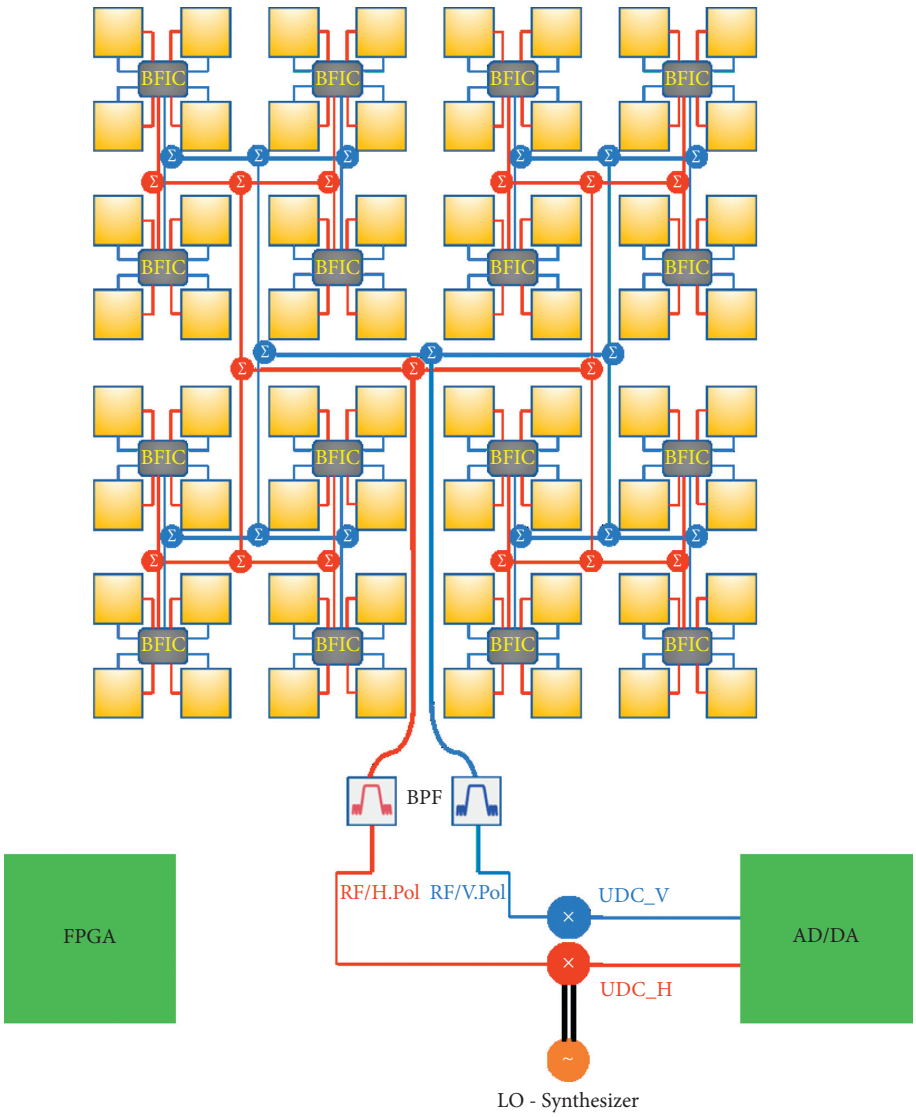

Figure 14: Diagram of a 5G phased array antenna capable of dual-beam operation and comprising 64 dual-polarized radiating elements, this resulting in 2×64 array inputs. Every beamforming integrated circuit (BFIC) is connected to 8 antenna inputs/outputs (with each dual-polarized antenna having two inputs/outputs) and has two common inputs/outputs (one per polarization as indicated with the blue and red color lines) connected to polarization-specific Wilkinson's networks.

characteristics. Note that the element-specific amplitude and phase behavior of $\mathbf{E}'_n(\theta, \phi)$ is preserved in (5)–(7) to the full extent, whereas some information is lost in the AF-based modeling. For planar array apertures, (7) can be rewritten as

$$\mathbf{E}(u, v) = \sum_n a_n \mathbf{E}_n(u, v) e^{jk(x_n u + y_n v)}. \tag{8}$$

Although the element far-field terms $\mathbf{E}_n$ are not known over the entire (u, v)-space, their analytical continuation into the invisible space allows using (8) to evaluate the total far-field distribution over the entire space, thereby enabling the analysis of the array scanning performance.

Another important aspect in phased-array pattern synthesis is that the total far-field representation based on (5)–(8) is an accurate reusable model with well-defined analytical derivatives with respect to the excitation taper entries (that constitute the available degrees of freedom for the synthesis problem). The cost associated with the acquisition of such EM model equals the product of the total number of input ports and the simulation time of the array with aperture [51, 52, 54]. Thus, minimax routines enhanced with analytical derivatives similar to those in Ref. [48], and combined with the smart random search, are well suited for phased array synthesis for SLL minimization, pattern nulling, cross-polarization minimization, and polarization interference minimization. Syntheses of planar and linear apertures based on this methodology have been conducted and described in Refs. [54, 77], respectively. A few selective results are shown in Figures 16 and 17. A surrogate-based modeling was used in Refs. [51, 52, 54, 77] so as to reduce the

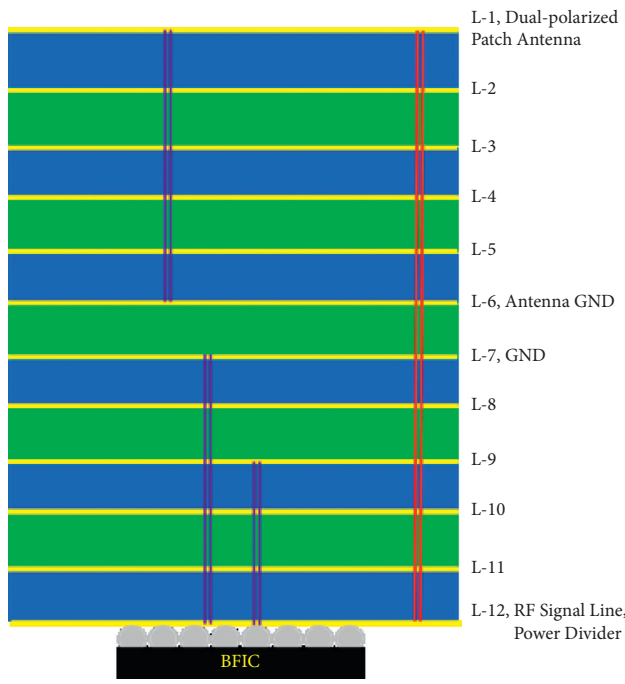

Figure 15: Simplified diagram of a low-cost PCB stack-up for 5G phased antenna arrays.

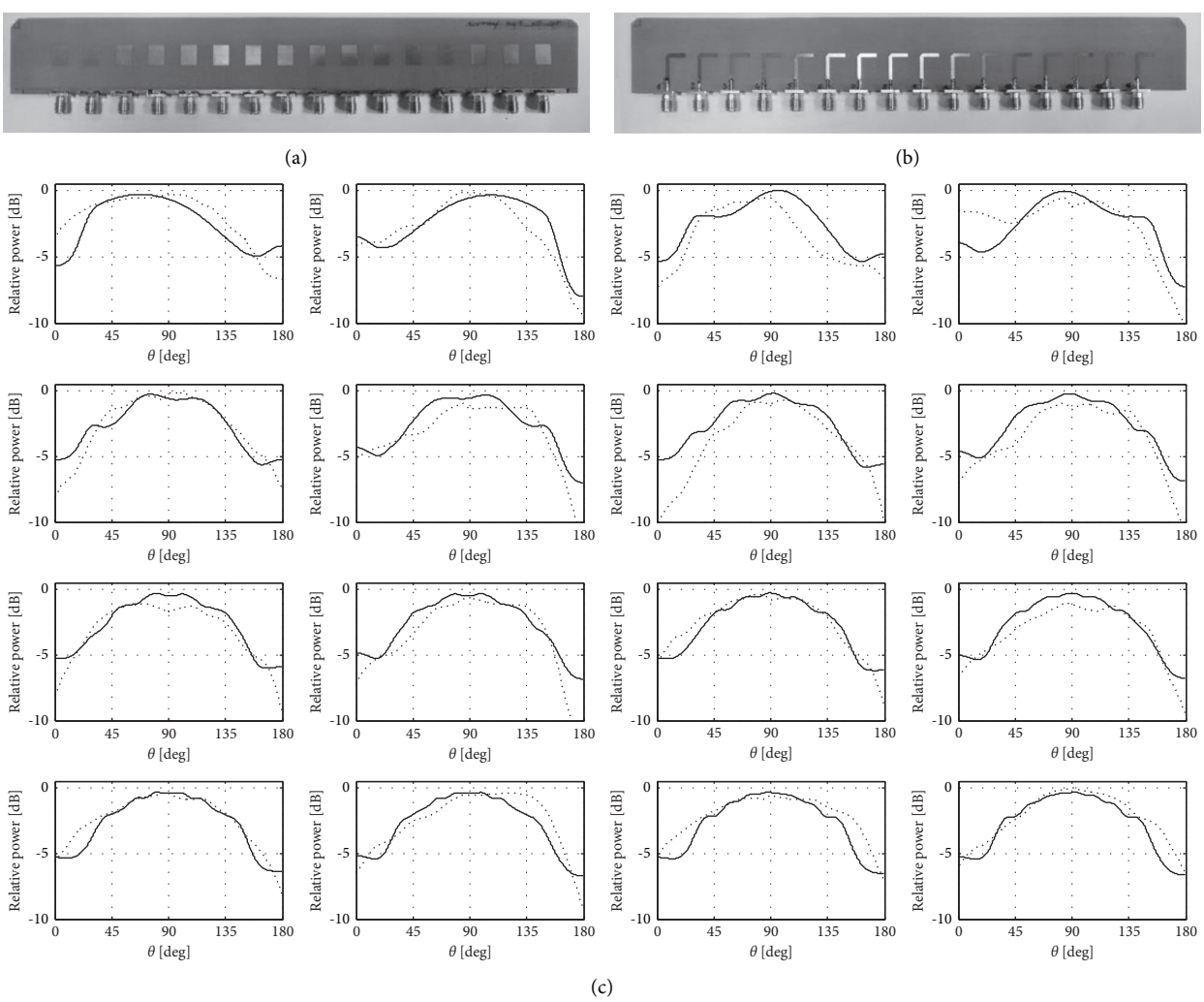

Figure 16: Antenna array operating at 10 GHz [77]: (a) front view; (b) back view; (c) measured (. . .) and simulated (▬) aperture-embedded-element E-plane patterns. The measured and simulated radiation patterns are normalized, respectively, to the maximal measured and simulated values. The patterns are displayed from top to bottom as follows: 1 and 16 (outermost elements), 2 and 15,. . ., 7 and 8 (central elements).

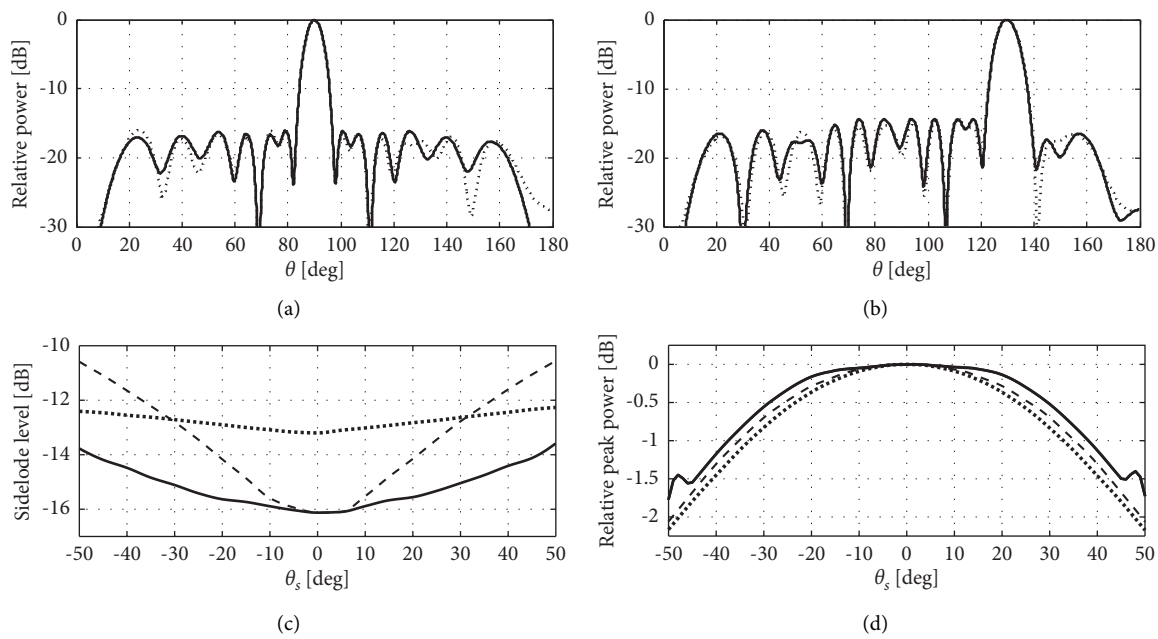

Figure 17: Selected radiation patterns at 10 GHz of the array shown in Figure 16 as obtained by phase-only synthesis [77]: (a) E-plane boresight array pattern, as simulated (-) and measured (); (b) E-plane array pattern scanned to 40 degrees, as simulated (-) and measured (); (c) SLL versus scan angle based on the synthesized scan-specific phase tapers (—), with the phase taper optimized for boresight radiation (— —), with uniform taper (▪▪▪); (d) realized gain scan loss with the synthesized scan-specific phase tapers (—), with the phase taper optimized for boresight radiation (— —), with uniform taper (▪▪▪).

Table 2: Alternative methods for phased antenna array synthesis: a qualitative comparison.

Method	Handleable array sizes (elements)	Modeling fidelity	Comp. speed, realizability	Automation suitability as demonstrated*
IFT/IFFT	Very large (thousands)	AF	Very fast (FFT-based), yes	High
Matrix inversion	Medium (dozens)	AF	Moderate, yes	Low-to-medium
Gradient-based with smart search	Up to large (hundreds)	AF, Vectorial EM***	Moderate-to-fast**, yes	Medium-to-high
Deterministic AAP-based	Up to very large (thousands)	AF	Fast	Medium-to-high
Deterministic ADT-based	Up to very large (thousands)	AF	Fast yet with enumeration	Medium

*Suitability for automation within the phased array development process. ** Fast with analytical derivatives, and very fast for EM-level of description if enhanced by surrogate-based optimization. *** As well as circuit scattering signals (e.g., active reflection coefficients).

Table 3: The matrix inversion synthesis method: applications and features.

Array aperture	Pattern	Elements/size	Synthesis	Variables	Work
Linear	Symmetric sum, unsymmetric sum, two beams, monotonically decaying sidelobes	10, 18, 28, 38, 15	Chebyshev SLLs, −20 and −40 dB two side SLLs and alternating SLLs with uniform and nonuniform separation	Unconstrained amplitudes and phases	[41, 42]

Table 4: Gradient-based optimization synthesis: selected applications and features.

Array aperture	Pattern	Elements/size	Synthesis	Variables	Work
Linear	End-fire	10, 20, 40	AF-based SLL minimization AF-based SLL minimization with directivity maximization AF-based SLL minimization with nulling	Constrained element separations, amplitudes, and phases	[44, 45]

Table 4: Continued.

Array aperture	Pattern	Elements/size	Synthesis	Variables	Work
Linear	Sum, Sector beam		AF-based SLL minimization with nulling AF-based sector beam shaping with SLL minimization	Amplitudes and spacing; amplitudes, phases, and spacing	[44, 45]
Linear	Sum	32 symmetric	AF-based SLL minimization EM-based SLL minimization combined with active reflection control	Constrained nonuniform element separations, phases; constrained element spacing, phases	[51, 52]
Linear aperture with integrated corporate feed	Sum	12 symmetric	Corporate feed constrained synthesis for Chebyshev sidelobes EM-based SLL minimization*	Constrained power splits of the corporate feed junctions	[53]
Linear	Sum	16	Scan table using EM-based SLL minimization* at scanning	Phase tapers	[77]
Planar with square and skewed lattices	Sum	16 100	EM-based SLL minimization* combined with control of peak realized gain and active reflection coefficients EM-based SLL minimization* combined with control of active reflections	Constrained amplitudes and phases	[54]

*Within surrogate-based techniques for computational speed-up of pattern syntheses.

Table 5: AAP-based deterministic synthesis method: applications and features.

Array aperture	Pattern	Elements/ size	Synthesis	Variables	Work
Linear sparse flat	Sum	24	Equally rippled reduced SLL	Constrained element separations	[56]
Sparse planar	Sum	1122	Reduced SLL	Constrained element separations and amplitudes (3-level control)	[56]
Linear sparse conformal	Symmetric sum Sector beam	28 30	Magnitude and phase pattern Isolux illumination	Constrained separations, amplitudes (4-level-control), and phases	[59]

Table 6: ADT-based deterministic synthesis method: applications and features.

Array aperture	Pattern	Elements/ size	Synthesis	Variables	Work
Linear sparse	Sum	17, 37, 2000	Minimal SLL with unconstrained and constrained array length	Dilated element separations, unconstrained and constrained	[60]

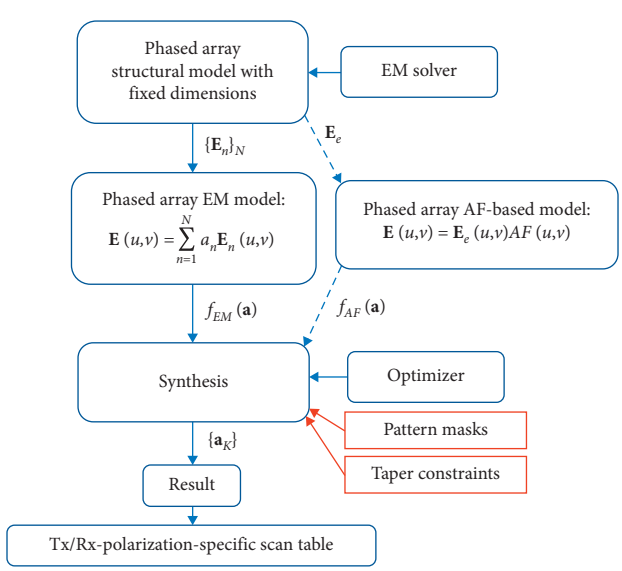

Figure 18: Simplified diagram of a phased antenna array pattern synthesis with nonidentical far-field responses of the embedded radiating elements.

computational cost of the synthesis procedure in the part relevant to the acquisition of the element-specific far-field distributions $\mathbf{E}_n$.

The polarization-specific EIRP patterns and peak values, with any complex taper applied to the radiating aperture, are readily available for evaluation and/or synthesis purposes at the EM level of description through any form of (4)–(7) with

$$\mathrm{EIRP}(\theta,\phi)_l[\mathrm{d}Bm] = p_{e,\max}[\mathrm{d}Bm] + 20\log_{10}\left|\mathbf{l}\cdot\mathbf{E}(\theta,\phi)_t\left[\frac{V}{m}\right]\right| - 14.77, \quad (9)$$

where $p_{e,\max}$ stands for the available power maximum at the BFIC TX outputs (depicted with the BFIC solder balls in Figure 15). The subscript t which denotes the total electric field indicates the evaluation with a complex taper normalized to its maximal amplitude, and the subscript l and unit vector $\mathbf{l}$ both refer to a particular polarization of the total far-field.

The insertion losses associated with transmission lines and transitions integrated in the array beamforming network are included in (9) if the ports in the EM-simulated model are defined at the BFIC TX outputs. In the case of uniform excitation, following a number of assumptions (including $\mathbf{E}_e = \mathbf{E}_n$ for all the radiators) and evaluating the element realized gain as

$$G_{e,\max}[\mathrm{d}B] + p_e[\mathrm{d}BW] = 20\log_{10}\left|\mathbf{E}_e(r=1m)\right|_{\max} - 14.77. \quad (10)$$

Expression in (9) reduces to a well-known yet simplistic formula that is indispensable for quick system-level calculations (see (1) in [65] or (2) in [17] or [78]).

5. Conclusions

Based on a detailed analysis and comparison of methods, summarized in Table 2, and by considering the application scope and features of the considered approaches listed in Tables 1 and 3–6, it can be concluded that the IFT method suits the development of large linear and planar phased array apertures, with a sufficient AF description. The matrix inversion method is suitable for fast array prototyping because it relies on user decisions (or needs intelligent routines) to address the synthesis problem while tracking the locations of the sidelobe peaks at each iteration. The deterministic methods are inexpensive and versatile, and they are capable of synthesizing aperiodic (using AAP and ADT methods) and conformal (using AAP method) array grids. The AAP method accounts for the angular dependence of the element pattern; however, it does not account for nonidentical far-fields of the array elements. In the development of active phased arrays for 5G applications where EM-simulation-based description is necessary, the far-field synthesis through gradient-based optimization combined with a smart random search can be used. The need for EM simulation is dictated by the nonidentical far-fields of the embedded array elements, different polarization characteristics, or both (as a part of the process relevant to the pattern synthesis depicted in Figure 18). Furthermore, this method has a higher efficiency as compared to population-based optimizers. In addition, the surrogate-based methodology can significantly reduce the overall cost of EM-based syntheses during the acquisition of the vectorial far-field EM-based models of 5G active phased arrays.

Conflicts of Interest

The authors declare that they have no conflicts of interest.

References

[1] T. S. Rappaport, S. Sun, R. Mayzus et al., "Millimeter wave mobile communications for 5G cellular: it will work!" *IEEE Access*, vol. 1, pp. 335–349, 2013.

[2] E. Dahlman, S. Parkvall, J. Skold, and N. R. 5G, *The Next Generation Wireless Access Technology*, Academic Press, London, UK, 2018.

[3] W. Hong, Z. H. Jiang, C. Yu et al., "Multibeam antenna technologies for 5G wireless communications," *IEEE Transactions on Antennas and Propagation*, vol. 65, no. 12, pp. 6231–6249, 2017.

[4] S. Kutty and D. Sen, "Beamforming for millimeter wave communications: an inclusive survey," *IEEE Communications Surveys & Tutorials*, vol. 18, no. 2, pp. 949–973, 2016.

[5] A. B. Smolders, A. Dubok, N. M. Tessema et al., "Building 5G millimeter-wave wireless infrastructure: wide-scan focal-plane arrays with broadband optical beamforming," *IEEE Antennas and Propagation Magazine*, vol. 61, no. 2, pp. 53–62, 2019.

[6] R. L. Haupt and Y. Rahmat-Samii, "Antenna array developments: a perspective on the past, present and future," *IEEE Antennas and Propagation Magazine*, vol. 57, no. 1, pp. 86–96, 2015.

[7] T. C. Cheston and J. Frank, "Phased array radar antennas," in *Chapter 7 in Radar Handbook*, M. I. Skolnik, Ed., McGraw-Hill, Boston, MA, USA, 2nd edition, 1990.

[8] R. C. Hansen, *Phase Array Antennas*, Wiley, Hoboken, NJ, USA, 2nd edition, 2009.

[9] Dassault Systèmes, *CST Studio Suite 2020*, Dassault Systèmes, Meudon, France, 2020.

[10] Ansys Inc, *Ansys HFSS 2020 R1*, Ansys Inc, Canonsburg, PA, USA, 2020.

[11] COMSOL, Inc., *Multiphysics Ver. 5.4, 2020*, COMSOL, Inc., Burlington, MA, USA, 2020.

[12] Sonnet Software, Inc., *Sonnet Release 16*, Sonnet Software, Inc., Syracuce, NY, USA, 2018.

[13] S. Ghosh and D. Sen, "An inclusive survey on array antenna design for millimeter-wave communications," *IEEE Access*, vol. 7, pp. 83137–83161, 2019.

[14] D. Caratelli, A. Al-Rawi, J. Song, and D. Favreau, "Dielectric resonator antenna arrays for 5G wireless communications," *Microwave Journal*, pp. 36–46, 2020.

[15] S. Alkaraki and Y. Gao, "Mm-wave low-cost 3D printed MIMO antennas with beam switching capabilities for 5G communication systems," *IEEE Access*, vol. 8, pp. 32531–32541, 2020.

[16] G. Raney, B. Unruh, R. Lovestead, and B. Winther, "64-Element 28 gigahertz phased array 5G prototyping platform," in *Proceedings of 2018 11th Global Symposium on Millimeter Waves (GSMM)*, pp. 1–4, Boulder, CO, USA, May 2018.

[17] U. Kodak, B. Rupakula, S. Zihir, and G. M. Rebeiz, "60-GHz 64- and 256-element dual-polarized dual-beam wafer-scale phased-array transceivers with reticle-to-reticle stitching," *IEEE Transactions on Microwave Theory and Techniques*, vol. 68, no. 7, pp. 2745–2767, 2020.

[18] P. Hindle, "Comprehensive survey of commercial mmWave phased array companies. Focused on SATCOM and 5G applications," *Microwave Journal*, 2020.

[19] M. Jones and P. Delos, "Integrated transceivers simplify design, improve phased array radar performance," *Microwave Journal*, 2020.

[20] M. Alibakhshikenari, F. Babaeian, B. S. Virdee et al., "A comprehensive survey on "various decoupling mechanisms with focus on metamaterial and metasurface principles applicable to SAR and MIMO antenna systems"," *IEEE Access*, vol. 8, pp. 192965–193004, 2020.

[21] A. Iqbal, O. A. Saraereh, A. W. Ahmad, and S. Bashir, "Mutual coupling reduction using F-shaped stubs in UWB-mimo antenna," *IEEE Access*, vol. 6, pp. 2755–2759, 2018.

[22] C. W. Carroll and B. V. K. Vijaya Kumar, "Iterative Fourier transform phased array radar pattern synthesis," *Proceedings of SPIE*, vol. 827, pp. 73–84, 1987.

[23] J. R. Fienup, "Phase retrieval algorithms: a comparison," *Applied Optics*, vol. 21, no. 15, pp. 2758–2769, 1982.

[24] S. J. Stirland, "Fast antenna synthesis by an iterative FFT procedure," in *Proceedings of 1991 21st European Microwave Conference*, pp. 745–750, Stuttgart, Germany, September 1991.

[25] W. P. M. N. Keizer, "Fast low-sidelobe synthesis for large planar array antennas utilizing successive fast Fourier transforms of the array factor," *IEEE Transactions on Antennas and Propagation*, vol. 55, no. 3, pp. 715–722, 2007.

[26] W. P. M. N. Keizer, "Affine transformation for synthesis of low sidelobe patterns in planar array antennas with a triangular element grid using the IFT method," *IET Microwaves, Antennas & Propagation*, vol. 14, no. 8, pp. 830–834, 2020.

[27] W. P. M. N. Keizer, "Element failure correction for a large monopulse phased array antenna with active amplitude weighting," *IEEE Transactions on Antennas and Propagation*, vol. 55, no. 8, pp. 2211–2218, 2007.

[28] W. P. M. N. Keizer, "Linear array thinning using iterative FFT techniques," *IEEE Transactions on Antennas and Propagation*, vol. 56, no. 8, pp. 2757–2760, 2008.

[29] W. Keizer, "Large planar array thinning using iterative FFT techniques," *IEEE Transactions on Antennas and Propagation*, vol. 57, no. 10, pp. 3359–3362, 2009.

[30] W. P. M. N. Keizer, "Amplitude-only low sidelobe synthesis for large thinned circular array antennas," *IEEE Transactions on Antennas and Propagation*, vol. 60, no. 2, pp. 1157–1161, 2012.

[31] W. P. M. N. Keizer, "Low-sidelobe pattern synthesis using iterative fourier techniques coded in MATLAB [EM programmer's notebook]," *IEEE Antennas and Propagation Magazine*, vol. 51, no. 2, pp. 137–150, 2009.

[32] W. P. M. N. Keizer, "Synthesis of scan- and frequency-invariant low-sidelobe tapers for planar array antennas," *IEEE Transactions on Antennas and Propagation*, vol. 64, no. 8, pp. 3703–3707, 2016.

[33] W. P. M. N. Keizer, "Low sidelobe phased array pattern synthesis with compensation for errors due to quantized tapering," *IEEE Transactions on Antennas and Propagation*, vol. 59, no. 12, pp. 4520–4524, 2011.

[34] W. P. M. N. Keizer, "Planar phased-array antennas: mutual coupling and ultralow peak sidelobes," *IEEE Antennas and Propagation Magazine*, vol. 61, no. 1, pp. 14–28, 2019.

[35] W. P. M. N. Keizer, "Synthesis of monopulse antenna patterns for elliptical phased array antennas with different peak sidelobes along the principal planes," *IEEE Transactions on Antennas and Propagation*, vol. 67, no. 9, pp. 5943–5950, 2019.

[36] Y. Lo and S. Lee, "Affine transformation and its application to antenna arrays," *IEEE Transactions on Antennas and Propagation*, vol. 13, no. 6, pp. 890–896, 1965.

[37] M. Skolnik, J. Sherman, and F. Ogg Jr., "Statistically designed density-tapered arrays," *IEEE Transactions on Antennas and Propagation*, vol. 12, no. 4, pp. 408–417, 1964.

[38] W. P. M. N. Keizer, "APAS: an advanced phased-array simulator," *IEEE Antennas and Propagation Magazine*, vol. 52, no. 2, pp. 40–56, 2010.

[39] W. P. M. N. Keizer, "Synthesis of thinned planar circular and square arrays using density tapering," *IEEE Transactions on Antennas and Propagation*, vol. 62, no. 4, pp. 1555–1563, 2014.

[40] R. Willey, "Space tapaering of linear and planar arrays," *IRE Transactions on Antennas and Propagation*, vol. AP-10, no. 4, pp. 369–377, 1962.

[41] E. K. Miller, "Synthesizing linear-array patterns via matrix computation of element currents," *IEEE Antennas and Propagation Magazine*, vol. 55, no. 5, pp. 85–96, 2013.

[42] E. K. Miller, "Synthesis of scanning and nonuniformly spaced dolph-chebyshev arrays," in *Proceedings of 2016 IEEE/ACES International Conference on Wireless Information Technology and Systems (ICWITS) and Applied Computational Electromagnetics (ACES)*, pp. 1-2, Honolulu, HI, USA, March 2016.

[43] J. Mautz and R. Harrington, "Computational methods for antenna pattern synthesis," *IEEE Transactions on Antennas and Propagation*, vol. 23, no. 4, pp. 507–512, 1975.

[44] S. Koziel and S. Ogurtsov, "Design of linear antenna array apertures using surrogate-assisted optimization," in *Simulation-Based Optimization of Antenna Arrays*, pp. 213–251, World Scientific Publication, London, UK, 2019, Chapter 10.

[45] S. Koziel and S. Ogurtsov, "End-fire array synthesis using gradient-based numerical optimization with analytical derivatives," in *Proceedings of 2012 Loughborough Antennas & Propagation Conference (LAPC)*, pp. 1–4, Loughborough, UK, November 2012.

[46] S. Koziel and S. Ogurtsov, "Linear Antenna Array Synthesis Using Gradient-Based Optimization with Analytical Derivatives," in *Proceedings of the 2012 IEEE International Symposium on Antennas and Propagation*, pp. 1-2, Chicago, IL, USA, July 2012.

[47] C. A. Balanis, *Antenna Theory: Analysis and Design*, Wiley, Hoboken, NJ, USA, 4th edition, 2016.

[48] Math Works, Inc., *Optimization Toolbox User's Guide*, The MathWorks, Inc., Natick, MA, USA, 2020.

[49] W.-C. Weng, F. Yang, and A. Z. Elsherbeni, "Linear antenna array synthesis using taguchi's method: a novel optimization technique in electromagnetics," *IEEE Transactions on Antennas and Propagation*, vol. 55, no. 3, pp. 723–730, 2007.

[50] D. Gies and Y. Rahmat-Samii, "Particle swarm optimization for reconfigurable phase-differentiated array design," *Microwave and Optical Technology Letters*, vol. 38, no. 3, pp. 168–175, 2003.

[51] S. Koziel and S. Ogurtsov, "Phase-spacing optimization of linear microstrip antenna arrays by em-based superposition models," in *Proceedings of 2014 Loughborough Antennas and Propagation Conference (LAPC)*, pp. 26–30, Loughborough, UK, November 2014.

[52] S. Koziel and S. Ogurtsov, "Phase-spacing optimization of linear microstrip antenna arrays using simulation-based surrogate superposition models," *International Journal of RF and Microwave Computer-Aided Engineering*, vol. 25, no. 6, pp. 536–547, 2015.

[53] S. Koziel and S. Ogurtsov, "Design of low-sidelobe arrays implementing required excitation tapers: the case of corporate

feeds comprising unequal-split junctions," in *Simulation-Based Optimization of Antenna Arrays*, pp. 328–354, World Scientific Publ., London, UK, 2019, Section 14.2.

[54] S. Koziel and S. Ogurtsov, "Fast simulation-driven optimization of planar microstrip antenna arrays using surrogate superposition models," *International Journal of RF and Microwave Computer-Aided Engineering*, vol. 25, no. 5, pp. 371–381, 2015.

[55] D. Caratelli and M. C. Viganó, "Analytical synthesis technique for linear uniform-amplitude sparse arrays," *Radio Science*, vol. 46, no. 4, pp. 1–6, 2011.

[56] D. Caratelli and M. C. Vigano, "A novel deterministic synthesis technique for constrained sparse array design problems," *IEEE Transactions on Antennas and Propagation*, vol. 59, no. 11, pp. 4085–4093, 2011.

[57] D. Caratelli, M. C. Viganó, G. Toso, P. Angeletti, A. A. Shibelgut, and R. Cicchetti, "A hybrid deterministic/metaheuristic synthesis technique for non-uniformly spaced linear printed antenna arrays," *Progress In Electromagnetics Research*, vol. 142, pp. 107–121, 2013.

[58] D. Caratelli, G. Toso, O. V. Stukach, and N. V. Panokin, "Deterministic constrained synthesis technique for conformal aperiodic linear antenna arrays-Part I: theory," *IEEE Transactions on Antennas and Propagation*, vol. 67, no. 9, pp. 5951–5961, 2019.

[59] D. Caratelli, G. Toso, O. V. Stukach, and N. V. Panokin, "Deterministic constrained synthesis technique for conformal aperiodic linear antenna arrays-Part II: applications," *IEEE Transactions on Antennas and Propagation*, vol. 67, no. 9, pp. 5962–5973, 2019.

[60] A. Kedar, "Deterministic synthesis approach for linear sparse array antennas," *IEEE Transactions on Antennas and Propagation*, vol. 68, no. 9, pp. 6667–6674, 2020.

[61] J. W. Hooker and R. K. Arora, "Optimal thinning levels in linear arrays," *IEEE Antennas and Wireless Propagation Letters*, vol. 9, pp. 771–774, 2010.

[62] A. Kedar and L. P. Ligthart, "Wide scanning characteristics of sparse phased array antennas using an analytical expression for directivity," *IEEE Transactions on Antennas and Propagation*, vol. 67, no. 2, pp. 905–914, 2019.

[63] S. Zhang, X. Chen, I. Syrytsin, and G. F. Pedersen, "A planar switchable 3-D-coverage phased array antenna and its user effects for 28-GHz mobile terminal applications," *IEEE Transactions on Antennas and Propagation*, vol. 65, no. 12, pp. 6413–6421, 2017.

[64] X. Chen, M. Abdullah, S. Zhang, T. Li, and Q. Li, "Mutual coupling reduction of slot array antenna for 5G millimeter-wave handset," in *Proceedings of 2019 Photonics & Electromagnetics Research Symposium-Fall (PIERS-Fall)*, pp. 1525–1530, Xiamen, China, December 2019.

[65] K. Kibaroglu, M. Sayginer, and G. M. Rebeiz, "A low-cost scalable 32-element 28-GHz phased array transceiver for 5G communication links based on a 2×2 beamformer flip-chip unit cell," *IEEE Journal of Solid-State Circuits*, vol. 53, no. 5, pp. 1260–1274, 2018.

[66] K. Kibaroglu, M. Sayginer, T. Phelps, and G. M. Rebeiz, "A 64-element 28-GHz phased-array transceiver with 52-dBm EIRP and 8-12-Gb/s 5G link at 300 meters without any calibration," *IEEE Transactions on Microwave Theory and Techniques*, vol. 66, no. 12, pp. 5796–5811, 2018.

[67] A. Nafe, M. Sayginer, K. Kibaroglu, and G. M. Rebeiz, "2 $\times$ 64-element dual-polarized dual-beam single-aperture 28-GHz phased array with 2 $\times$ 30 Gb/s links for 5G polarization MIMO," *IEEE Transactions on Microwave Theory and Techniques*, vol. 68, no. 9, pp. 3872–3884, 2020.

[68] M. K. Leino, R. Montoya Moreno, J. Ala-Laurinaho, R. Valkonen, and V. Viikari, "Waveguide-based phased array with integrated element-specific electronics for 28 GHz," *IEEE Access*, vol. 7, pp. 90045–90054, 2019.

[69] B. Rupakula, S. Zihir, and G. M. Rebeiz, "Low complexity 54-63-GHz transmit/receive 64- and 128-element 2-D-scanning phased-arrays on multilayer organic substrates with 64-QAM 30-gbps data rates," *IEEE Transactions on Microwave Theory and Techniques*, vol. 67, no. 12, pp. 5268–5281, 2019.

[70] M. K. Leino, J. Bergman, J. Ala-Laurinaho, and V. Viikari, "Beam optimization for 28 GHz phased array utilizing measurement data," in *Proceedings of 2020 14th European Conference on Antennas and Propagation (EuCAP)*, pp. 1–5, Copenhagen, Denmark, March 2020.

[71] Y. Yin, S. Zihir, T. Kanar et al., "A 37-42-GHz 8×8 phased-array with 48-51-dBm EIRP, 64-QAM 30-Gb/s data rates, and EVM analysis versus channel RMS errors," *IEEE Transactions on Microwave Theory and Techniques*, vol. 68, no. 11, pp. 4753–4764, 2020.

[72] A. H. Aljuhani, T. Kanar, S. Zihir, and G. M. Rebeiz, "A scalable dual-polarized 256-element Ku-band SATCOM phased-array transmitter with 36.5 dBW EIRP per polarization," in *Proceedings of 2018 48th European Microwave Conference (EuMC)*, pp. 938–941, Madrid, Spain, September 2018.

[73] X. Gu, D. Liu, C. Baks et al., "Development, implementation, and characterization of a 64-element dual-polarized phased-array antenna module for 28-GHz high-speed data communications," *IEEE Transactions on Microwave Theory and Techniques*, vol. 67, no. 7, pp. 2975–2984, 2019.

[74] G. Gültepe, S. Zihir, T. Kanar, and G. M. Rebeiz, "A dual-polarized 1024-element Ku-band SATCOM transmit phased-array with ±70° scan and 43.5 dBW EIRP," in *Proceedings of 2020 IEEE/MTT-S International Microwave Symposium (IMS)*, pp. 837–840, Los Angeles, CA, USA, August 2020.

[75] K. Park, J. Myeong, G. M. Rebeiz, and B.-W. Min, "A 28-GHz full-duplex phased array front-end using two cross-polarized arrays and a canceller," *IEEE Transactions on Microwave Theory and Techniques*, vol. 69, no. 1, pp. 1127–1135, 2021.

[76] Y. Yin, B. Ustundag, K. Kibaroglu, M. Sayginer, and G. M. Rebeiz, "Wideband 23.5-29.5-GHz phased arrays for multistandard 5G applications and carrier aggregation," *IEEE Transactions on Microwave Theory and Techniques*, vol. 69, no. 1, pp. 235–247, 2021.

[77] S. Koziel and S. Ogurtsov, "Design of linear phased array apertures using response correction and surrogate-assisted optimization," in *Simulation-Based Optimization of Antenna Arrays*, pp. 357–371, World Scientific Publication, London, UK, 2019, Chapter 15.

[78] B. Peterson and D. Schnaufer, "5G fixed wireless access array and RF-front end trade-offs," *Microwave Journal*, 2018.

Hindawi
International Journal of Antennas and Propagation
Volume 2021, Article ID 5559765, 18 pages
https://doi.org/10.1155/2021/5559765

Review Article

A Review of Antenna Array Technologies for Point-to-Point and Point-to-Multipoint Wireless Communications at Millimeter-Wave Frequencies

G. Federico,[1,2] **D. Caratelli**,[1,2] **G. Theis**,[1,2] **and A. B. Smolders**[2]

[1]*Department of Research and Development, The Antenna Company, 5656 AE, Eindhoven, Netherlands*
[2]*Department of Electrical Engineering, Eindhoven University of Technology, 5600 MB, Eindhoven, Netherlands*

Correspondence should be addressed to G. Federico; g.federico@tue.nl

Received 15 January 2021; Revised 15 March 2021; Accepted 28 March 2021; Published 22 April 2021

Academic Editor: Shah Nawaz Burokur

With the introduction of 5G communication systems operating in the mm-wave frequency range, new opportunities in terms of multimedia services and applications will become available. For this to happen, several technical challenges from an antenna standpoint need to be addressed. The achievements of high-gain characteristics and agile beamforming with wide-scan capabilities are the main targets of the ongoing research on mm-wave antenna arrays. In this paper, an up-to-date overview of antenna array technology for wireless communications at mm-wave frequencies is given. Particular focus is put on the review of the state-of-the art and most advanced antenna array concepts for point-to-point and point-to-multipoint radio links at said frequencies. Various figures of merit are assessed for a comprehensive analysis and bench marking of the technical solutions investigated in the presented survey.

1. Introduction

Wireless data traffic is exponentially increasing and such trend is expected to continue in the coming years. The capacity limit of wireless networks operating in the sub-6 GHz frequency band is effectively reached. As a matter of fact, most of the commercial radio-communication infrastructures, including AM/FM and high-definition TV broadcasting, as well as GPS, satellite, cellular, and Wi-Fi communications, are confined in relatively narrow portions of the spectrum between 300 MHz and 3 GHz where electromagnetic propagation conditions are more favorable, and low-cost semiconductor technology is readily available [1]. Said frequency range, however, is nowadays excessively crowded. For this reason, a significant effort has been put in place for the development of wireless communication systems operating at mm-wave frequencies, where larger bandwidth is available so to satisfy future capacity needs. The main advantages of communication systems operating at mm-waves can be summarized as follows [2]:

(i) Extremely wide bandwidths: compared to the frequency bands between 300 MHz and 3 GHz, mm-wave applications can benefit from wider portions of spectrum and, therefore, data rates.

(ii) Antenna size: the physical size of radiating elements decreases proportionally to the wavelength, allowing for integration of antennas and RF electronics to realize small form-factor devices.

(iii) Electromagnetic energy focusing: by virtue of the reduced operating wavelength, large-scale antenna arrays with more than 100 elements can be integrated into relatively small physical areas, allowing for adaptive beamforming to synthesize narrow beams with enhanced directivity characteristics which are instrumental to the delivery of better quality of service in real-life operative scenarios [3].

Wireless communications at mm-wave frequencies, however, also come with certain drawbacks, such as higher sensitivity to radio-wave blockage and larger propagation

losses. Furthermore, because of the specific quasioptical behavior of the electromagnetic field that dominates the physical layer, dedicated protocols in the MAC layer have to be developed [4] and adopted in order to achieve very low latency and high data rates [5]. At mm-waves, severe path losses are experienced in combination with a significant attenuation due to the impact of oxygen absorption (mainly in the 60 GHz band), blockage, precipitation, and foliage (associated with the presence of trees obstructing the radio link) [6]. However, several studies have confirmed that, for small distances (less than 1 km), rain attenuation has reduced impact on the distribution of the electromagnetic field radiated by small cells operating in the frequency range between 28 GHz and 38 GHz [7].

The unique characteristics of radio-wave propagation at mm-wave frequencies make the antenna one of the most critical elements in the overall system [8]. The higher level of antenna integration enabled by the higher frequencies of operation comes with the challenge of dealing with reduced tolerance to fabrication errors and more complex requirements for the materials employed. The antenna performance is obviously also affected by the characteristics of the circuitry embedded in the system, such as the feeding network to interconnect different components, or by the limitations in the active devices, like power and low-noise amplifiers. Another challenge in the design process at mm-waves is the characterization and testing of integrated antenna systems which, at such small wavelengths, are more sensitive to misalignment errors, temperature, and mechanical vibrations that, in turn, can result in additional losses, as well as amplitude and phase errors. More information on mm-wave antenna characterization can be found in [9], where a detailed analysis of measurement uncertainties at mm-wave frequencies is provided.

Many surveys and scientific papers concerning different aspects of the mm-wave technology have appeared in the literature during the last years. In [10], Wang et al. discussed the technical challenges faced in relation to phase noise and large-scale attenuation. In [11], Rappaport et al. provided an overview of the evolution of cellular and Wi-Fi networks with a detailed description of propagation channel models. In [12], Ghosh and Sen reported an inclusive survey on antenna array architectures. In [13], Hong et al. covered the aspects relevant to multibeam reflector-based array technology enabled by different phase-shifting techniques. Finally, in [14], Hong et al. described practical solutions for the integration of mm-wave phased-array antennas with beam-switching capabilities.

In this study, we focus on the review of different antenna array solutions classified according to the underlying technology. In particular, a detailed analysis of advanced arrays used for wireless communications at mm-wave frequencies is provided. Such an overview is, based on our knowledge, not published before in the open literature. The paper is organized as follows. In Section 2, useful design considerations are given together with some comments on the main challenges faced during the development of mm-wave array systems. Section 3 provides a description of the suitable antenna technologies employed at mm-wave frequencies, highlighting the relevant advantages and disadvantages. In the subsequent sections, an extensive review is made of the state of the art of mm-wave antenna arrays for two specific use cases: point-to-multipoint (PtM) and point-to-point (PtP) wireless communications. Finally, concluding remarks are given in Section 7.

2. Design Considerations for MM-Wave Antennas

The next generation of wireless communication systems aims to support low latency and high data rates with extended coverage for a wide variety of applications, including sensor networks, smart buildings, and mobile devices [15]. The expression of the channel capacity is provided by the following equation [16]:

$$C = B \log_2\left[1 + \left(\frac{\lambda_0}{4\pi r}\right)^2 G_{Tx} G_{Rx} \frac{P_t}{N_0}\right], \tag{1}$$

which shows that the achievement of higher data rates is only possible by increasing the operational bandwidth (B) and the antenna gain at the transmit and/or receive ends (G_{Tx}, G_{Rx}) and by enhancing the signal-to-noise ratio (P_t/N_0). This explains the benefit associated with the use of the mm-wave spectrum, though at the cost of a larger free-space attenuation. In order to further improve the channel capacity, one can also enable multiple spatial data streams by supporting, concurrently, different beams and dual polarization at both the transmitter and receiver.

A key requirement of the antenna solutions for mm-wave communications is to feature high-gain characteristics so as to compensate for the significant propagation losses experienced at the considered frequencies. The solution to this challenge consists in the integration of antennas in array configuration [17], in combination with a sufficiently high density of deployment of cells in a given network. Upon increasing the number of radiating elements in an antenna array, one can increase directivity and thereby focus the radiated power in a given direction. The most common array structures are in rectangular/square configuration. A $M \times N$ planar array is shown in Figure 1, together with the coordinate system used as a reference in the rest of the document.

In order to achieve adequate radio coverage of the operating environment, it is imperative to perform an accurate link budget analysis. A key parameter in this respect is the path loss, which determines the level of attenuation of the radiated energy following the electromagnetic propagation process in the radio channel. Different models are available in the literature for the estimation of the path loss between transmitter and receiver. Of particular interest are the Close-In (CI) and the Alpha-Beta-Gamma (ABG) models which rely on experimental measurement data [18, 19]. An accurate evaluation of the link budget in Line-of-Sight (LOS) and Non-Line-of-Sight (NLOS) propagation scenarios for 5G-and-beyond communications is reported, also, in [20, 21] based on the 3GPP standard [22].

The main figures of merit that define the performance of an antenna array, as per the illustrations in Figure 2, are used

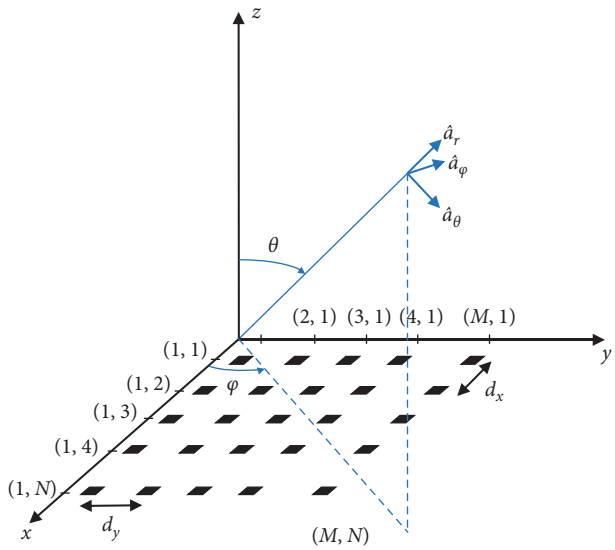

Figure 1: Schematic of a regular $M \times N$ planar array in a spherical coordinate system.

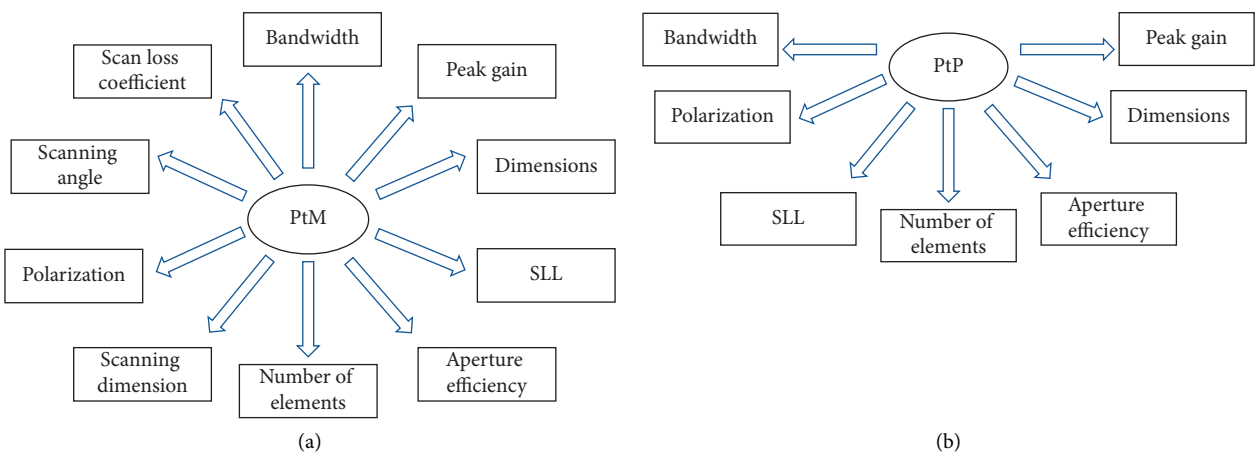

Figure 2: Figures of merit for the analysis of antenna arrays for (a) point-to-multipoint (PtM) communications and (b) point-to-point (PtP) communications.

in the following sections for bench marking of the technical solutions investigated in this review. For convenience, two different scenarios (PtP and PtM communications) have been examined in order to provide a more meaningful overview of the different antenna concepts considered here. Each operative scenario requires indeed different radiation characteristics.

When developing antenna arrays for PtP wireless communications, the main concern is to achieve high-gain characteristics in order to compensate for the propagation losses at mm-waves and obtain, in this way, a stable radio link while avoiding unexpected misalignment between the transmitter and receiver. Examples of PtP systems are found in midrange networks such as mm-wave backhaul/fronthaul as well as board-to-board communications. When an antenna array is used, instead, for PtM communications, one of the main challenges is to achieve wide-angle beam scanning. This allows minimizing the number of array antenna panels necessary to enable proper coverage of the operating environment and, in this way, reducing the overall system costs. A relevant example in this respect is given by 5G base stations (BSs) that have to ensure a suitable 360° coverage of multiple users while they are in motion (as illustrated in Figure 3). In this case, in accordance with the aforementioned propagation loss models, one should target values of peak gain of about 26 dBi in order to enable a reliable quality of service up to 100 m in the frequency band at 28 GHz, as well as a scanning range of at least ±60° so to limit the required number of sectors to three or four (including some overlap margin). In this and several other operative scenarios, besides the wide-angle scanning capability, it is key to have antenna array solutions that feature stable gain and low Side-Lobe Level (SLL) characteristics. In addition to that, an important aspect to take into account during the design stage is the appearance of grating lobes. With reference to a uniformly spaced planar antenna array, the following criterion is typically enforced to avoid the formation of grating lobes [8]:

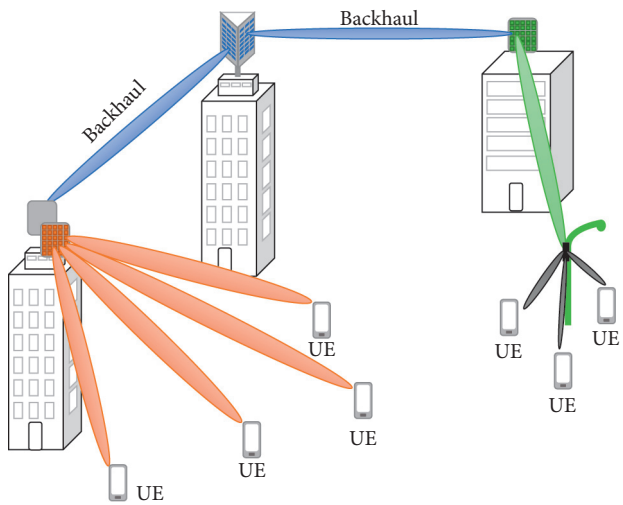

Figure 3: 5G wireless communication scenario where the use of PtP and PtM systems is shown in order to set up a communication system with user equipment (UE).

$$d_x, d_y < \frac{\lambda_0}{1 + \sin\theta_{\max}}, \tag{2}$$

where d_x and d_y denote the interelement separation along the horizontal and vertical directions, respectively, λ_0 is the wavelength in free space at the highest operational frequency, and θ_{max} is the maximal steering angle along each of the scan planes; that is, $\phi = 0^\circ$ and $\phi = 90^\circ$ (see also Figure 1). As it can be inferred from (2), grating lobes can be avoided by using a dense array grid. This can, however, cause unwanted high mutual coupling which, in turn, affects the array performance negatively. While scanning, broadside antenna arrays are subjected to a degradation of the main-lobe gain due to the aperture projection loss [23]. In ideal conditions, the gain degradation while scanning off boresight, also referred to as scan power loss, follows the $\cos\theta$ law. In real life, because of the impact of parasitic mutual coupling, scan loss is actually more severe and can be effectively modeled as $\cos^n\theta$, where n is a real-valued parameter larger than 1. The following considerations can be made [23]:

(i) The main-lobe gain decays at least as $\cos\theta$ while scanning in different directions.

(ii) A broadside array cannot scan up to the end-fire direction since $\cos(\pi/2) = 0$. Dedicated arrays should be designed to ensure end-fire coverage.

Grating lobes avoidance, high isolation between antenna elements, and stable gain over the scanning range are among the most relevant challenges and somehow conflicting requirements in the design of wide-angle scanning arrays.

An important figure of merit for antenna arrays is the active reflection coefficient (Γ_{A_m}), which provides an effective means for evaluating antenna return-loss characteristics inclusive of mutual coupling effects while scanning [24]. For the general m^{th} array element, Γ_{A_m} can be calculated as

$$\Gamma_{A_m} = \sum_{n=1}^{N} \frac{a_n}{a_m} S_{mn}, \quad m = 1, \ldots, N_a, \tag{3}$$

where N_a is the overall number of antenna elements, a_n and a_m denote the incident waves at the input terminals of the nth and m^{th} array element, respectively, and S_{mn} denotes the coupling coefficient. The operational bandwidth of a phased-array antenna is typically defined as the frequency range where the magnitude of the active reflection coefficient is below −10 dB. Blindness ($|\Gamma_{A_m}| \simeq 1$) may occur while scanning due to spurious coupling between antenna elements [24]. A detailed analysis of mutual coupling in phased arrays is provided in [25].

Among various aspects, the attainment of high efficiency over the entire frequency band of operation is important to enable effective power management at system level. With the billions of objects wirelessly connected to upcoming 5G communication networks, it becomes indeed crucial to reduce the power consumption of the individual devices and components.

3. Antenna Concepts and Technologies

The different antenna concepts available in the scientific literature offer a variety of design choices for array antennas which, with different characteristics, can strongly affect the overall system performance. An overview of the advantages and disadvantages of commonly used antenna elements integrated into mm-wave arrays is reported in Table 1.

Microstrip patch antennas are relatively easy to manufacture using technologies which are commonly available in industry [26]. They represent a quite versatile solution in several applications which require pencil beams, fan beams, or omnidirectional radio coverage. The antenna polarization, whether it is linear or circular, can be controlled in rather simple ways. Furthermore, microstrip antennas can conform to the shape of the hosting platform on flat or curved surfaces [27, 28]. Patch antennas are particularly suitable for PtM communications, since they feature a radiation pattern with broad coverage that is instrumental to the achievement of wide-angle scanning properties at array level.

Thanks to their characteristics, *Vivaldi antennas* [29] may represent a valid alternative to other antenna solutions in different applications. One of the main advantages of this type of antennas is the broadband behavior [30]. Vivaldi antennas are typically printed on dielectric substrates, thus making the relevant integration with other components of easier implementation. Vivaldi antennas have been extensively studied in literature with various design improvements [31, 32]. Many techniques have been developed to enhance the gain of this class of antennas, such as those based on the use of dielectric lenses [33–35], metamaterial lenses [36], and parasitic elliptical patches [37]. As Vivaldi antenna, end-fire radiation can also be realized with printed *dipole* or *bow-tie* antenna arrays, which have a similar built-up as shown in [38].

Table 1: Advantages and disadvantages of commonly used antenna technologies for array development.

Technology	Advantages	Disadvantages
Patch	(i) Integration (ii) Low cost	(i) Losses (ii) Isolation
Vivaldi	(i) Wideband (ii) High gain	(i) Bulky
DRA	(i) No conductor loss (ii) High efficiency	(i) Manufacturing precision
Open-ended waveguide	(i) Stable radiation pattern (ii) High efficiency	(i) Bulky (ii) High costs
Gap waveguide	(i) Low losses (ii) Wideband	(i) Design complexity
Resonant cavity	(i) High gain (ii) Low cost	(i) Narrow 3 dB gain bandwidth

Dielectric resonator antennas (DRAs) display excellent characteristics for high-frequency applications and in particular for mm-wave communications and remote sensing [39]. DRAs feature low losses, high efficiency, and wide bandwidth and can support multiple polarizations, as well as diverse radiation patterns by excitation of suitable resonant modes [40, 41]. The DRA size is proportional to $\lambda_0/\sqrt{\epsilon_r}$, which translates into the possibility of controlling the antenna dimensions by properly selecting the relative permittivity (ϵ_r) of the material forming the basic dielectric resonator. DRAs are easy to fabricate and enable good design flexibility based on different geometries. One of the main characteristics of DRAs is the absence of conduction losses, which makes them a very promising candidate for mm-wave applications [42]. Electrically large DRAs exploiting higher-order propagation modes are used to enhance antenna gain. At the same time, one should notice that the bandwidth is inversely proportional to the relative permittivity, and this may limit the choice of dielectric materials for a given application [43].

Thanks to high-gain and high-efficiency characteristics, *open-ended waveguide antennas* are largely employed in array configuration for mm-wave applications. This type of antennas, however, is not very attractive for commercial applications at mm-wave frequencies above 60 GHz because of the inherently high manufacturing costs, bulky dimensions, and less easy integration with a chip or in a package as compared to other technologies [15]. Nowadays, some of these limitations have been overcome thanks to the concept of *substrate-integrated waveguide* (SIW). The advantages of conventional waveguides are preserved with SIW structures. The SIW technology has recently replaced the conventional transmission lines in mm-wave communications due to favorable propagation characteristics, such as high-Q factor and high power handling capability [44]. The most important advantage of SIW technology is represented by the possibility of enabling full integration of all the system components on the same substrate [45]. Since SIW components are bounded by conducting surfaces on both sides of the substrate, they exhibit extremely low (completely negligible) spurious radiation losses and insensitivity to outer electromagnetic interferences (EMIs) [46]. *Gap-waveguides* are also presented in the technical literature as a possible solution for mm-wave wireless communications [47]. Gap-waveguide technology offers indeed good performance at mm-wave frequencies thanks to the relevant low-loss characteristics. Gap-waveguiding structures rely on the propagation of electromagnetic waves between two parallel metal plates, while the propagation direction is controlled through metal pins that do not have electrical contact with the lid that covers them [48]. The losses in gap-waveguides are comparable to the losses in conventional waveguides.

Resonant cavity antennas (RCAs) can also be a class of antennas to be considered for mm-wave applications. RCAs feature very high-gain characteristics with the drawback of a narrow gain bandwidth at 3 dB level. An extensive review of RCAs for 5G wireless communications is provided in [49].

4. Wide-Angle Scanning Antenna Arrays for PtM Communications

In this section, we provide an extensive review and comparison of the most common wide-angle scanning antenna array technologies available at mm-waves for PtM communications. The antenna array solutions considered here are detailed in Table 2 where the relevant figures of merit (see Figure 2(a)) are evaluated. The aperture efficiency (η_{eff}), as reported in Table 2, is calculated starting from the antenna gain characteristics through the following formula [50]:

$$\eta_{\text{eff}} = \frac{G\lambda_0^2}{4\pi A_{\text{phys}}}, \tag{4}$$

where G denotes the peak gain at the boresight and A_{phys} is the physical area of the antenna structure.

The scan loss of the relevant antenna arrays analyzed in this review is illustrated in Figures 4(a) and 4(b) along the azimuth plane and the elevation plane, respectively, and compared to the ideal case with $\cos\theta$ behavior. One can notice that the state-of-the-art solutions have scanning capabilities up to $\pm 60^\circ$ but at the cost of at least 4 dB scan loss.

In [51], a 5G communication link at 28 GHz is demonstrated using a 64-element (8×8) phased-array consisting of stacked patch antennas. The design is based on four-channel (2×2) transmit/receive (TRX) beamforming chips in SiGe BiCMOS technology with 6-bit phase control.

Table 2: State of the art of antenna arrays for PtM mm-wave wireless communications.

Antenna technology	Bandwidth (GHz)	Peak gain (dBi)	Dimensions (mm^2)	SLL (dB)	Aperture efficiency (%)	Number of elements	Dimension of beam scanning	Polarization	Max scan angle	Scan loss coefficient
Stacked patch [51]	28–32	22.5	50×63	−10	57	8×8	Azimuth and elevation	Single	Az.: ±50° El.: ±25°	Az.: $n = 1.5$ El.: NA
Patch on PCB [52]	26–31.4	12	23×23	−8	26	4×4	Azimuth	Dual	Az.: ±42°	Az.: $n = 2$
Dipole [56]	26.5–29.5	12	NA	−9	NA	8×1	Azimuth	Single	Az.: ±50°	Az.: $n = 2$
Patch [57]	57–66	21.5	14.1×22.4	−11	85	48	Azimuth and elevation	Single	Az.: ±60° El.: ±10°	Az.: $n = 1.7$ El.: NA
AiP patch/ dipole for UE [59]	28–29.5	14	NA	−7	NA	2×4	Azimuth and elevation	Dual	Az.: ±45° El.: ±45°	Az.: $n = 2$el.: $n = 1.7$
AiP patch for UE [61]	27.5–29.5	14	11.6×22	−8	79	2×4	Azimuth	Dual	Az.: ±30°	Az.: $n = 1.7$
Patch for BS [62]	28–32	24	70×70	−9	47	8×8	Azimuth and elevation	Dual	Az.: ±50° El.: ±50°	Az.: $n = 2$el.: $n = 1.5$
AiP patch [65]	80–100	30	45×45	−8	44	384	Azimuth and elevation	Dual	Az.: ±20° El.: ±30°	Az.: $n = 4.2$ El.: $n = 4.7$
Vivaldi for UE [66]	27.4–28.6	12	60×130	−10	30	1×8	Azimuth	Single	Az.: ±70°	Az.: $n = 0.5$
DRA for BS [68]	26–30	23.5	63.1×69.4	−12	44	8×8	Azimuth and elevation	Dual	Az.: ±60° El.: ±60°	Az.: $n = 1.5$ El.: $n = 1.5$
Gap waveguide [69]	26.5–31	24	135×122	−12	13	16×16	Azimuth and elevation	Dual	Az.: ±45° El.: ±10°	Az.: $n = 2$ El.: NA
Horn for BS [70]	26.5–29.5	24	50×50	−13	90	8×8	Azimuth	Single	Az.: ±45°	Az.: $n = 1.7$
FPA [77]	20–40	43	830×255	−12	80	200	Azimuth	Single	Az.: ±20°	NA

Sixteen chips are integrated on a 12-layer Printed Circuit Board (PCB) which includes a suitable Wilkinson power dividing/combining network. The antenna elements are spaced 5 mm (about $0.5\lambda_0$ at 30 GHz) apart in the horizontal direction and 6.3 mm (about $0.63\lambda_0$ at 30 GHz) apart in the vertical direction, as shown in Figure 5. The selected interelement spacing enables a maximal scan angle up to ±50° along the azimuth plane and up to ±25° along the elevation plane while achieving relatively low SLLs (below −10 dB) in combination with a peak gain of 22.5 dBi and a bandwidth of 4 GHz (from 28 GHz to 32 GHz). The antenna array is characterized by an Effective Isotropic Radiated Power (EIRP) of 50 dBm and is designed in such a way as not to require a dedicated calibration network. It has been tested and verified for radio links over a distance of up to 300 m.

A wideband patch antenna array that can support two linear orthogonal polarizations concurrently is presented in [52]. The antenna array is formed by 16 elements in a 4×4 configuration which is optimized so to operate in the frequency band between 26 GHz and 31.4 GHz. As known from theory, conventional rectangular or circular patch antennas typically feature a rather limited fractional bandwidth, up to about 7% [53]. In [52], a broader band of operation is achieved by realizing circular cutouts at the four corners of the basic square patch (see Figure 6). The individual radiating element has maximal dimensions of 2.65 mm × 2.65 mm, whereas the radius of the cutouts is 0.95 mm. The antenna element is excited by two feeding pins in order to support dual linear polarization. In the final 4×4 array configuration, the antenna elements are spaced 5.5 mm (about $0.57\lambda_0$ at 31.4 GHz) apart from each other along both the horizontal and vertical directions. The array beam-steering network is based on a Butler Matrix (BM) [54, 55], which is implemented on a circuit board with dimensions of 120 mm × 70 mm × 1.62 mm. The array is characterized by a maximal scan angle of ±42° and a peak gain level of 12 dBi.

A microstrip array dipole-based operating in the 28 GHz frequency band is detailed in [56]. A PTFE board of 15 printed dipoles is used to construct an array in a 15×8 configuration. The antenna elements are connected to the PCB through SMPM connectors and kept at a center-to-center distance of 6 mm. This supports a beam-scanning range beyond ±50° in the azimuth plane, in combination with a saturated EIRP of 39.8 dBm at the boresight.

A tile-based array for backhaul applications at 60 GHz has been presented in [57]. The unit cell consists of a slot-coupled microstrip patch that is parasitically loaded by four auxiliary patches (forming an H-shape). The position of the auxiliary patches has been chosen so to broaden the operational bandwidth while achieving an active reflection coefficient with magnitude below −10 dB in the frequency range between 57 GHz and 66 GHz. A tile with 48 unit cells is designed in a 6×8 array configuration. Measurements carried out on the individual tile have shown a peak gain of

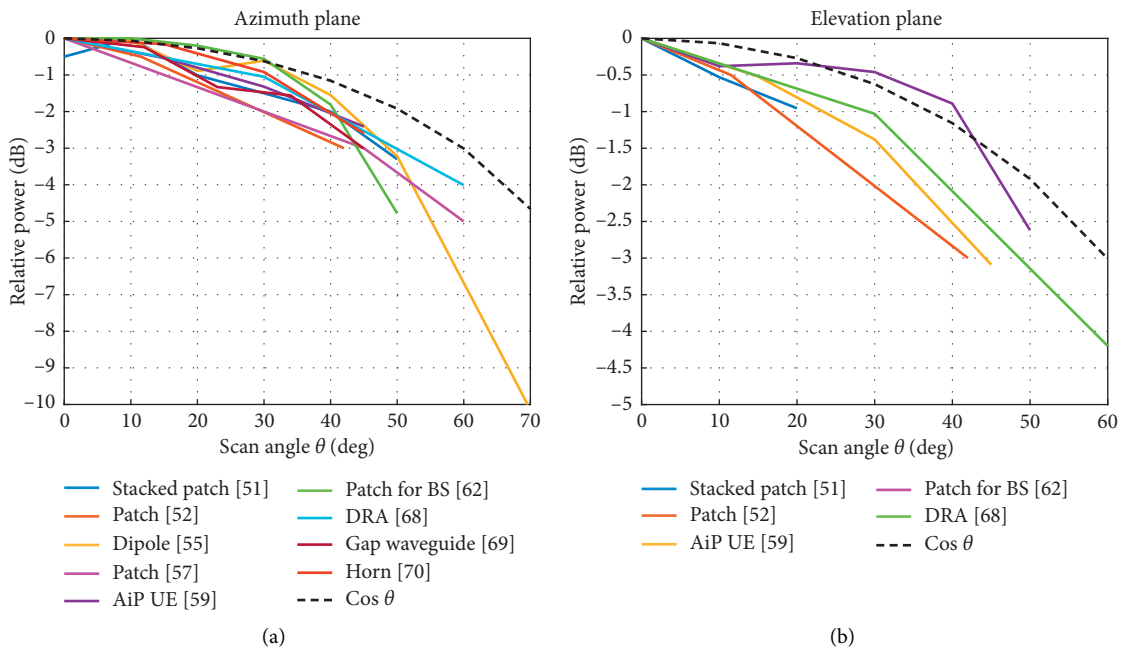

Figure 4: Scan loss of the most relevant antenna arrays along the azimuth plane (a) and the elevation plane (b).

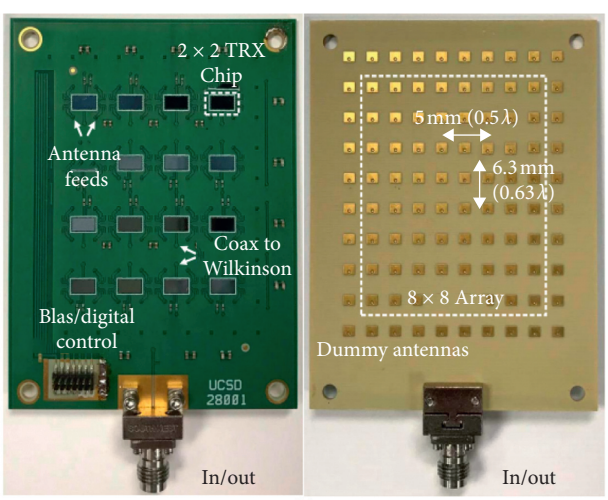

Figure 5: Top and bottom views of the 12-layer 64-element phased-array Printed Circuit Board (PCB) [51] ©2018 IEEE.

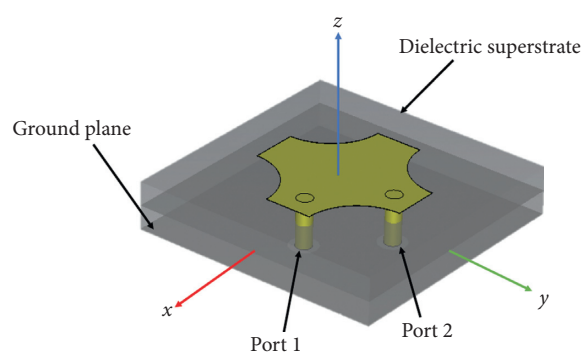

Figure 6: Patch element with angular circular cutouts of the 4 × 4 array configuration proposed in [52].

about 22 dBi at the boresight, which drops by 3 dB at ±45° and by 5 dBi at ±60° while scanning in the azimuth plane. When six of the aforementioned 48-element tiles are placed together in two rows to form a 288-element array, a peak gain of 29.5 dBi is achieved.

As documented in the previous section, microstrip antennas are particularly suitable for close integration with circuit components such as amplifiers and switches, so to realize an Antenna-in-Package (AiP) [58]. The need for AiP technology is going to increase dramatically for applications at mm-wave frequencies and beyond. AiPs are already being widely employed for 5G cellular network deployment at 28 GHz [59, 60]. In [59], a relevant phased-array transceiver with 24 channels and dual-polarization support is described. The UE module relies on different antenna array configurations, such as 1 × 4 dipole arrays and 2 × 4 patch arrays with integrated radio frequency integrated circuits (RFICs). The BS makes use of a 4 × 4 patch antenna array with 2 rows of dummy elements on one edge. Measurements carried out on the UE module with 2 × 4 integrated array have shown an uncalibrated scan range up to ±45° for both the horizontal and vertical polarization channels along the azimuth plane, whereas the achieved peak EIRP level is 35 dBm for horizontal polarization and 34 dBm for vertical polarization.

A similar dual-polarized design for UE (see Figure 7) is proposed in [61]. The relevant 2 × 4 patch antenna array with dual feeds is integrated into a Flip Chip-Chip Scale Package (FC-CSP) with a relative permittivity of 3.9 and 8 metal layers having a thickness of 800 μm and a total area of 11.6 mm × 22 mm. The separation between antenna

elements is equal to 5.25 mm (i.e., $\lambda_0/2$ at the center frequency of 28.5 GHz). The individual antenna element occupies an area of 2.35 mm × 2.35 mm and features an average peak gain of 5 dBi when integrated into an array configuration. The complete array displays a peak gain along the broadside direction of about 14 dBi with a scan range of ±30° along the azimuth plane. In the frequency band between 27.5 GHz and 29.5 GHz, the maximum EIRP of the considered array is 31.5 dBm.

An antenna module operating at 28 GHz is proposed in [62] and is shown in Figure 8. In this design, the multilayered phased-array antenna consists of 64 dual-polarized active patch antennas and 36 dummy elements. The dummy elements are placed along the periphery of the array, whereas the active elements are fed by 4 RFICs. An air cavity is implemented underneath all the array elements to improve bandwidth and, at the same time, suppress spurious antenna coupling processes. The measured peak gain of the individual antenna element is about 7 dBi at 30.5 GHz. The array is claimed to scan from −50° to ±50° and features an EIRP larger than 50 dBm. The module has a size of 70 mm × 70 mm with a thickness of 2.3 mm.

AiP technology is being broadly employed, also, for smart sensing and short-range wireless communications in the 60 GHz band. An example of this is reported in [63], where a package that integrates 6 patch antennas is designed in such a way so as to deliver a combined gain of about 10 dBi. Thanks to the very compact dimensions, namely, 14 mm × 14 mm × 0.8 mm, the aforementioned AiP has the potential of being integrated into a wide range of wearable devices [64].

The use of W-band technology for 5G applications has been investigated in [65] using a scalable tile-based phased-array architecture. The individual tile consists of a 5 × 5 aperture-stacked patch antenna array which is partitioned into 16-element and 8-element subarrays, in addition to a dummy element. The antenna spacing is selected to be $0.63\lambda_0$ at 90 GHz (i.e., 2.1 mm) along both the vertical and horizontal directions. In order to avoid grating lobes while scanning, it is advisable to keep the array elements at a separation smaller than or equal to $0.5\lambda_0$. However, such layout could not be implemented in [65] because of the physical constraints set by the adopted RFIC solution as well as by the limitations of the adopted PCB manufacturing process. The developed single tile covers the frequency range from 80 GHz to 100 GHz, with simulated directivity, gain, and efficiency better than 18.5 dBi, 18 dBi, and 87%, respectively. The integration of 16 array tiles results in a total EIRP level of 60 dBm and a beamwidth of less than 4° at 90.7 GHz. The 2D beam-steering function can be achieved by integrating any number of tiles.

Vivaldi antenna arrays have been proposed for 5G mobile terminals in [66]. The design consists of 8 antenna elements integrated along the edge of the device PCB and optimized in such a way so as to feature a central working frequency of 28 GHz with an operational bandwidth larger than 1 GHz. The array is characterized by a scan range up to ±70° with a total efficiency of more than 84%. The peak gain of the array beam is shown to be nearly flat around 12 dBi over the scan range from the boresight to ±40°.

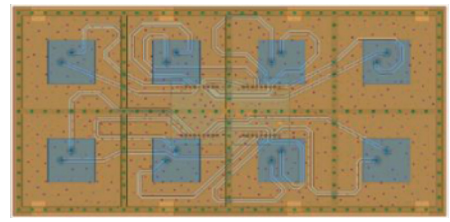

Figure 7: Antenna array for UE proposed in [61] ©2017 IEEE.

Another interesting solution for wide-angle scanning arrays is represented by DRA technology. The introduction of DRAs in literature dates back to 1983 when Long et al. presented the first detailed mode analysis of resonant cylindrical dielectric cavities in [67]. After that, DRAs have been used in a variety of applications over a wide frequency range, from 55 MHz up to 340 GHz [43]. A relevant study concerning the application of DRA technology in mm-wave antenna arrays for 5G applications is proposed in [68]. The array demonstrator discussed in the said study is shown in Figure 9. Each parallelepipedal DRA element forming the array structure is fed by a slot aperture which, in turn, is excited by proximity coupling through a dedicated microstrip line. The array elements are placed along a uniformly spaced 8 × 8 grid on the top of a feeding network integrated into a PCB with an overall size of 63 mm × 69 mm. It is shown that a total efficiency larger than 80% is achieved in the frequency band from 28 GHz to 30 GHz in combination with a maximal scan range of ±60° along both the azimuth and elevation planes. The realized gain displayed by the array along the broadside direction is about 23 dBi at 28 GHz, with a minimum level of 21.5 dBi across the frequency range from 24 GHz to 30 GHz.

A relevant design solution for 5G BSs based on gap-waveguide technology is presented in [69]. In this research, a slotted-waveguide array antenna is implemented by means of a fully integrated all-metal multilayered assembly. Waveguide-like feeding lines are realized using artificial magnetic conductors, without the need for electrical connections between the layers forming the array structure. This enables the integration with substrate-based components. The radiating antenna layer consists of an 8 × 8 array of slots and is characterized by an active reflection coefficient with a magnitude below −10 dB in the wide frequency range from 26.5 GHz to 31 GHz. The array features a peak main-lobe gain of 23 dBi with a maximum scan range of ±45° along the azimuth plane and ±10° along the elevation plane.

In [70], a phased-array based on compact horn antennas is proposed. Such an array is optimized for operation in the 26.5 GHz–29.5 GHz frequency band. A 2 × 2 subarray is used as a building block to realize a scalable $M \times N$ array. In the subarray, the feed of each radiating element is at a distance of 5.84 mm from the neighboring elements along both the vertical and horizontal directions. The numerical simulation results of the 4 × 4 array, as illustrated in Figure 10, show a scanning capability of ±45° along the azimuth plane with a peak gain ranging from 21.48 dBi to 23.99 dBi. The array has been scaled up to 8 × 8 array elements and in this case, the main-lobe gain level is comprised between 27.81 dBi and 29.99 dBi.

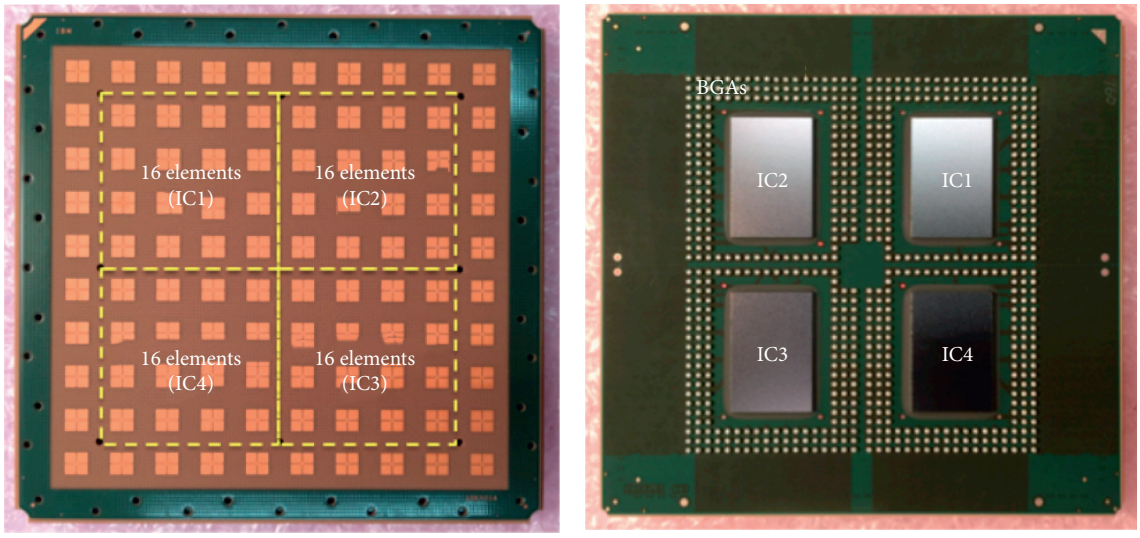

(a) (b)

Figure 8: Top view (a) and bottom view (b) of the antenna module as presented in [62] ©2019 IEEE.

Figure 9: Top view of the 8×8 DRA array proposed in [68].

In [71] a multimode horn antenna is used, instead, in a linear array configuration with sparse topology. The size of the individual radiating element is $2.0\lambda_0 \times 1.8\lambda_0$ at 28.5 GHz. This results in a peak gain of 11.5 dBi in combination with a 120° scanning range along the azimuth plane of the array. It is shown that the irregular sparse array can improve the system performance by decreasing the outage probability (referring to the probability that the Carrier to Noise Ratio is lower than 3 dB).

An alternative to horn and gap-waveguide technologies is represented by the use of open-ended waveguide arrays. The design presented in [72] is capable of scanning up to ±60° along both principal planes. A drawback of such technology, however, is the significantly more complicated manufacturing process. Furthermore, the integration of such radiating structures with printed circuits and components is not mature yet and requires additional research.

The design concepts presented up to now make use of phase shifters and variable gain amplifiers for each antenna element in order to realize beamforming. This requires the use of multiple power-hungry ICs. In [73, 74], an alternative solution is presented, where the use of a lens is investigated as a replacement to said ICs. The lens-based array antenna reported in [75] is optimized for 5G PtM wireless communications at mm-wave frequencies. The prototype is shown in Figure 11. The basic radiating structure is formed by a standard 4×4 patch antenna array with a size of 55 mm × 55 mm. The size of the individual patch antenna is 3.05 mm × 3.05 mm with an interelement spacing of λ_0 at the frequency of 30 GHz. The design relies on a hyperbolic dielectric lens made out of polyethylene, with a diameter of 155 mm. The concept is based on the independent control of the individual patch antennas so to focus the radiation beam in different directions according to a suitable beam-switching scheme. The working frequency band of the radiating structure is rather narrow and is limited to the range from 27.8 GHz to 28.4 GHz. The peak gain achieved with the considered design is about 12.12 dBi with an improvement of about 8 dBi as compared to the same radiating structure without integrated dielectric lens. The maximum scan range is about 15° but, as mentioned in [75], this can be further improved by using higher-order patch antenna array configurations.

Another alternative hybrid beamforming concept is represented by focal-plane arrays (FPAs) [76, 77]. Similar to the use of lens antennas, they provide a more limited scan range, which makes these concepts, in general, less suited for PtM applications.

5. High-Gain Array Antenna-Based Concepts for PtP Communications

In this section, we provide an overview of available antenna array concepts and technologies for mm-wave PtP communications. For such applications, key design aspects are the antenna beamwidth and directivity. These need to be carefully optimized to prevent system performance failure due to unwanted misalignment. Most of the PtP radio links are in fact designed for LOS communications in outdoor scenarios where devices are exposed to weather and environmental factors which can cause degradation of the quality of service (QoS). Reflectors, lens or DRAs, FPAs, and

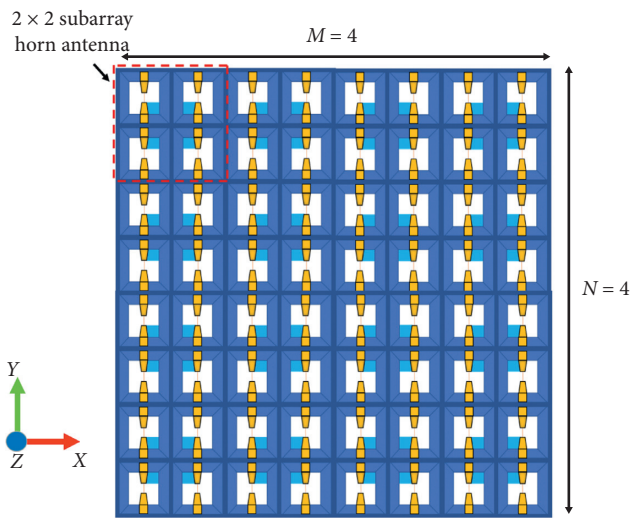

Figure 10: Top view of a 4 × 4 horn-based array antenna as presented in [70].

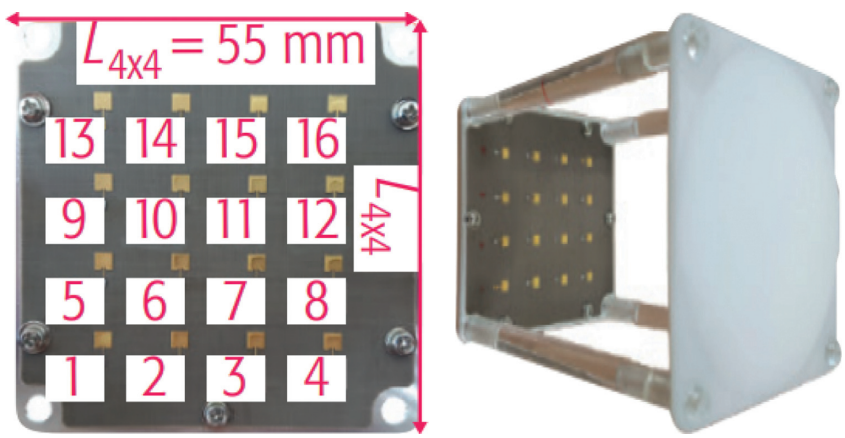

(a) (b)

Figure 11: Patch array (a) and lens antenna array prototype (b) proposed in [75] ©2018 IEEE.

reflectarrays are usually preferred to other classes of radiating structures for PtP communications by virtue of the high-gain characteristics they display. Alternative antenna technologies can, however, provide solutions in specific operative scenarios and are often employed [8]. The antenna concepts for mm-wave PtP communications reviewed in this study are illustrated in Table 3.

Thanks to the relevant high-gain characteristics, reflectarrays are becoming appealing for 5G applications. The solution proposed in [78] is a reflectarray based on microstrip patch antennas. The array operates in two frequency bands (around 27 GHz and 32 GHz) by integration of two sets of radiating elements which cover each band, separately. A horn antenna is used as a feeding structure. As mentioned by the authors, the considered reflectarray is not optimized in terms of bandwidth, and information in this respect is not made available. The design is optimized to support dual polarization. Such performance is achieved by properly rotating the radiating elements by 90°. The 2 × 2 patch assembly that constitutes the subarray cell has an overall size of 5.5 mm × 5.5 mm (which is $0.58\lambda_0$ at 32 GHz). The reflection phase is corrected for each frequency band/polarization by independently tuning the dimensions of each element. The total size of the reflectarray based on a 15 × 15 subarray configuration is approximately 82.5 mm × 82.5 mm. A peak gain of 27.5 dBi is observed at 32 GHz. Because of the relatively small dimensions, the design is affected by high spillover losses which result in an aperture efficiency of 29% at 27 GHz and 38% at 32 GHz.

The reflectarray proposed in [79] for operation in the frequency range from 30 GHz to 40 GHz is instead based on the use of DRA elements. The unit cell has a circular shape with four arms, and the relevant radius is tuned in a suitable way when moving from the center to the edge of the reflectarray so to synthesize the required reflection phase response. The unit cells embedded in the structure are 446, arranged in a circular array with a maximal radius of 60 mm. A horn antenna is used as a feeder. The choice of DRAs as

Table 3: State of the art of high-gain array-based antenna concepts for PtP mm-wave wireless communications.

Antenna technology	Bandwidth (GHz)	Peak gain (dBi)	Dimensions (mm^2)	SLL (dB)	Aperture efficiency (%)	Number of elements	Polarization
AiP patch [63]	57–64	10	14×14	−7.5	11	2×2	Single
Lens antenna [75]	27.8–28.4	25	100×100	−8	30	2×2	Single
Patch reflectarray [78]	NA	27.5	82.5×82.5	−12	38	15×15	Dual
DRA reflectarray [79]	30–40	24.8	$60 \times 60 \times \pi$	−10	26	446	Single
Double-ring reflectarray [80]	26–35	37.8	$177 \times 177 \times \pi$	−14	60	NA	Single
DRA [81]	29–34.3	16.29	NA	−10	NA	4×4	Circular
GDRA [83]	29.3–35.2	12	36.5×8	−10	38	1×8	Single
GDRA [84]	55–62	19.4	23×20	−14	38	8×8	Single
3D printed horn [85]	27.6–38.1	33.8	140×140	−15	86	16×16	Single
Vivaldi [86]	28–38	24.1	97.5×42	−7.7	32	4×4	Single
SIW horn [88]	25.25–32.6	17.2	70×2.8	−12	80	1×4	Single
SIW horn with lens [89]	26.7–27.3	15.65	112×2.5	−9.63	63	1×8	Single
SIW stacked patch [90]	25–33.7	20.3	100×90	−9	20	4×4	Circular
Slotted waveguide [91]	71–81	39.4	210×220	−18.9	24	512	Single
Gap waveguide [92]	57–66	33.3	80×80	−12	64	256	Single
Resonant cavity [93]	26–31.3	14.1	19×19	NA	65	2×2	Circular

basic radiating elements allows removing conductor losses and, in this way, attaining a measurably high peak gain of 23.9 dBi at 34 GHz and of 24.8 dBi at 35 GHz.

In [80], a reflectarray with very high-gain characteristics over a wide frequency range is presented. The design approach adopted for this purpose is based on a spatial dispersion compensation concept. The reflectarray is formed by a single-layer printed structure consisting of patch and double-ring (multiresonant) elements with properly selected dimensions, arranged according to a circular array scheme. The array has a maximal radius of 350 mm and is divided into two areas: the first area, closer to the center, is formed by double-ring elements, whereas the second area, towards the edge, is formed by patch elements. The frequency-phase response of each element can, in this way, compensate for the dispersion process caused by different propagation paths. The considered reflectarray is characterized by peak gain up to 37.8 dBi at 34 GHz, with a minimum level of 36 dBi across the entire operational frequency band from 26 GHz to 35 GHz.

As mentioned above, lenses are often employed for PtP wireless communications, thanks to their capability of drastically enhancing the antenna gain. The design presented in [75] demonstrates this once more. A conventional patch antenna is used as a basic radiating element with a peak gain of about 6 dBi. Thanks to the integration of a suitable cubic lens, the gain level is increased up to 12 dBi. The dimensions of the individual antenna, inclusive of lens, are $50\,\text{mm} \times 50\,\text{mm} \times 60\,\text{mm}$. The radiating element can be easily arranged in a linear or planar array configuration. Measurements of the 1×4 array and 2×2 array have shown a peak gain of approximately 25 dBi at 28 GHz.

In [81], a circularly polarized dielectric resonator antenna array for mm-wave frequencies is presented. In order to achieve circular polarization, X-shaped slots are etched off the ground plane so to excite the radiating elements while removing the need for more complex pin probes. In order to enhance the bandwidth of the array, a sequential feeding network is used, similarly to the design concept illustrated in [82]. The simulated impedance bandwidth extends from 24.1 GHz to 31.1 GHz, whereas the simulated axial ratio (AR) bandwidth at 3 dB level extends from 26.9 GHz to 33.7 GHz. The antenna structure realizes, at the working frequency of 30 GHz, a peak gain of 12.44 dBi when arranged in a 2×2 array scheme and of 16.29 dBi in a 4×4 configuration.

An attractive alternative solution to conventional dielectric resonator arrays for mm-wave applications is reported in [83]. Here, an artificial grid dielectric resonator antenna (GDRA) is optimized in such a way so as to deliver high gain in combination with wideband characteristics at mm-wave frequencies. The size of the individual GDRA is only $2.7\,\text{mm} \times 2.7\,\text{mm} \times 0.5\,\text{mm}$ (i.e., $0.29\lambda_0 \times 0.29\lambda_0 \times 0.05\lambda_0$ at 32.2 GHz). Each GDRA is bonded to the substrate and is excited through a slot whose length is chosen to be approximately $\lambda_{\text{eff}}/2$, with λ_{eff} denoting the effective wavelength. The slot is realized in a SIW channel in combination with a suitable transition in microstrip technology. The GDRA elements are arranged in 1×4 or 1×8 array configurations, as illustrated in Figure 12. The eight-element array shows an impedance bandwidth at 10 dB return-loss level of 5.3 GHz (i.e., from 29 GHz to 34.3 GHz) with an improvement of 2.65 GHz as compared to the four-element array. The peak realized gain of the eight-element array is 12.13 dBi against 10.2 dBi featured by the smaller configuration. An efficiency level above 85% across the relevant operational frequency band is reported for both arrays. The same design solution can be tailored for applications at 60 GHz as documented in [84]. Here, GDRAs have been characterized in 4×4 and 8×8 array configurations. The operational band is from 56.5 GHz to 63 GHz in the former case and from 55 GHz to 62 GHz in the latter case. Experimental measurements carried out on the 4×4 and 8×8 GDRA arrays have shown a peak gain of 15.2 dBi and 19.4 dBi, respectively. According to the authors, the

proposed solution offers a lower profile and much wider impedance bandwidth as compared to conventional DRAs.

A 3D printed horn antenna array is investigated in [85]. Using such radiating element, a 16×16 array including a full-corporate air-filled waveguide network is designed for operation in *Ka*-band. The overall footprint size of the considered array is approximately $14\,\text{cm} \times 14\,\text{cm}$. The maximum broadside gain is 33.8 dBi, whereas the impedance bandwidth at 10 dB return-loss level is from 28.2 GHz to 35.8 GHz. The radiation efficiency is reported to be about 85% at the center of the operating frequency band.

In [86], a 4×4 array of slot-coupled Vivaldi antennas (SCVAs) is presented. The structure is optimized for 5G wireless communications and is demonstrated to have a wide impedance bandwidth, from 25 GHz to 40 GHz, in combination with high-gain characteristics. As a matter of fact, the individual SCVA features a peak gain of 13 dBi. On the other hand, the 4×4 array (see Figure 13) shows a broadside gain of 22.3 dBi at 28 GHz and 24.1 dBi at 38 GHz.

SIW technology is often adopted to ease fabrication and integration of horn antennas operating at mm-wave frequencies [87–89]. A relevant example of that can be found in [88], where a 1×4 array of hollow SIW (HSIW) H-plane horn antennas are realized using conventional, inexpensive though lossy, FR4 laminates. Under such assumption, HSIW technology provides an effective means for avoiding/reducing dielectric losses. The size of the individual horn antenna element is $18\,\text{mm} \times 25\,\text{mm} \times 2.8\,\text{mm}$, while a long dielectric load is used to improve the impedance matching characteristics, as shown in Figure 14. It is claimed that the radiating structure features an efficiency of 66.5% over the working frequency band from 27.6 GHz to 38.1 GHz, in combination with a maximum realized gain of 17.2 dBi.

Different methods have been introduced in the literature to improve gain and impedance matching properties of SIW-based horn antennas. In [87], a perforated dielectric slab is used to properly load the horn, whereas in [89], the horn antenna gain is boosted using an elliptical dielectric lens.

In [90], a novel SIW-based feeding network is cooptimized with a coplanar waveguide (CPW) fed array in such a way so as to achieve a wide bandwidth in terms of AR for applications in *Ka*-band. The basic radiating elements used in the considered design are stacked microstrip antennas. The array is formed by 4×4 subarrays, with each subarray consisting of 4×4 stacked patches. The relevant driven patches are embedded in the middle layer as shown in Figure 15. The overall size of the array is $106\,\text{mm} \times 90\,\text{mm} \times 1.016\,\text{mm}$. The radiation pattern features strong grating lobes since the distance between adjacent driven patches is $1.35\lambda_0$. Measurements show a bandwidth at 2 dB AR level from 25.25 GHz to 32.6 GHz in combination with a peak gain of 20.32 dBi at 30.5 GHz.

For fixed beam applications, slotted waveguides represent a sounding solution thanks to their high-gain and high-efficiency characteristics. The array proposed in [91] is a 32×64 slot array antenna with unequal beamwidths in the relevant horizontal and vertical planes. Measurement results show a return loss above 14 dB in the entire frequency band from 71 GHz to 81 GHz and a peak gain level of 39.4 dBi. The design presented in [92] is, instead, a high-gain slotted antenna array based on gap-waveguide technology. The antenna elements are designed using groove ridge and inverted microstrip solutions. The array consists of 16×16 radiating slots which cover the frequency band from 57 GHz to 66 GHz, with a peak gain of about 33.3 dBi at the center of the band in combination with an SLL below −12 dB.

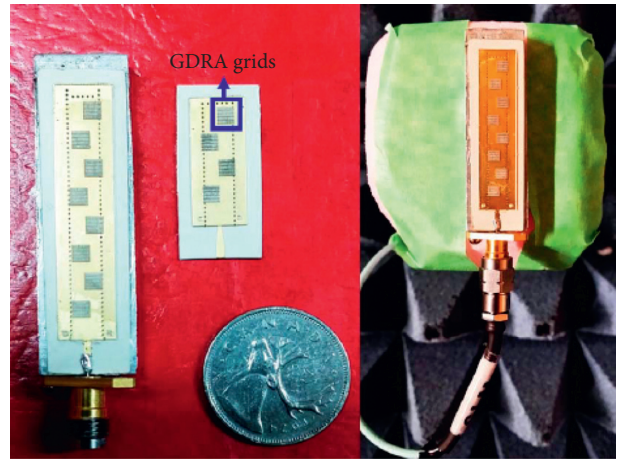

Figure 12: Illustration of the 1×8 (on the left) and 1×4 (on the right) GDRA arrays realized in [83] ©2019 IEEE.

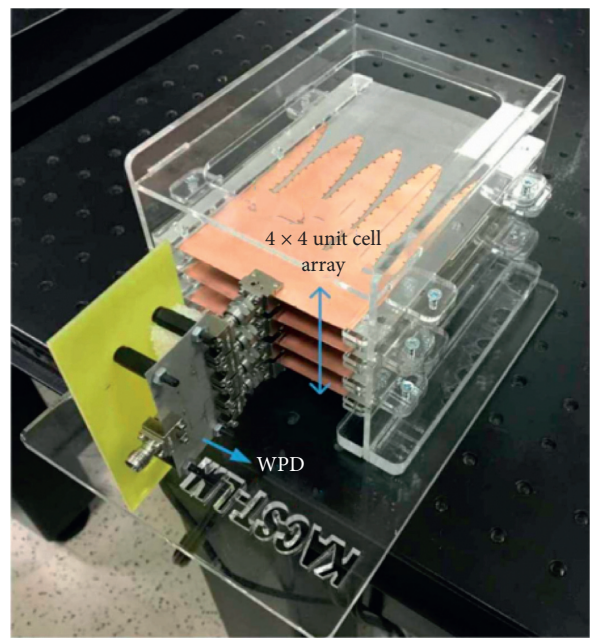

Figure 13: Box for placement of the four 1×4 antenna arrays as shown in [86].

As mentioned in Section 3, a high antenna gain can also be achieved by means of RCAs. As an example, the 2×2 array described in [93] relies on a Fabry-Perot resonant antenna structure. The individual array elements consist of a corner-cut patch with a diagonal slot, and each antenna is sequentially rotated by 90° in order to improve the relevant isolation. The considered array is characterized by a broad 3 dB AR bandwidth that ranges from

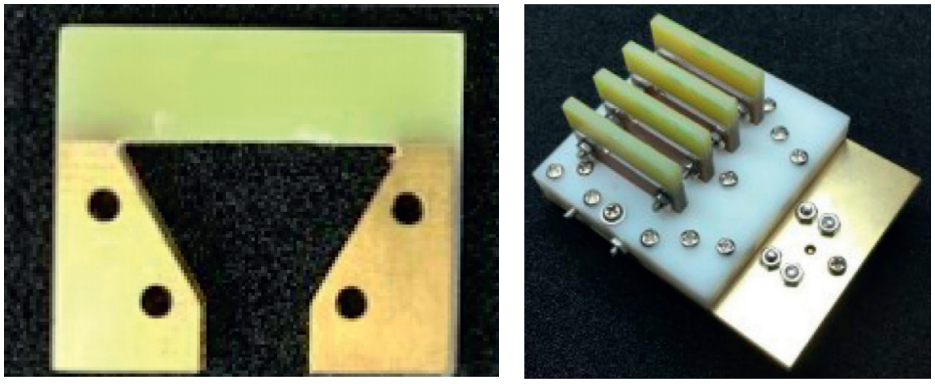

(a) (b)

Figure 14: HSIW Horn antenna element (a) and antenna array (b) proposed in [88] ©2019 IEEE.

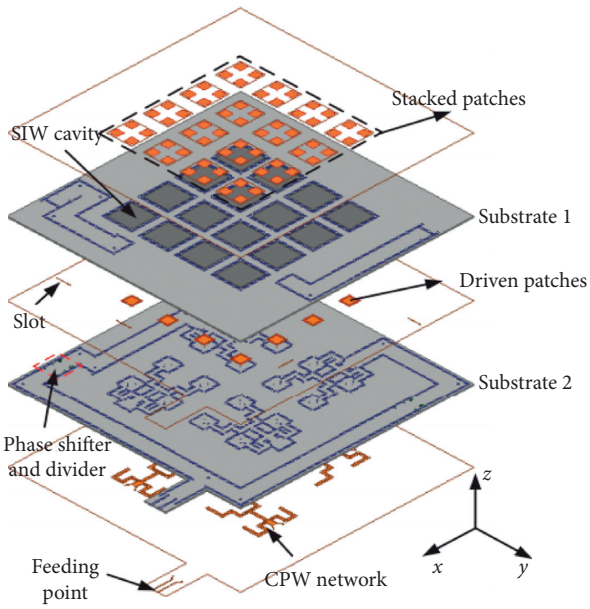

Figure 15: Layer configuration of the antenna array in [90] ©2018 IEEE.

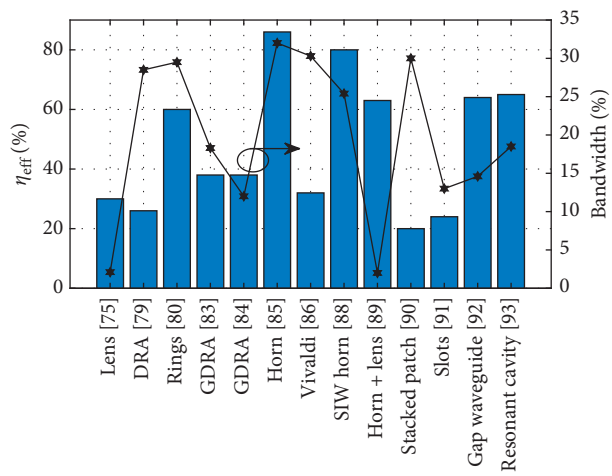

Figure 16: Aperture efficiency on the left axis and relative bandwidth on the right axis.

26 GHz to 31.3 GHz, in combination with a peak gain of 14.1 dBi at 28 GHz.

In Figure 16, the aperture efficiency, as computed by (4), and the relative bandwidth of each design concept for mm-wave PtP communications analyzed in this section are illustrated. One can notice how antenna arrays manufactured in waveguide/gap-waveguide technology tend to feature high aperture efficiency and wide bandwidth. As discussed in the previous sections, such benefit comes at the expense of significantly larger complexity and more expensive manufacturing process. Furthermore, this technology does not lend itself to the support of dual-polarization characteristics as it is now typically required for antenna systems for 5G communications.

Next to the overview in Table 3, it is important to stress that several research groups have developed alternative design approaches for gain enhancement of array antennas [94–99]. In [98], a straight slot is transversely introduced at the center of a patch. The slot acts as a secondary radiator which contributes to the enhancement of the antenna gain by about 1.7 dB without increasing the patch size. In [99], electromagnetic band-gap (EBG) structures have been employed to improve the gain of a 2×2 patch array antenna operating at 60 GHz. The merit of EBG structures is to suppress TM-mode surface waves [99], resulting in a gain enhancement of about 4 dB. On the other hand, the design solution illustrated in [97] enables a measurable gain increase thanks to the integration of a dielectric superstrate with circular holes. In combination with a 2×2 square patch antenna array, the use of the aforementioned superstrate structure results in a wider bandwidth of 15.35% and a nearly flat gain of 16 dBi in the frequency range from 26.5 GHz to 30.8 GHz.

6. Analysis and Discussion

The state-of-the-art overview provided in the previous sections gives a flavor of the wide variety of existing antenna concepts available in the literature; each of them characterized by different performance, benefits, and limitations. For mm-wave applications, ease of fabrication and a high

level of integration are key. It is not uncommon that a specific antenna technology is chosen mainly on the basis of manufacturing costs and integration constraints even if that results in largely suboptimal RF characteristics such as gain, efficiency, and bandwidth. The radiation properties of a given antenna element are also an important factor in the technology selection process. Broadside antennas are usually easier to integrate into array configuration, while end-fire radiating elements are most amenable for edge integration. To date, microstrip patch antennas are among the most used radiating elements for mm-wave arrays, although microstrip technology severely suffers from material losses and performance limitations at said frequencies.

One of the design challenges at mm-waves is associated with the correct knowledge of the material properties. At shorter wavelengths, it is certainly not straightforward to characterize dielectric materials with high accuracy. Furthermore, manufacturers typically provide, in their datasheets, detailed information regarding the complex permittivity of their own materials only up to 10 GHz. This is a definitive gap and possible drawback since even secondary materials such as soldermask may lead to unforeseen losses at the considered frequencies when neglected [100].

The main two types of losses at mm-wave frequencies are conductor and dielectric losses, with the former being typically more severe than the latter. The conductor losses quickly increase with frequency, due to the skin effect. The skin depth quantifies how close to the surface of a given conductor the electric current flows [101]. When the skin depth is approximately equal to the roughness of the conductor, a significant impact on the current flow is noticed. In fact, under said conditions, the surface roughness causes an increase of the parasitic inductance and, in turn, of the insertion loss [102]. Conductors with high melting temperature, low resistivity, low surface roughness levels, and good solderability are to be preferred for high-frequency circuit design [103]. The most common conductors with said characteristics are copper, gold, silver, aluminum, and palladium-silver alloys [103].

At mm-wave frequencies, the assumption of electrically thin dielectric substrates may be not valid any longer [104]. In the presence of thick substrates, surface wave modes are excited removing, in this way, power from the main beam radiation process; because of that, they can be regarded as a loss mechanism [12].

The choice of materials for mm-wave antenna array design is also related to another important challenge, that is, the thermal management. A growing number of research studies is being devoted to this problem [105], and highly efficient antennas are important to reduce the ohmic losses which contribute to the overall power dissipation budget. In this perspective, as seen in the previous sections, DRA and waveguide arrays showed good performance at mm-waves thanks to the high-efficiency and low-loss characteristics which they exhibit.

7. Conclusions

In this paper, an extensive overview of the state of the art of the most recent antenna array solutions for mm-wave communications has been given. In the first part of the manuscript, the development challenges at mm-wave frequencies have been discussed with particular focus on the antenna integration aspects associated with miniaturization, as well as the constraints relevant to the channel propagation characteristics and the need for cost and energy-efficient system design. In the subsequent sections, the recent developments in antenna technology for high-frequency applications have been surveyed, while highlighting the advantages and disadvantages of the most relevant designs available in the scientific and technical literature. In order to provide the reader with a rational classification, two different use cases have been identified: PtM and PtP wireless communications. The former requires the use of wide-scanning arrays, whereas the latter relies on high-gain directional antenna technologies.

For the first use case scenario, patch antenna arrays are widely used thanks to the radiation characteristics, which allow wide-angle scanning on both relevant planes. At the same time, DRA solutions are also emerging as promising candidates in this respect. For the second use case scenario, instead, reflectarrays, FPAs, and lens or dielectric resonators are preferred to other array technologies. In both cases, integration and manufacturability are key aspects in the selection of suitable antenna technology, while dedicated design approaches have to be adopted in such a way so as to ensure optimal scanning performance with stable gain, low-losses, and high-efficiency characteristics.

In the future, important opportunities will be offered by the advent of 6G communication systems as broader frequency bands will become available at even higher frequencies. At the same time, new challenges will have to be addressed, such as those associated with progressively higher propagation losses and tighter integration between electronic circuitry and antenna subsystems.

Conflicts of Interest

The authors declare that they have no conflicts of interest.

Acknowledgments

This work was carried out in the framework of the Top Consortium Knowledge and Innovation (TKI) Project "Arrays5G" running jointly at The Antenna Company and Eindhoven University of Technology.

References

[1] Z. Pi and F. Khan, "An introduction to millimeter-wave mobile broadband systems," *IEEE Communications Magazine*, vol. 49, no. 6, pp. 101–107, 2011.

[2] X. Wang, L. Kong, F. Kong et al., "Millimeter wave communication: a comprehensive survey," *IEEE Communications Surveys & Tutorials*, vol. 20, no. 3, pp. 1616–1653, 2018.

[3] A. Naqvi and S. Lim, "Review of recent phased arrays for millimeter-wave wireless communication," *Sensors*, vol. 18, no. 10, p. 3194, 2018.

[4] S. Dutta, M. Mezzavilla, R. Ford, M. Zhang, S. Rangan, and M. Zorzi, "MAC layer frame design for millimeter wave

cellular system," in *Proceedings of the European Conference on Networks and Communications (EuCNC)*, pp. 117–121, Athens, Greece, June 2016.

[5] C. H. Doan, S. Emami, D. A. Sobel, A. M. Niknejad, and R. W. Brodersen, "Design considerations for 60 GHz CMOS radios," *IEEE Communications Magazine*, vol. 42, no. 12, pp. 132–140, 2004.

[6] T. E. Bogale, X. Wang, and L. B. Le, "mmWave massive MIMO: a paradigm for 5G," in *mmWave Massive MIMO: A Paradigm for 5G*, S. Mumtaz, J. Rodriguez, and L. Dai, Eds., pp. 195–225, Acadamic Press, San Diego, CA, USA, 2017.

[7] Z. Qingling and J. Li, "Rain attenuation in millimeter wave ranges," in *Proceedings of the 7th International Symposium on Antennas, Propagation & EM Theory*, pp. 1–4, Guilin, China, October 2006.

[8] W. Hong, "Millimeter-wave antennas and arrays," in *Handbook of Antenna Technologies*, Z. Chen, D. Liu, H. Nakano, X. Qing, and T. Zwick, Eds., pp. 1787–1850, Springer, Singapore, 2016.

[9] A. C. F. Reniers, U. Johannsen, and A. B. Smolders, "Antenna-in-package measurements," in *Antenna-in-Package Technology and Applications*, pp. 115–145, IEEE, Piscataway, NJ, USA, 2020.

[10] P. Wang, Y. Li, L. Song, and B. Vucetic, "Multi-gigabit millimeter wave wireless communications for 5G: from fixed access to cellular networks," *IEEE Communications Magazine*, vol. 53, no. 1, pp. 168–178, 2015.

[11] T. S. Rappaport, Y. Xing, G. R. MacCartney, A. F. Molisch, E. Mellios, and J. Zhang, "Overview of millimeter wave communications for fifth-generation (5G) wireless networks-with a focus on propagation models," *IEEE Transactions on Antennas and Propagation*, vol. 65, no. 12, pp. 6213–6230, 2017.

[12] S. Ghosh and D. Sen, "An inclusive survey on array antenna design for millimeter-wave communications," *IEEE Access*, vol. 7, pp. 83137–83161, 2019.

[13] W. Hong, Z. H. Jiang, C. Yu et al., "Multibeam antenna technologies for 5G wireless communications," *IEEE Transactions on Antennas and Propagation*, vol. 65, no. 12, pp. 6231–6249, 2017.

[14] W. Hong, K.-H. Baek, and S. Ko, "Millimeter-wave 5G antennas for smartphones: overview and experimental demonstration," *IEEE Transactions on Antennas and Propagation*, vol. 65, no. 12, pp. 6250–6261, 2017.

[15] M. A. Matin, "Review on millimeter wave antennas—potential candidate for 5G enabled applications," *Advanced Electromagnetics*, vol. 5, no. 3, pp. 98–105, 016.

[16] K. Okada and J. Pang, "Millimeter-wave CMOS phased-array transceiver supporting dual-polarized MIMO for 5G NR," in *Proceedings of the IEEE Custom Integrated Circuits Conference (CICC)*, pp. 1–8, Boston, MA, USA, March 2020.

[17] D. Caratelli, M. C. Viganó, G. Toso, P. Angeletti, A. A. Shibelgut, and R. Cicchetti, "A hybrid deterministic/metaheuristic synthesis technique for non-uniformly spaced linear printed antenna arrays," *Progress In Electromagnetics Research*, vol. 142, pp. 107–121, 2013.

[18] T. S. Rappaport, S. Sun, and M. Shafi, "Investigation and comparison of 3GPP and NYUSIM channel models for 5G wireless communications," in *Proceedings of the IEEE 86th Vehicular Technology Conference (VTC-Fall)*, pp. 1–5, Toronto, ON, Canada, September 2017.

[19] T. S. Rappaport, G. R. MacCartney, M. K. Samimi, and S. Sun, "Wideband millimeter-wave propagation measurements and channel models for future wireless communication system design," *IEEE Transactions on Communications*, vol. 63, no. 9, pp. 3029–3056, 2015.

[20] D. Chizhik, J. Du, R. Feick, M. Rodriguez, G. Castro, and R. A. Valenzuela, "Path loss and directional gain measurements at 28 GHz for non-line-of-sight coverage of indoors with corridors," *IEEE Transactions on Antennas and Propagation*, vol. 68, no. 6, pp. 4820–4830, 2020.

[21] K. Bechta, J. Du, and M. Rybakowski, "Rework the radio link budget for 5G and beyond," *IEEE Access*, vol. 8, pp. 211585–211594, 2020.

[22] 3GPP Radio Access Network Working Group, *Study on Channel Model for Frequencies from 0.5 to 100 GHz (Release 15)*, 3GPP TR 38.901 V15.0.0, Sophia Antipolis, France.

[23] B. J. West, "Phased array antenna technology," in *The RF and Microwave Handbook*, M. Golio, Ed., pp. 1037–1057, CRC Press Taylor & Francis group, Inc., Boca Raton, FL, USA, 1st edition, 2001.

[24] Y. Li, S. Xiao, and J. Guo, "A review of wideband wide-angle scanning 2-D phased array and its applications in satellite communication," *Journal of Communications and Information Networks*, vol. 3, no. 1, pp. 21–30, 2018.

[25] H. Singh, H. L. Sneha, and R. M. Jha, "Mutual coupling in phased arrays: a review," *International Journal of Antennas and Propagation*, vol. 2013, Article ID 348123, 23 pages, 2013.

[26] R. Hill, "A practical guide to the design of microstrip antenna arrays," *Microwave Journal*, vol. 44, 2001.

[27] D. Caratelli, G. Toso, O. V. Stukach, and N. V. Panokin, "Deterministic constrained synthesis technique for conformal aperiodic linear antenna arrays-Part I: theory," *IEEE Transactions on Antennas and Propagation*, vol. 67, no. 9, pp. 5951–5961, 2019.

[28] D. Caratelli, G. Toso, O. V. Stukach, and N. V. Panokin, "Deterministic constrained synthesis technique for conformal aperiodic linear antenna arrays-part II: applications," *IEEE Transactions on Antennas and Propagation*, vol. 67, no. 9, pp. 5962–5973, 2019.

[29] P. J. Gibson, "The Vivaldi aerial," in *Proceedings of the 9th European Microwave Conference*, pp. 101–105, Bringhton, UK, September 1979.

[30] S. Zhu, H. Liu, Z. Chen, and P. Wen, "A compact gain-enhanced Vivaldi antenna array with suppressed mutual coupling for 5G mmWave application," *IEEE Antennas and Wireless Propagation Letters*, vol. 17, no. 5, pp. 776–779, 2018.

[31] P. Kumar, Z. Akhter, A. K. Jha, and M. J. Akhtar, "Directivity enhancement of double slot Vivaldi antenna using anisotropic zero-index metamaterials," in *Proceedings of the IEEE International Symposium on Antennas and Propagation & USNC/URSI National Radio Science Meeting*, pp. 2061-2062, Vancouver, BC, Canada, July 2015.

[32] A. Loutridis, S. Kazıcı, O. V. Stukach, A. B. Mirmanov, and D. Caratelli, "A novel class of super-elliptical Vivaldi antennas for ultra-wideband Applications," in *Advanced Radio Frequency Antennas for Modern Communication and Medical Systems*Albert Sabban, IntechOpen, London, UK, 2020.

[33] M. Moosazadeh and S. Kharkovsky, "A compact high-gain and front-to-back ratio elliptically tapered antipodal Vivaldi antenna with trapezoid-shaped dielectric lens," *IEEE Antennas and Wireless Propagation Letters*, vol. 15, pp. 552–555, 2016.

[34] P. Bia, D. Caratelli, L. Mescia, and J. Gielis, "Electromagnetic characterization of supershaped lens antennas for high-frequency applications," in *Proceedings of the European*

Radar Conference, pp. 367–370, Nuremberg, Germany, October 2013.

[35] L. Mescia, P. Bia, D. Caratelli, M. A. Chiapperino, O. Stukach, and J. Gielis, "Electromagnetic mathematical modeling of 3D supershaped dielectric lens antennas," *Mathematical Problems in Engineering*, vol. 2016, Article ID 8130160, 10 pages, 2016.

[36] H.-X. Xu, G.-M. Wang, Z. Tao, and T. J. Cui, "High-directivity emissions with flexible beam numbers and beam directions using gradient-refractive-index fractal metamaterial," *Scientific Reports*, vol. 4, no. 1, 2014.

[37] I. T. Nassar and T. M. Weller, "A novel method for improving antipodal Vivaldi antenna performance," *IEEE Transactions on Antennas and Propagation*, vol. 63, no. 7, pp. 3321–3324, 2015.

[38] R. Schulpen, U. Johannsen, S. C. Pires, and A. B. Smolders, "Design of a phased-array antenna for 5G base station applications in the 3.4–3.8 GHz band," in *Proceedings of the 12th European Conference on Antennas and Propagation (EuCAP)*, pp. 1–5, London, UK, April 2018.

[39] S. Keyrouz and D. Caratelli, "Dielectric resonator antennas: basic concepts, design guidelines, and recent developments at millimeter-wave frequencies," *International Journal of Antennas and Propagation*, vol. 2016, Article ID 6075680, 20 pages, 2016.

[40] M. Simeoni, R. Cicchetti, A. Yarovoy, and D. Caratelli, "Supershaped dielectric resonator antennas," in *Proceedings of the IEEE 2009 IEEE Antennas and Propagation Society International Symposium AP-S/URSI*, Charleston, SC, USA, June 2009.

[41] M. Simeoni, R. Cicchetti, A. Yarovoy, and D. Caratelli, "Circularly polarized supershaped dielectric resonator antennas for indoor ultra wide band applications," in *Proceedings of the 2010 IEEE Antennas and Propagation Society IEEE AP-S/URSI International Symposium*, Toronto, ON, Canada, July 2010.

[42] E. Baldazzi, A. Al-Rawi, R. Cicchetti et al., "A high-gain dielectric resonator antenna with plastic-based conical horn for millimeter-wave applications," *IEEE Antennas and Wireless Propagation Letters*, vol. 19, no. 6, p. 949, 2020.

[43] A. Petosa and A. Ittipiboon, "Dielectric resonator antennas: a historical review and the current state of the art," *IEEE Antennas and Propagation Magazine*, vol. 52, no. 5, pp. 91–116, 2010.

[44] Y. J. Cheng, K. Wu, and W. Hong, "Power handling capability of substrate integrated waveguide interconnects and related transmission line systems," *IEEE Transactions on Advanced Packaging*, vol. 31, no. 4, pp. 900–909, 2008.

[45] Y. J. Cheng, *Substrate Integrated Antennas and Arrays*, pp. 1–52, CRC Press, Boca Raton, FL, USA, 2015.

[46] T. Djerafi, A. Doghri, and K. Wu, "Substrate integrated waveguide antennas," in *Handbook of Antenna Technologies*, Z. Chen, Ed., pp. 1585–1655, Springer, Singapore, 2015.

[47] E. Rajo-Iglesias, M. Ferrando-Rocher, and A. U. Zaman, "Gap waveguide technology for millimeter-wave antenna systems," *IEEE Communications Magazine*, vol. 56, no. 7, pp. 14–20, 2018.

[48] A. U. Zaman and P. S. Kildal, "Gap waveguides," in *Handbook of Antenna Technologies*, Z. Chen, D. Liu, H. Nakano, X. Qing, and T. Zwick, Eds., pp. 3273–3347, Springer, Singapore, 2016.

[49] A. Goudarzi, M. M. Honari, and R. Mirzavand, "Resonant cavity antennas for 5G communication systems: a review," *Electronics*, vol. 9, no. 7, p. 1080, 2020.

[50] T. S. Bird, "Reflector Antennas," in *Handbook of Antenna Technologies*, Z. Chen, D. Liu, H. Nakano, X. Qing, and T. Zwick, Eds., pp. 853–922, Springer, Singapore, 2016.

[51] K. Kibaroglu, M. Sayginer, T. Phelps, and G. M. Rebeiz, "A 64-element 28-GHz phased-array transceiver with 52-dBm EIRP and 8-12-Gb/s 5G link at 300 meters without any calibration," *IEEE Transactions on Microwave Theory and Techniques*, vol. 66, no. 12, pp. 5796–5811, 2018.

[52] K. Klionovski, M. S. Sharawi, and A. Shamim, "A dual-polarization-switched beam patch antenna array for millimeter-wave applications," *IEEE Transactions on Antennas and Propagation*, vol. 67, no. 5, pp. 3510–3515, 2019.

[53] K. F. Lee and J. S. Dahele, "Characteristics of microstrip patch antennas and some methods of improving frequency agility and bandwidth," in *Handbook of Microstrip Antennas*, J. R. James and P. S. Hall, Eds., pp. 111–217, Peter Peregrinus Ltd., London, UK, 1989.

[54] H. Moody, "The systematic design of the butler matrix," *IEEE Transactions on Antennas and Propagation*, vol. 12, no. 6, pp. 786–788, 1964.

[55] K. Xiang and F. Chen, "4 × 4 broadband butler matrix and its application in antenna arrays," in *Proceedings of the IEEE International Symposium on Antennas and Propagation and USNC-URSI Radio Science Meeting*, pp. 675-676, Atlanta, GA, USA, December 2019.

[56] J. Pang, R. Wu, Y. Wang et al., "A 28-GHz CMOS phased-array transceiver based on LO phase-shifting architecture with gain invariant phase tuning for 5G new radio," *IEEE Journal of Solid-State Circuits*, vol. 54, no. 5, pp. 1228–1242, 2019.

[57] T. Sowlati, S. Sarkar, B. G. Perumana et al., "A 60-GHz 144-element phased-array transceiver for backhaul application," *IEEE Journal of Solid-State Circuits*, vol. 53, no. 12, pp. 3640–3659, 2018.

[58] Y. Développement, "5G's impact on RF front-end module and connectivity for cell phones 2019," 2021, http://www.yole.fr/yole–reports.aspx.

[59] J. D. Dunworth, A. Homayoun, B.-H. Ku et al., "A 28 GHz bulk-CMOS dual-polarization phased-array transceiver with 24 channels for 5G user and base station equipment," in *Proceedings of the IEEE International Solid-State Circuits Conference (ISSCC)*, pp. 70–72, San Francisco, CA, USA, March 2018.

[60] W. Qualcomm, "Wireless technology & innovation—mobile technology—qualcomm," 2021, https://www.qualcomm.com/.

[61] H. Kim, B.-S. Park, S.-S. Song et al., "A 28 GHz CMOS direct conversion transceiver with packaged antenna arrays for 5G cellular system," in *Proceedings of the IEEE Radio Frequency Integrated Circuits Symposium (RFIC)*, pp. 69–72, Honolulu, HI, USA, June 2017.

[62] X. Gu, D. Liu, C. Baks et al., "Development, implementation, and characterization of a 64-element dual-polarized phased-array antenna module for 28-GHz high-speed data communications," *IEEE Transactions on Microwave Theory and Techniques*, vol. 67, no. 7, pp. 2975–2984, 2019.

[63] I. Nasr, R. Jungmaier, A. Baheti et al., "A highly integrated 60 GHz 6-channel transceiver with antenna in package for smart sensing and short-range communications," *IEEE Journal of Solid-State Circuits*, vol. 51, no. 9, pp. 2066–2076, 2016.

[64] Y. Zhang, "Antenna-in-package technology: its early development (historical corner)," *IEEE Antennas and Propagation Magazine*, vol. 61, no. 3, pp. 111–118, 2019.

[65] S. Shahramian, M. J. Holyoak, A. Singh, and Y. Baeyens, "A fully integrated 384-element, 16-tile, W -band phased array with self-alignment and self-test," *IEEE Journal of Solid-State Circuits*, vol. 54, no. 9, pp. 2419–2434, 2019.

[66] N. Ojaroudiparchin, M. Shen, and G. F. Pedersen, "Design of Vivaldi antenna array with end-fire beam steering function for 5G mobile terminals," in *Proceedings of the 23rd Telecommunications Forum Telfor (TELFOR)*, pp. 587–590, Belgrade, Serbia, November 2015.

[67] S. Long, M. McAllister, and L. Liang Shen, "The resonant cylindrical dielectric cavity antenna," *IEEE Transactions on Antennas and Propagation*, vol. 31, no. 3, pp. 406–412, 1983.

[68] D. Caratelli, A. Al-Rawi, J. Song, and D. Favreau, "Dielectric resonator antenna arrays for 5G wireless communications," *Microwave Journal*, vol. 63, no. 2, pp. 36–46, 2020.

[69] C. Bencivenni, M. Gustafsson, A. Haddadi, A. U. Zaman, and T. Emanuelsson, "5G mmWave beam steering antenna development and testing," in *Proceedings of the 13th European Conference on Antennas and Propagation (EuCAP)*, pp. 1–4, Krakow, Poland, June 2019.

[70] Y. C. Mark TAN, N. G. Guan Hong, and Y. S. Roger TAY, "A 2-by-2 sub-array for scalable 28 GHz mm-wave phased array horn antenna in 5G network," in *Proceedings of the 13th European Conference on Antennas and Propagation (EuCAP)*, pp. 1–5, Krakow, Poland, June 2019.

[71] R. Budé, U. Johannsen, T. Bressner, A. B. Smolders, and M. V. Ivashina, "Sparse array topologies for 5G mmWave base-stations: a system-level study," 2020.

[72] A. B. Smolders, "Design and construction of a broadband wide-scan angle phased-array antenna with 4096 radiating elements," in *Proceedings of the International Symposium on Phased Array Systems and Technology*, pp. 87–92, Boston, MA, USA, October 1996.

[73] J. Ala-Laurinaho, J. Aurinsalo, A. Karttunen et al., "2-D beam-steerable integrated lens antenna system for 5G E -band access and backhaul," *IEEE Transactions on Microwave Theory and Techniques*, vol. 64, no. 7, pp. 2244–2255, 2016.

[74] Y. Zeng and R. Zhang, "Millimeter wave MIMO with lens antenna array: a new path division multiplexing paradigm," *IEEE Transactions on Communications*, vol. 64, no. 4, pp. 1557–1571, 2016.

[75] Y. J. Cho, G.-Y. Suk, B. Kim, D. K. Kim, and C.-B. Chae, "RF lens-embedded antenna array for mmWave MIMO: design and performance," *IEEE Communications Magazine*, vol. 56, no. 7, pp. 42–48, 2018.

[76] A. Dubok, A. Al-Rawi, N. Tessema et al., "Double-reflector configuration for optimal exposure of wideband focal-plane arrays with optical beamforming," *IEEE Transactions on Antennas and Propagation*, vol. 65, no. 8, pp. 4316–4321, 2017.

[77] A. B. Smolders, A. Dubok, N. M. Tessema et al., "Building 5G millimeter-wave wireless infrastructure: wide-scan focal-plane arrays with broadband optical beamforming," *IEEE Antennas and Propagation Magazine*, vol. 61, no. 2, pp. 53–62, 2019.

[78] S. Costanzo, F. Venneri, A. Borgia, and G. D. Massa, "Dual-band dual-linear polarization reflectarray for mmWaves/5G applications," *IEEE Access*, vol. 8, pp. 78183–78192, 2020.

[79] Y.-X. Sun and K. W. Leung, "Millimeter-wave substrate-based dielectric reflectarray," *IEEE Antennas and Wireless Propagation Letters*, vol. 17, no. 12, pp. 2329–2333, 2018.

[80] Y. Liu, Y. J. Cheng, X. Y. Lei, and P. F. Kou, "Millimeter-wave single-layer wideband high-gain reflectarray antenna with ability of spatial dispersion compensation," *IEEE Transactions on Antennas and Propagation*, vol. 66, no. 12, pp. 6862–6868, 2018.

[81] M. Akbari, S. Gupta, R. Movahedinia, S. Zarbakhsh, and A. R. Sebak, "Bandwidth enhancement of 4 × 4 subarrays circularly polarized rectangular dielectric resonator antenna by sequential feeding network," in *Proceedings of the 10th European Conference on Antennas and Propagation (EuCAP)*, pp. 1–4, Davos, Switzerland, April 2016.

[82] S.-L. S. Yang, R. Chair, A. A. Kishk, K.-F. Lee, and K.-M. Luk, "Study on sequential feeding networks for subarrays of circularly polarized elliptical dielectric resonator antenna," *IEEE Transactions on Antennas and Propagation*, vol. 55, no. 2, pp. 321–333, 2007.

[83] W. Mazhar, D. M. Klymyshyn, G. Wells, A. A. Qureshi, M. Jacobs, and S. Achenbach, "Low-profile Artificial grid dielectric resonator antenna arrays for mm-wave applications," *IEEE Transactions on Antennas and Propagation*, vol. 67, no. 7, pp. 4406–4417, 2019.

[84] W. Mazhar, D. Klymyshyn, G. Wells, A. Qureshi, and M. Jacobs, "60 GHz substrate integrated waveguide-fed monolithic grid dielectric resonator antenna arrays," *IEEE Antennas and Wireless Propagation Letters*, vol. 18, no. 6, pp. 1109–1113, 2019.

[85] Y. Li, "A *Ka*-band 3D printed horn antenna array," in *Proceedings of the International Conference on Microwave and Millimeter Wave Technology (ICMMT), Technology (ICMMT)*, pp. 1–3, Guangzhou, China, May 2019.

[86] W. T. Sethi, M. A. Ashraf, A. Ragheb, A. Alasaad, and S. A. Alshebeili, "Demonstration of millimeter wave 5G setup employing high-gain Vivaldi array," *International Journal of Antennas and Propagation*, vol. 2018, Article ID 3927153, 12 pages, 2018.

[87] Y. Cai, Z. Qian, Y. Zhang, J. Jin, and W. Cao, "Bandwidth enhancement of SIW horn antenna loaded with air-via perforated dielectric slab," *IEEE Antennas and Wireless Propagation Letters*, vol. 13, pp. 571–574, 2014.

[88] Z. Qi, X. Li, J. Xiao, and H. Zhu, "Dielectric-slab-loaded hollow substrate-integrated waveguide *H*-plane horn antenna array at *Ka*-band," *IEEE Antennas and Wireless Propagation Letters*, vol. 18, no. 9, pp. 1751–1755, 2019.

[89] H. Wang, D. Fang, B. Zhang, and W. Che, "Dielectric loaded substrate integrated waveguide (SIW) H-plane horn antennas," *IEEE Transactions on Antennas and Propagation*, vol. 58, no. 3, pp. 640–647, 2010.

[90] H. Xu, J. Zhou, K. Zhou, Q. Wu, Z. Yu, and W. Hong, "Planar wideband circularly polarized cavity-backed stacked patch antenna array for millimeter-wave applications," *IEEE Transactions on Antennas and Propagation*, vol. 66, no. 10, pp. 5170–5179, 2018.

[91] L. Qin, Y. Lu, Q. You, Y. Wang, J. Huang, and P. Gardner, "Millimeter-wave slotted waveguide array with unequal beamwidths and low sidelobe levels for vehicle radars and communications," *IEEE Transactions on Vehicular Technology*, vol. 67, no. 11, pp. 10574–10582, 2018.

[92] A. U. Zaman and P. Kildal, "Different gap waveguide slot array configurations for mmwave fixed beam antenna application," in *Proceedings of the 10th European Conference on Antennas and Propagation (EuCAP)*, pp. 1–4, Davos, Switzerland, 2016.

[93] N. Hussain, M.-J. Jeong, J. Park, and N. Kim, "A broadband circularly polarized fabry-perot resonant antenna using A single-layered PRS for 5G MIMO applications," *IEEE Access*, vol. 7, pp. 42897–42907, 2019.

[94] B. Thors, A. Furuskär, D. Colombi, and C. Törnevik, "Time-averaged realistic maximum power levels for the assessment of radio frequency exposure for 5G radio base stations using massive MIMO," *IEEE Access*, vol. 5, pp. 19711–19719, 2017.

[95] N. Ojaroudiparchin, M. Shen, and G. F. Pedersen, "8 × 8 planar phased array antenna with high efficiency and insensitivity properties for 5G mobile base stations," in *Proceedings of the 10th European Conference on Antennas and Propagation (EuCAP)*, pp. 1–5, Davos, Switzerland, April 2016.

[96] A. Dadgarpour, A. A. Kishk, and T. A. Denidni, "Gain enhancement of planar antenna enabled by array of split-ring resonators," *IEEE Transactions on Antennas and Propagation*, vol. 64, no. 8, pp. 3682–3687, 2016.

[97] M. Asaadi and A. Sebak, "Gain and bandwidth enhancement of 2 × 2 square dense dielectric patch antenna array using a holey superstrate," *IEEE Antennas and Wireless Propagation Letters*, vol. 16, pp. 1808–1811, 2017.

[98] X. Zhang and L. Zhu, "Gain-enhanced patch antenna without enlarged size via loading of slot and shorting pins," *IEEE Transactions on Antennas and Propagation*, vol. 65, no. 11, pp. 5702–5709, 2017.

[99] W. E. McKinzie, D. M. Nair, B. A. Thrasher, M. A. Smith, E. D. Hughes, and J. M. Parisi, "60-GHz LTCC patch antenna array with an integrated EBG structure for gain enhancement," *IEEE Antennas and Wireless Propagation Letters*, vol. 15, pp. 1522–1525, 2016.

[100] J. Coonrod, "Choosing circuit materials for millimeter wave applications," *High Frequency Electronics*, vol. 12, pp. 22–30, 2013.

[101] T. Jariyanorawiss and C. Thumkanon, "Optimization of coating material selection using the skin depth approximation," in *Proceedings of the 2018 IEEE International WIE Conference on Electrical and Computer Engineering (WIECON-ECE)*, pp. 114–117, Chonburi, Thailand, October 2018.

[102] A. F. Horn, J. W. Reynolds, and J. C. Rautio, "Conductor profile effects on the propagation constant of microstrip transmission lines," in *Proceedings of the IEEE MTT-S International Microwave Symposium*, pp. 868–871, Anaheim, CA, USA, June 2010.

[103] J. R. Baker-Jarvis, M. D. Janezic, B. F. Riddle, C. L. Holloway, N. G. Paulter Jr., and J. Blendell, *Dielectric and Conductor-Loss Characterization and Measurements on Electronic Packaging Materials*, NIST National Institute Standards Technology, Gaithersburg, MD, USA, 2001.

[104] D. Pozar, "Considerations for millimeter wave printed antennas," *IEEE Transactions on Antennas and Propagation*, vol. 31, no. 5, pp. 740–747, 1983.

[105] Y. Aslan, J. Puskely, J. H. J. Janssen, M. Geurts, A. Roederer, and A. Yarovoy, "Thermal-aware synthesis of 5G base station antenna arrays: an overview and a sparsity-based approach," *IEEE Access*, vol. 6, pp. 58868–58882, 2018.

Hindawi
International Journal of Antennas and Propagation
Volume 2021, Article ID 8874385, 11 pages
https://doi.org/10.1155/2021/8874385

Research Article

Optimization of Modified Yagi-Uda Nanoantenna Arrays Using Adaptive Fuzzy GAPSO

Pitther N. Santos, Victor Dmitriev, and Karlo Q. da Costa

Department of Electrical Engineering, Federal University of Para, Belém-PA, Brazil

Correspondence should be addressed to Pitther N. Santos; pitther.negrao@yahoo.com.br

Received 18 September 2020; Revised 23 December 2020; Accepted 21 January 2021; Published 17 February 2021

Academic Editor: Diego Caratelli

This paper presents an optimization of the radiation and absorption characteristics of modified Yagi-Uda (YU) nanoantenna arrays. Four geometries of antennas are considered: conventional YU fed by voltage source and transmission line, and YU with a loop element fed by voltage source and transmission line. The numerical electromagnetic simulations of these nanoantennas were made by the method of moments (MoM). The optimization method used is the adaptive fuzzy GAPSO, which consists of hybridization between genetic algorithm (GA) and particle swarm optimization (PSO), with a fuzzy system employed to adapt the inertial weight ω and the acceleration coefficients C_1 and C_2 of PSO. The optimized results show that the modified YU nanoantennas present better characteristics of gain, directivity, and radiation efficiency than the conventional YU antenna.

1. Introduction

Optical nanoantennas have received great interest in recent years in the scientific community due to its ability to increase and confine optical fields beyond the diffraction limit of light. With this characteristic, it is possible application in the areas of nanophotonics, biology, chemistry, computer science, optical microscopy, photovoltaic, and others [1–3].

Array of optical antennas, for example, Yagi-Uda (YU) nanoantennas, possess better unidirectional radiation characteristics than single element antennas [4]. Also, these antennas can provide higher coupling between optical fields and nanoplasmonic waveguides [5, 6]. In [7], Mironov et al. fabricated an array of 80 YU nanoantennas on the coating of an optical fiber. This antenna was fed by a Gaussian beam and its radiation was optimized at $\lambda = 1060$ nm, where the authors obtained an increase in directivity around 5 dB. Already in [8], through 3D numerical calculations, the interaction of a single emitter with a YU array is presented. It was proven that the electromagnetic fields from the emitter are improved due the array. Also, a tunable YU nanoantenna with semiconductors material loaded in the gap of the dipole element in the array is shown in [9]. In [10], Da Costa et al. used YU nanoantennas to improve the transmission efficiency of a wireless optical nanolink. In all these works, a little attention has been given to the optimization process of the nanoantennas, i.e., no special optimization technique was used in the antenna design.

This paper proposes the optimization of radiation and absorption of four models of YU nanoantennas. The first model is the classical geometry composed by five cylindrical elements made of gold: a reflector, a dipole, and three directors, where the dipole is fed by an equivalent voltage source. The second model has the same geometry as the first, but the dipole is connected to an optical transmission line (OTL). The third model is a conventional YU combined with a rectangular loop placed above the feeding dipole. The fourth model has the same geometry of the third model, but with an OTL connected to the dipole. These nanoantennas were analyzed numerically by the Method of Moments (MoM) [11], where a MoM code was developed to simulate and optimize these antennas. There are some works about optimization of antennas array available in literature, where different optimization techniques have been used [12–16]. However, we prefer to use in present paper the fuzzy adaptive GAPSO method due their better efficiency [17].

This optimization technique is a hybrid method between genetic algorithm (GA) and particle swarm optimization (PSO), with a fuzzy system used to adapt some parameters of PSO.

The geometries of the proposed antennas were optimized to obtain optimal radiation efficiency and gain and directivity in the frequency range of 100–400 THz. The optimized results are presented and discussed. Some results are compared with simulations made by software based on finite element method [18] in order to compare and validate our results. The remainder of this work is organized as follows. Section 2 presents the geometries of the antennas and the theoretical MoM model considered, Section 3 explains the optimization technique used in this work, and Section 4 presents the numerical results and Section 5 the conclusions.

2. Theoretical Development

2.1. Geometries of the YU Nanoantennas. Figure 1(a) illustrates schematically the considered conventional YU nanoantenna, consisting of a nanodipole, three directors above of nanodipole, and one reflector below it. The entire structure of the model is located in free space. In this figure, a voltage source V_s, applied in the gap d, located in the center of the nanodipole is used to fed the nanoantenna. Figure 1(b) has the same geometry as the previous case, but an optical transmission line (OTL) is connected through the dipole. The only difference between a standard transmission line and an OTL is the physical properties of the conductors. The conductivity of metals is not infinite in optical frequencies, that is, the metal presents a complex permittivity variable with frequency. In other words, the metals not behave like perfect conductors, but rather as plasmonic material described by the Lorentz–Drude model for the complex permittivity. This OTL is perpendicular to the plane of the array and placed along the axis z. The third antenna shown in Figure 1(c) is a YU nanoantenna combined with a rectangular loop, which is fed by a voltage source V_s. The loop element is centered symmetrically with the dipole, in respect to the xy plane but is located above it by a distance d_w in direction of axis z, not shown in this figure. Figure 1(d) is the same YU nanoantenna as the previous case but connected to an OTL.

The geometric parameters of the nanoantennas are as follows: for the dipole, arm length (h), radius (a_h), and feed gap (d); for the reflector, length (h_r), radius (a_r), and distance to dipole (d_h); for the directors, length (h_n) radius (a_n), and distance to the previous director or dipole; in the case of the first director, d_n for $n = 1$, 2, and 3; for the OTL, length (L) and radius (a_l); and for the loop, length (h_e), width (w_e), height (d_w), and radius (a_e). The antenna arrays are in the xy plane with the dipole aligned along the y axis and the axis of the array aligned in the x direction as illustrated in Figure 1.

2.2. Method of Moments Model. The method of moments (MoM) is a technique used to solve the integral equation 1 D of the electric field, with linear approximation of the current longitudinal, rectangular pulse for test functions, and sinusoidal base functions [11]. The radiation problem of the nanoantennas in Figure 1 consists of an incident electric field $\overline{E}_i$ radiated from a voltage source in the center of the nanodipole or at the beginning of the OTL. This voltage generates an induced electric current I_{in} the conductors who in turn will radiate a field $\overline{E}_s$. The integral equation of electric field is obtained substituting the scattered field and the incident filed in the boundary conditions on the metal's surface [11]:

$$\left(\overline{E}_s + \overline{E}_i\right) \cdot \overline{a}_l = Z_s I, \tag{1}$$

where $\overline{a}_t$ is a unit vector tangent to the surface of the conductors, I is the current in a particular point on the nanoantenna's surface, and Z_s is the surface impedance of the conductors. The metallic nanoantenna is made of gold, where the model of its complex permittivity is the LorentzDrude model [19], given by

$$\varepsilon_{r1} = \varepsilon_\infty - \frac{\omega_{p1}^2}{\omega^2 - j\Gamma_D\omega} + \frac{\omega_{p2}^2}{\omega_0^2 - \omega^2 + j\gamma_L\omega}, \tag{2}$$

where the constants are $\omega_0 = 2\pi c/\lambda_0$, $\lambda_0 = 450\,\text{nm}$, and $c = 3 \times 10^8$ m/s, $\varepsilon_\infty = 8$, $\omega_{p1} = 13.8 \times 10^{15}\,\text{s}^{-1}$, $\omega_{p2} = 45 \times 10^{14}\,\text{s}^{-1}$, $\Gamma_D = 1.075 \times 10^{14}\,\text{s}^{-1}$, and $\gamma_D = 9 \times 10^{14}\,\text{s}^{-1}$. We can calculate the surface impedance by [20]

$$\begin{aligned} Z_s &= \frac{T, J_0\,(\text{Ta})}{2\pi a j\omega\varepsilon_1 J_1\,(\text{Ta})}, \\ T &= k_0\sqrt{\varepsilon_{r1}}, \\ k_0 &= \omega\sqrt{\mu_0\varepsilon_0}, \\ \varepsilon_1 &= \varepsilon_0\varepsilon_{r1}, \end{aligned} \tag{3}$$

where J_0 and J_1 are the Bessel functions of first type and zero order, respectively, j is the imaginary unit, ω the frequency of operation, and $T = k_0\sqrt{\varepsilon - (\beta/k_0)^2}$, β being the phase constant in the cylindrical waveguide, $k_0 = \omega\sqrt{\mu_0\varepsilon_0}$ the propagations constant in the air, μ_0 the magnetic permeability of air, and $\varepsilon_0$the electrical permittivity of air.

To transform the integral equation (1) in a linear system, we apply the conventional linear MoM with base functions sine and test functions rectangular pulse [11], where the following linear system is obtained:

$$V_m = Z_s I_m \Delta_m + \sum_{n=1}^{N} Z_{mn} I_n, \quad m = 1, 2, \ldots, N-1, \tag{4}$$

where V_m is the voltage in one generic segment m, the elements of Z_{mn} represent the mutual impedance between different points m and n on the antenna's surface, Δ_m is the length of each segment, and N is the total number of segments. The solution of the system (4) produces the current distribution I_m, and by this current, it is possible to calculate all the radiation and absorptions characteristics. All these parameters have been defined in [11]. The input impedance is calculated by

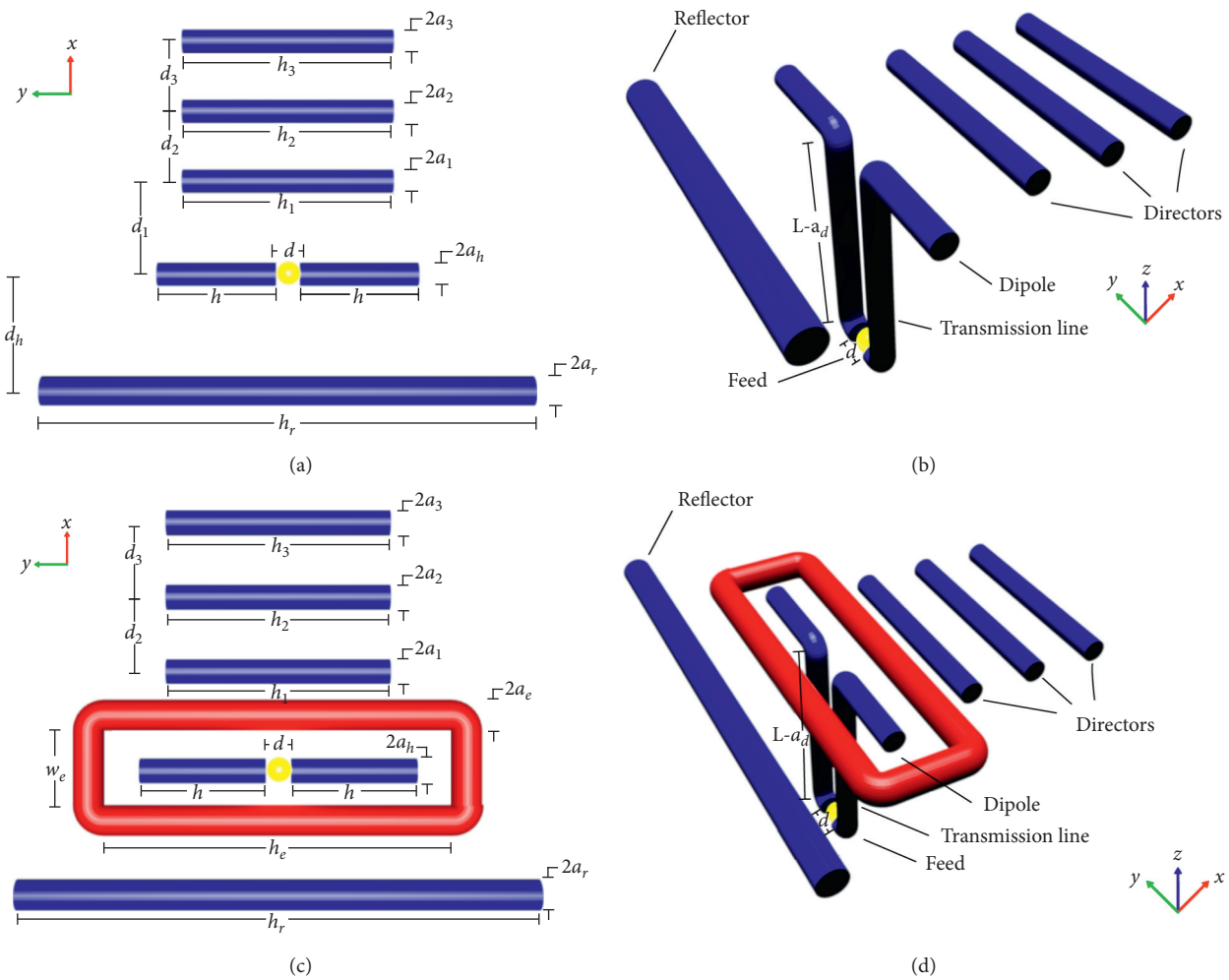

Figure 1: Geometries of the four YU nanoantennas models in study. (a) Conventional YU, (b) YU with OTL, (c) YU with loop, and (d) YU with loop and OTL.

$$Z_{in} = \frac{V_s}{I_f}, I_f = \frac{1}{\sinh \lambda d}\left[I_s \sinh\frac{\gamma d}{2} + I_{s+1}\sinh\frac{\gamma d}{2}\right], \quad (5)$$

where the localization of the voltage source is $m = s$. For $V_s = 1\ V$, the input impedance is $Z_{in} = 1/I_f = (R_r + R_L) + jX_{in} = R_{in} + jX_{in}$, where R_r, R_L, R_{in}, and X_{in} are the radiation resistance, loss resistance, input resistance, and input reactance, respectively. The total input power is calculated by $P_{in} = 0.5\,\mathrm{Re}\ (V_s I_f *) = 0.5\,(R_L + R_r)|I_f|^2 = 0.5\,R_{in}|I_f|^2 = P_r + P_L$, P_r is the radiated power and P_L the loss power dissipated at the antenna's surface which is calculated by [11]

$$P_L = 0.5\mathrm{Re}(Z_s)\sum_{n=1}^{N-1}|I_n|^2\Delta_n. \quad (6)$$

The radiated power can be obtained by $P_r = P_{in} - P_L$ and the resistances by $R_r = 2P_r/|I_f|^2$ and $R_L = 2P_L/|I_f|^2$. The radiation efficiency is defined by $e_r = P_r/P_{in} = P_r/(P_r + P_L) = R_r/(R_r + R_L) = R_r/R_{in}$.

3. Hybrid Method Adaptive Fuzzy GAPSO

3.1. Genetic Algorithm. The genetic algorithm (GA) is a metaheuristic inspired in the Darwinian natural selection, where the candidate solutions are represented by individuals, whose parameter vectors are coded in chromosomes and the parameters in each vector are coded in genes. The GA executes iteratively, the procedures of selection, crossover, and mutation in the population to generate individuals with optimized parameters. The selection process consists in selecting, among the population, the individuals who present the best evaluation, according to the objective function, while the remaining ones are discarded. The selection can be done by ranking [21], roulette [22], or tournament [23], and the selection criteria can be a threshold cost value or a determined percentage of population.

The following procedure of crossover consist in the generation of new individuals from the gene recombination among the present individuals called parents to obtain improved solutions by combining the favorable characteristics of the existing solutions. The main crossover methods

applied are as follows: simple crossover [24], arithmetic crossover [25], and uniform crossover [26].

The final procedure mutation changes, with an arbitrary probability, some parameters of the individuals, to generate and preserve diversity in the population and improve the exploration of the search space. The random mutation is the main employed mutation method and consists in randomly choosing individuals from the population and, from the chosen individuals, the genes that will be modified to random values [27].

3.2. Fuzzy Inference System (FIS). FIS are systems that apply fuzzy logic to make inferences from linguistic variables from a fuzzy associative matrix to output the system's response to the given inputs. Such systems are used to deal with parameters that present considerable uncertainty margin and/or have a complex mathematical representation [17]. The FIS are formed by: input variables, pertinence functions, fuzzy associative matrix, and output variables. The input variables are quantities that the FIS receive to generate inferences. The pertinence functions define a relation between a given input/output variable and its linguistic variables and determine how much the input variable is pertinent to each fuzzy set defined for these variables [28]. The fuzzy associative matrix defines the relations among the input and output variables, based on its linguistic variables. From the pertinence values of the input variables, the associative matrix infers the pertinence values of the output variables. The inference method employed in the FIS depends on its classification; the two most used classes of FIS are the Mamdani [28] and Tagaki-Sugeno [29] systems. The output variables receive the pertinence values inferred by the system and, by means of its pertinence functions, determine the real value that correspond to the received pertinence values and return them to the FIS output. From these real values, it is possible to control and adaptively adjust external systems connected to the FIS [28]. In the case of the adaptive fuzzy GAPSO, the FIS is a Mamdani system and is responsible to adjust the acceleration coefficients C_1 and C_2 which are the output variables of the FIS having as input variables: the percentage of complete iterations; and the normalized Euclidian distance defines as the ratio between the mean of the distances among the individual with best evaluation and the remaining individuals and the distance between the most distant individual and the best evaluated individual.

3.3. Particle Swarm Optimization (PSO). The PSO is metaheuristic inspired in the behavior of birds swarms searching for food [30]. The candidate solutions are represented by particles, in which its parameter vectors are coded in the position that each particle occupies in the search space. The particles $i = 1, \ldots, n$ are described by the current position $\overrightarrow{x_i}$ in the search space, the velocity $\overrightarrow{v_i}$, and the best individual position $\overrightarrow{g_i}$ [31]. PSO initially, determines the best individual positions $\overrightarrow{g_i}$, by evaluating the solution contained in each particle and the best global position $\overrightarrow{g_b}$ as the $\overrightarrow{g_i}$ with best evaluation. Then, the PSO updates the velocity $\overrightarrow{v_i}$ of each by [31]:

$$\overrightarrow{v_i} = W^* \overrightarrow{v_i} + \text{rand}^* C_1{}^* \overrightarrow{g_i} + \text{rand}^* C_2{}^* \overrightarrow{g_b}, \tag{7}$$

where W is the inertia coefficient of the particle and quantifies the resistance to changes in velocity presented by the particle; C_1 is the coefficient of individual acceleration, and quantifies the tendency of the particle to move towards its best individual solution; C_2 is the coefficient of social acceleration, and quantifies the tendency of the particle to direct to the best global solution; and rand is a random variable with uniform distribution in the range [0, 1] [30]. With the updated velocity, the final step of particle dislocation is done with [30, 31]

$$\overrightarrow{x_i} = \overrightarrow{x_i} + \overrightarrow{v_i}. \tag{8}$$

3.4. Adaptive Fuzzy GAPSO Method. To perform the optimization, the hybrid method adaptive fuzzy GAPSO was applied [17]. The adaptive fuzzy GAPSO is composed by three different methods that operate together to find an optimal solution for optimization problems. The methods are genetic algorithm (GA), fuzzy inference system (FIS), and particle swarm optimization (PSO).

Initially, the adaptive fuzzy GAPSO generates a population of N individuals, where each individual is represented by a vector of m values; the individuals represent the candidate solutions, and the vectors represent the parameters of each solution. Then, it is defined as the maximum number of iterations n, which will be the stopping criteria of the adaptive fuzzy GAPSO, the objective function (function that evaluates the individual's pertinence), the search space, and the optimization restrictions. After the initial procedures, the adaptive fuzzy GAPSO executes iteratively and in following sequence: the GA, the FIS, and the PSO, generating a new and improved population in each iteration, as is described in the flowchart in Figure 2 and in the following pseudocode.

This pseudocode explains the AGPSO used in this work, where an intermediary solution is obtained in each iteration. The stop condition verifies whether the total number of iterations has been achieved or if the best solution found by AGPSO remains constant in different iterations. If one of these conditions is met, the AGPSO stops and returns the best solution and the cost/relevance value. The population size and other general parameters used in the AGPSO method are defined according to the Table 1. The best solutions obtained by this method are the global maximum.

Pseudocode of the AGPSO algorithm

1: for $i \longleftarrow 1$ until Np do

2: Randomly initialize the position xi and the speed viof each particle;

3: Initialize the best position pi = xi;

4: Assess position xi;

5: Initialize pg, using the equation of the best global position;

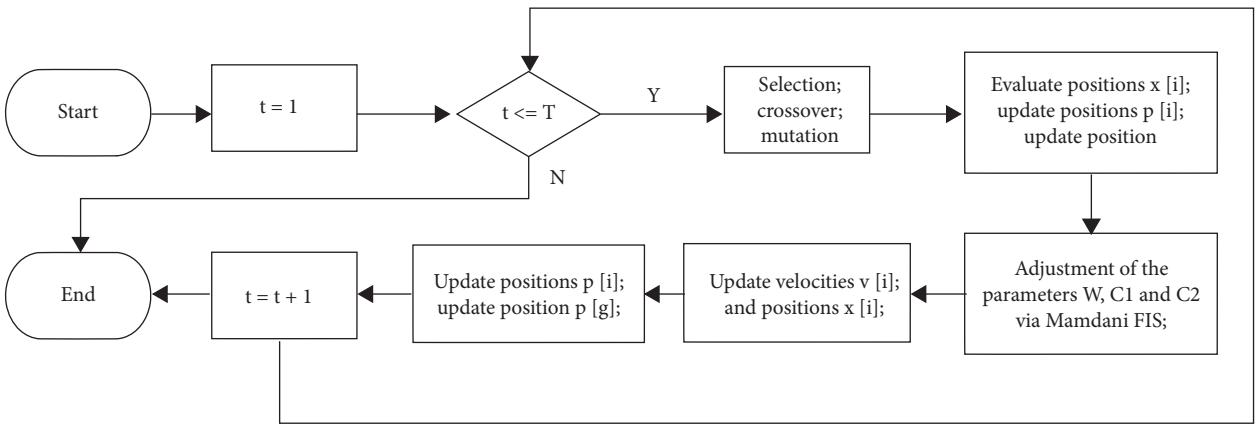

Figure 2: Adaptive GAPSO flowchart.

Table 1: General optimization parameters by the GAPSO method.

Populationsize	100 individuals
Numberof total iterations	100 iterations
Mutation rate	0.1 (10%)
Leniencyfee	0.5 (50%)
Inertia coefficient	1
Individual acceleration coefficient	1 (Initial)
Social acceleration coefficient	3 (Initial)

6: to end

7: for $t \longleftarrow 1$ until T do

8: for $i \longleftarrow 1$ until Np do

9: Select the particles that will be reproduced, with probability pc;

10: Apply the crossover;

11: Apply the mutation operator, with probability pm;

12: Insert new particles (children) into the population, replacing their parents;

13: Assess positions xi;

14: Update pi, using the equation of updating the position of each particle;

15: Update pg, using the equation of the best global position;

16: Update vi, using the equation of speed and best position, of each particle;

17: Update xi, using the speed update equation;

18: Evaluate positions xi;

19: Update pi, using the equation of updating the position of each particle;

20: Update pg, using the equation of the best global position;

21: end

22: end

4. Numerical Results

Based on the theory presented above, a MoM computational code was developed in the Matlab software to calculate the following results: input impedance, radiation diagram, radiation efficiency, gain, and directivity of the four nanoantennas and optimized via adaptive fuzzy GAPSO algorithm included in the MoM code. The objective function was defined as the maximum gain and radiation efficiency value of the YU antenna, given by

$$F(N_i) = \max(G(f, N_i).E(f, N_i)), \quad 100\,\text{THz} \le f \le 400\,\text{THz}, \tag{9}$$

where the N_i inputs of the objective function are the nanoantenna dimensions: length, radius, element distance, and dipole gap, which are contained in the search space, and are provided to the modeling algorithm.

4.1. Verification of the MoM Model. With the intention of testing and validating our MoM code developed, in this section, we present a comparison of the results obtained by FEM [18] and MoM codes. For this, we considered and simulated two antennas: a conventional YU array (Figure 1(a)) and an isolated dipole.

Figure 3 shows the input impedance calculated by MoM and FEM for both YU and isolated nanodipole for comparison, where this isolated nanodipole has the same dimensions of the nanodipole of the YU array. We observe a good agreement between these two methods and those reported in [11], which guarantees the good accuracy of our model. In both results, of isolated dipole and array, we note that the first two resonant frequencies are close each other; this shows that the directors and reflectors do not affect significantly the original resonant frequencies of the isolated dipole. The principal differences in these two cases is observed near the frequencies $F = 175$ and 260 THz (Figure 3(a)), which correspond physically to the dipolar resonances of the reflector and directors, respectively. These

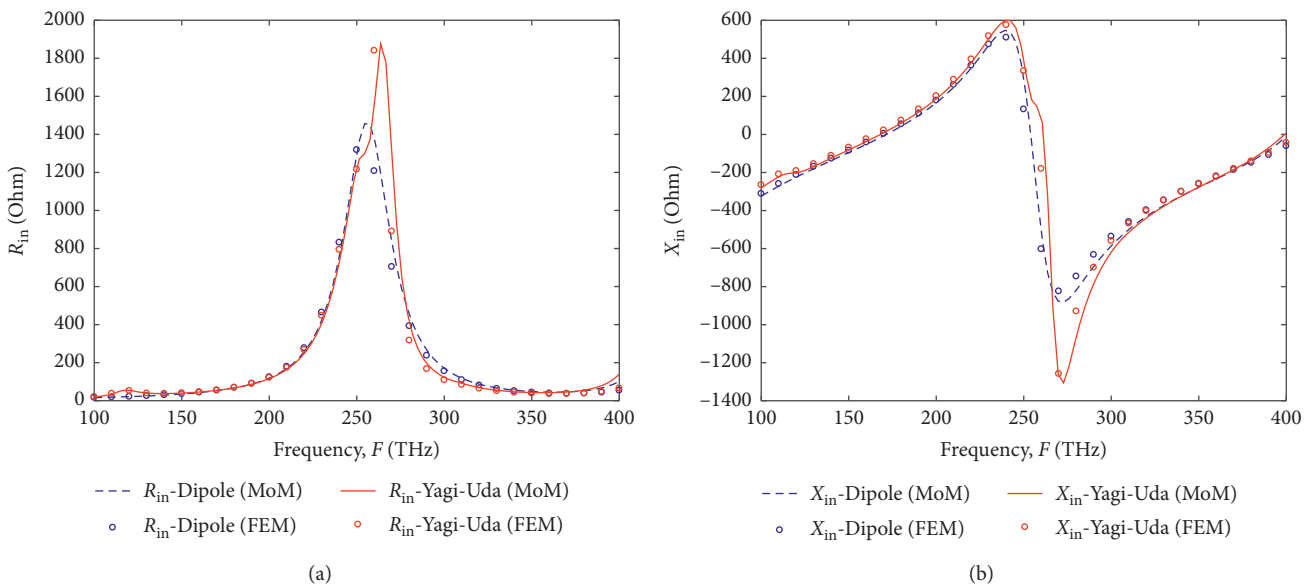

FIGURE 3: Input impedance of YU array and nanodipole: (a) R_{in} and (b) X_{in}. The dimensions of antennas are $h_r = 700$ nm, $h_t = 2$ (h) + (d) = 460 nm, $h_1 = h_2 = h_3 = 250$ nm, $d_h = d_1 = d_2 = d_3 = 100$ nm and $a_1 = a_2 = a_3 = a_h = a_r = 15$ nm.

resonances can be observed in the current distributions in these frequencies, which are not shown here.

4.2. Optimized Dimensions. To optimize the elements of YU nanoantennas, the search space of Table 2 was used. The search space is the range of the domain of the objective function in which the search for the minimum or maximum value of the function will be made. In this table are used typical values of dimensions considered in design of optical nanoantennas. The fuzzy adaptive AGPSO runs 100 iterations to find the best gain and efficiency of the nanoantennas.

Tables 3–6 show the optimized results obtained of the conventional YU (Figure 1(a)), YU with OTL (Figure 1(b)), YU with loop (Figure 1(c)), and YU with OTL and loop (Figure 1(d)), respectively. These tables present the optimized dimensions values of each element of the nanoantenna simulated by fuzzy adaptive AGPSO and the pertinence value equivalent to the maximum obtained gain of each nanoantenna.

In all the optimized antennas presented in these tables, the reflector and directors are smaller than the feeding element (dipole). We believe that this is due to the definition of the objective function being the gain instead of directivity. Smaller reflector size implies in smaller dissipated power in this element and consequently higher radiation efficiency. In this case, even that directivity been smaller, the higher efficiency compensates to obtain higher gain. In other words, smaller reflector produces higher efficiency, and the directors are responsible to increase the directivity.

4.3. Optimized Antenna Results. In this section, we present a comparison of the four nanoantennas optimized, in respect the following characteristics: input impedance, radiation efficiency, gain, and directivity, where their dimensions are presented in Tables 3–6.

Figure 4 presents the input impedances of the antennas, where Figure 4(a) shows the real component (R_{in}) and Figure 4(b) the imaginary component (X_{in}). In this figure, it is observed that the electromagnetic coupling between the YU nanoantenna with the new elements (OLT and Loop) modifies its input impedance. As the new elements are inserted in the YU, the larger is its input impedance in the frequency range of 200 THz to 260 THz. It is also observed that the nanoantenna YU and YU with OTL reached higher impedance value in the frequency range $F = 100$ to 150 THz (Figure 4(a)). The nanoantennas YU with loop and YU with loop and OTL reached higher values of R_{in} in the frequency range $F = 180$ to 280 THz (Figure 4(a)).

Figure 5 shows the radiation efficiency results e_r, in function of frequency. The adaptive fuzzy GAPSO optimization show to be effective when applied in nanoantennas design. In this work, good results are obtained: maximum efficiency of $e_r = 0.80$ for the YU with OTL and loop, $e_r = 0.73$ for the YU with loop, $e_r = 0.57$ for the YU with OTL, and $e_r = 0.53$ for the conventional YU. It is observed that in the insertion of new elements (OTL and loop) in the conventional YU, and after the optimization process, the resulted are improved considerably as can be seen in Figure 5.

Figure 6 shows the results of directivity (Figure 6(a)) and gain (Figure 6(b)) of the four optimized YU in the $+y$ direction. We observe that, in Figure 6(a), the maximum value of the directivity occurred in the case of YU with OTL and loop, where a peak of $D_0 = 46.5$ was obtained close to 259 THz. In the other hand, for the case of YU with loop, we have a peak of $D_o = 31.7$ near 274 THz, but at this frequency, the radiation efficiency is $e_r = 0.1$, which consequently reduces the gain because $G_0 = e_r D_0$. Table 7 shows the maximum directivity of the four nanoantennas and the frequency

Table 2: Search space for each dimension of the elements of the conventional YU nanoantenna.

Dipole			Transmission line (when present)			
Arm length (nm)		Radius (nm)	Length (nm)	Radius (nm)	Gap (nm)	
90–330		10–30	500–1000	10–30	10–30	
Reflector and directors			Rectangular loop (when present)			
Length (nm)	distance (nm)	Radius (nm)	Length (nm)	Distance (nm)	Radius (nm)	Height (nm)
90–330	90–330	10–30	400–1000	50–100	10–30	0–50

Table 3: Optimal dimensions found by fuzzy adaptive AGPSO method for conventional YU nanoantenna.

Dipole			1° director		
Arm length (nm)	Radius (nm)		Length (nm)	Distance (nm)	Radius (nm)
260	27		285	291	30
Reflector			2° director		
Length (nm)	Distance (nm)	Radius (nm)	Length (nm)	Distance (nm)	Radius (nm)
254	267	29	281	283	30
3° director			Pertinence (gain)		
Length (nm)	Distance (nm)	Radius (nm)			
280	290	28	5		

Table 4: Optimal dimensions found by the fuzzy adaptive AGPSO method for YU nanoantenna connected to a transmission line.

Dipole			1° director		
Arm length (nm)	Radius (nm)		Length (nm)	Distance (nm)	Radius (nm)
272	16	300	90	25	
Reflector			2° director		
Length (nm)	Distance (nm)	Radius (nm)	Length (nm)	Distance (nm)	Radius (nm)
300	300	23	300	300	25
3° director			Transmission line		
Length (nm)	Distance (nm)	Radius (nm)	Length (nm)	Radius (nm)	Gap (nm)
300	300	25	500	30	30
Pertinence (gain)					
7.6					

Table 5: Optimal dimensions found by the fuzzy adaptive AGPSO method for YU nanoantenna combined to a rectangular loop.

Dipole			1° director		
Arm length (nm)	Radius (nm)		Length (nm)	Distance (nm)	Radius (nm)
280	20		300	300	25
Reflector			2° director		
Length (nm)	Distance (nm)	Radius (nm)	Length (nm)	Distance (nm)	Radius (nm)
300	300	20	300	300	25
3° director			Rectangular loop		
Length (nm)	Distance (nm)	Radius (nm)	Length (nm)	Distance (nm)	Radius (nm)	Height (nm)
300	300	25	610	60	25	30
Pertinence (gain)						
7.8						

Table 6: Optimal dimensions found by the fuzzy adaptive AGPSO method for YU nanoantenna connected to a transmission line and combined with a rectangular loop.

Dipole			1° director		
Arm length (nm)	Radius (nm)		Length (nm)	Distance (nm)	Radius (nm)
280	20		300	95	25
Reflector			2° director		
Length (nm)	Distance (nm)	Radius (nm)	Length (nm)	Distance (nm)	Radius (nm)
300	300	20	300	300	25
3° director			Rectangular loop		
Length (nm)	Distance (nm)	Radius (nm)	Length (nm)	Distance (nm)	Radius (nm)	Height (nm)
300	300	25	720	60	25	30
Transmission line			Pertinence (Gain)			
Length (nm)	Radius (nm)	Gap (nm)				
500	26	28	9.6			

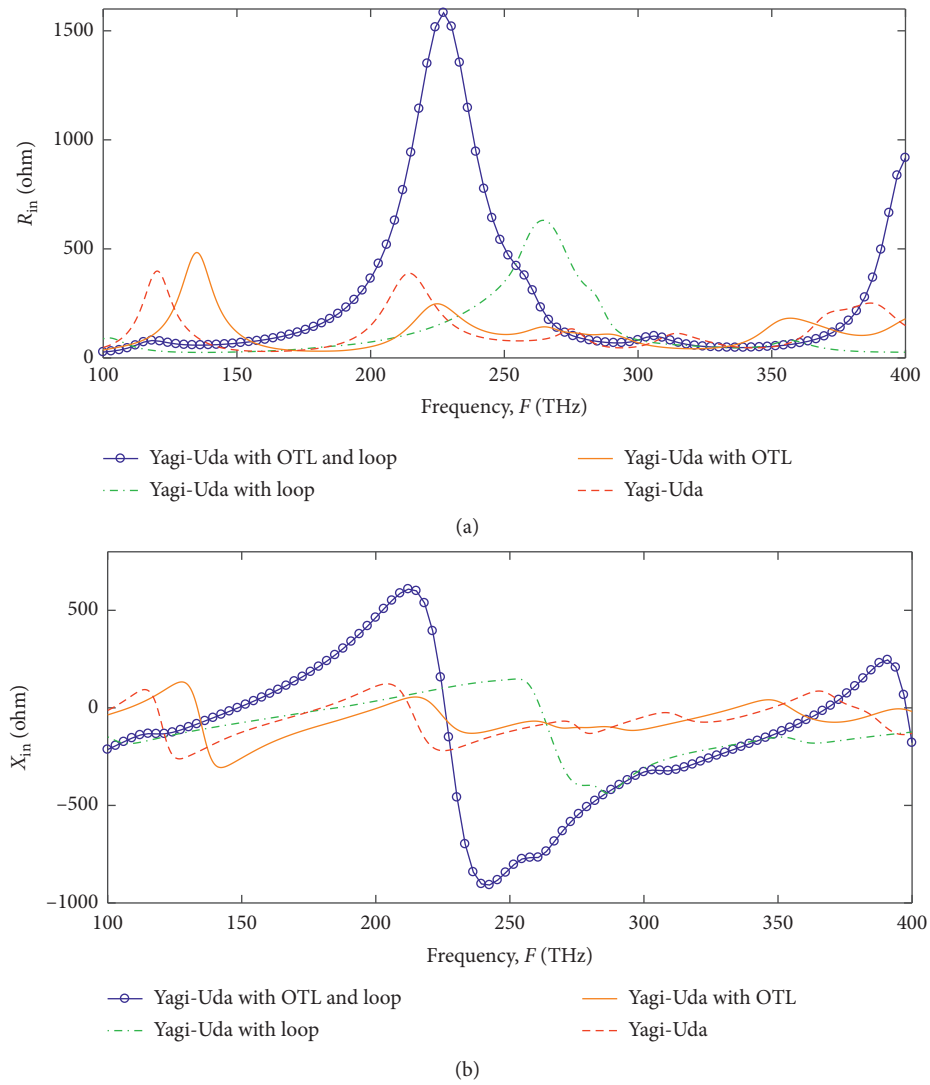

Figure 4: Variation of input impedance in frequency of the four YU nanoantennas: (a) R_{in} and (b) X_{in}.

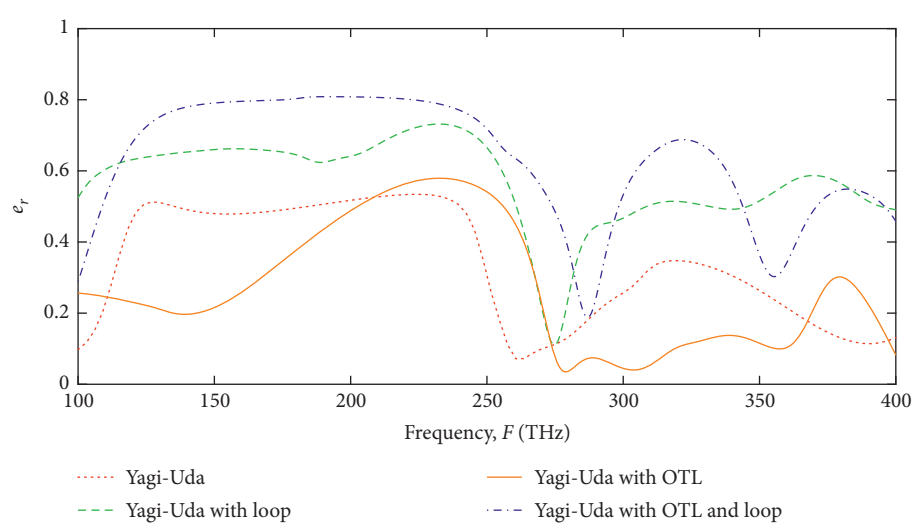

Figure 5: Radiation efficiency e_r of the four optimized YU nanoantennas.

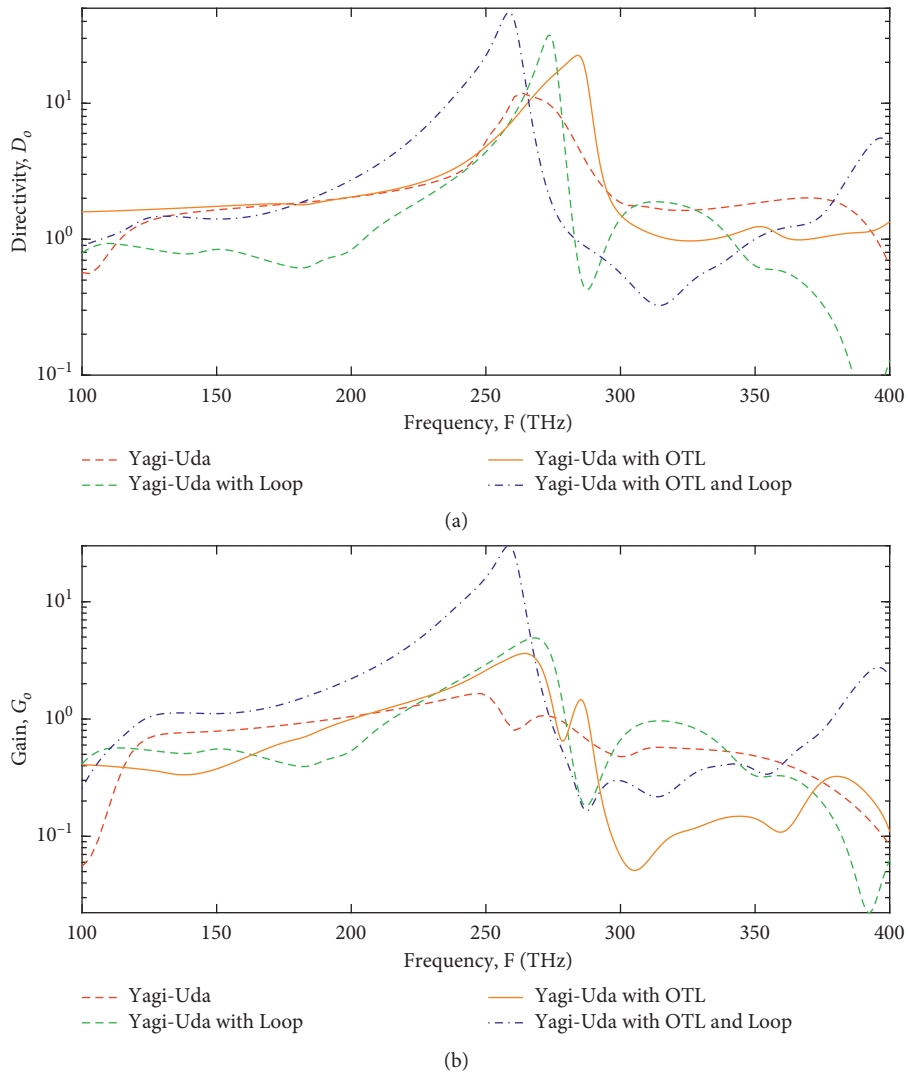

Figure 6: Directivity $(D)_0$ (a) and gain $(G)_0$ (b) of the four optimized YU nanoantennas.

Table 7: Resonance frequency and peak values of directivity of the four nanoantennas.

Nanoantenna	Frequency (THz)	D_0
Yagi-Uda	264	11.8
Yagi-Uda with OTL	284	22.5
Yagi-Uda with Loop	274	31.7
Yagi-Uda with OTL and Loop	259	46.5

Table 8: Resonance frequency and peak values of gain of the four nanoantennas.

Nanoantenna	Frequency (THz)	G_0
Yagi-Uda	247	1.65
Yagi-Uda with OTL	264	3.62
Yagi-Uda with Loop	268	4.91
Yagi-Uda with OTL and Loop	259	30

where it occurs. We observe from this table that the nanoantennas OTL and loop presented higher directivity than the other cases with OTL.

The maximum gain is also improved with the inclusions of these elements, as can be viewed in Table 8, where the gain of the conventional YU is increased from $G_0 = 1.65$ to 3.62 with the addition of the OTL and increases to 1.65 and 4.91 with the addition of the loop, and 1.65 to 30 for the case with loop and OTL.

5. Conclusions

In this paper, we presented the optimization of some radiation and absorption characteristics of four types of modified Yagi-Uda (YU) nanoantennas. The optimization technique used is the hybrid adaptive fuzzy GAPSO method. The results showed, in overall, that the insertion of new elements, such as loop elements and optical transmission line, in the geometry of the classic YU nanoantenna

produced improved values of efficiency, directivity, and gain when compared to the conventional one. It was also observed that the variation in spacing and dimensions of the elements considerably modifies the magnitude of directivity and gain. Another important conclusion obtained is that, for any YU antenna considered, the maximum gain does not necessarily occurs in the same frequency of maximum directivity. This means that the operation point depends in which characteristic directivity or gain that is more important in a given application. And finally, we observed that the adaptive fuzzy GAPSO is capable of optimizing any objective function with minimal restrictions. This makes this method an extremely versatile tool for modeling/optimization complex problems of nanoantennas.

Regarding the advantages of the nanoantennas proposed in this work, we observed that in general the performance of these are better than the conventional YU antenna, without significantly increasing their total size. These results may be useful for the design of efficient and compact YU nanoantennas for nanoplasmonic applications. The only disadvantage was the small increase in the overall input impedance of the proposed antennas compared to the conventional YU nanoantenna. In the future works, we intend to apply this optimization method in YU nanoantennas fed by Gaussian beam and optimize the impedance matching of these nanoantennas with optical transmission lines.

Data Availability

The data used to support this study can be available upon request to the corresponding author.

Conflicts of Interest

The authors declare that they have no conflicts of interest.

References

[1] P. Bharadwaj, B. Deutsch, and L. Novotny, "Optical antennas," *Advances in Optics and Photonics*, vol. 1, no. 3, pp. 438–483, 2009.

[2] L. Novotny and N. Van Hulst, "Antennas for light," *Nature Photonics*, vol. 5, no. 2, pp. 83–90, 2011.

[3] A. Alu and N. Engheta, "Theory, modeling and features of optical nanoantennas," *Institute of Electrical and Electronics Engineers Transactions on Antennas and Propagation*, vol. 61, no. 4, pp. 1508–1517, 2013.

[4] I. S. Maksymov, I. Staude, A. E. Miroshnichenko, and Y. S. Kivshar, "Optical Yagi-Uda nanoantennas," *Journal of Nanophotonics*, vol. 14, 2012.

[5] Q. Gao, S. Liverman, and A. X. Wang, "Design and characterization of high efficiency nanoantenna couplers with plasmonic integrated circuit," *Journal of Lightwave Technology*, vol. 35, no. 15, pp. 3182–3188, 2017.

[6] F. Obelleiro, J. M. Taboada, D. M. Solís, and L. Bote, "Directive antenna nanocoupler to plasmonic gap waveguides," *Optics Letters*, vol. 38, no. 10, pp. 1630–1632, 2013.

[7] E. G. Mironov, A. Khaleque, L. Liu, I. S. Maksymov, and H. T. Hattori, "Enhancing weak optical signals using a plasmonic yagi-uda nanoantenna array," *Institute of Electrical and Electronics Engineers Photonics Technology Letters*, vol. 26, no. 22, pp. 2236–2239, 2014.

[8] T. Kosako, Y. Kadoya, and H. F. Hofmann, "Directional control of light by a nano-optical yagi-uda antenna," *Nature Photonics*, vol. 4, no. 5, pp. 312–315, 2010.

[9] I. S. Maksymov, A. E. Miroshnichenko, and Y. S. Kivshar, "Actively tunable bistable optical Yagi-Uda nanoantenna," *Optics Express*, vol. 20, no. 8, pp. 8929–8938, 2012.

[10] K. Q. da Costa, G. T. C. de Sousa, P. R. Amaral, J. L. Souza, and P. N. dos Santos, "Wireless optical nanolinks with yagi-uda and dipoles plasmonic nanoantennas," *Nanoplamonics: Chapter 1*, Intech Open, London, UK, 2019.

[11] K. Q. Da Costa and V. Dmitriev, "Simple and efficient computational method to analyze cylindrical PlasmonicNanoantennas," *International Journal of Antennas e Propagation*, vol. 2014, Article ID 675036, 8 pages, 2014.

[12] U. Singh and R. Salgotra, "Pattern synthesis of linear antenna arrays using enhanced flower pollination algorithm," *International Journal of Antennas and Propagation*, vol. 2017, Article ID 7158752, 11 pages, 2017.

[13] R. Salgotra, U. Singh, S. Saha, and A. K. Nagar, "Improved flower pollination algorithm for linear antenna design problems," in *Soft Computing for Problem Solving. Advances in Intelligent Systems and Computing*, K. Das, J. Bansal, K. Deep, A. Nagar, P. Pathipooranam, and R. Naidu, Eds., vol. 1048, Springer, 2020.

[14] R. Salgotra, U. Singh, and S. Saha, "On some improved versions of whale optimization algorithm," *Arabian Journal for Science and Engineering*, vol. 44, no. 11, pp. 9653–9691, 2019.

[15] R. Salgotra and U. Singh, "The naked mole-rat algorithm," *Neural Computing and Applications*, vol. 31, no. 12, pp. 8837–8857, 2019.

[16] U. Singh, R. Salgotra, and M. Rattan, "A novel binary spider monkey optimization algorithm for thinning of concentric circular antenna arrays," *The Institution of Electronics and Telecommunication Engineers Journal of Research*, vol. 62, no. 6, pp. 736–744, 2016.

[17] Z. Michalewicz and M. Schoenauer, "Evolutionary algorithms for constrained parameter optimization problems," *Evolutionary Computation*, vol. 4, no. 1, pp. 1–32, 1996.

[18] COMSOL Inc., *COMSOL Multiphysic 4.4a*, COMSOL Inc., Bengaluru, India, 2013, http://www.comsol.com/.

[19] L. Novotny and B. Hecht, *Principles of Nano-Optics*, University of Cambridge, Cambridge, UK, 2 edition, 2012.

[20] K. Q. da Costa and E V. Dmitriev, "Software based on mom model to analyze electromagnetic transients in grounding systems," in *Proceedings of the International Conference on Grounding e Earthing& 2nd International Conference on Lightning Physics e Effects*, Manaus, Brazil, November 2006.

[21] J. H. Holle, "Genetic algorithms e adaptation," in *Adaptive Control of Ill-Defined Systems. NATO Conference Series (II Systems Science)*, O. G. Selfridge, E. L. Rissle, and A. ArbibM, Eds., Vol. 6, Springer, Boston, MA, USA, 1984.

[22] B. L. Miller and D. E. E Goldberg, "Genetic algorithms, tournament selection, and the effects of noise," *Complex System*, vol. 9, pp. 193–212, 1995.

[23] T. Higuchi, S. E Tsutsui, and M. Yamamura, "Theoretical analysis of simplex crossover for real-coded genetic algorithms," in *Parallel Problem Solving From Nature. PPSN VI. PPSN 2000. Lecture Notes in Computer Science*, M. Schoenauer et al., Ed., Vol. 1917, Springer, Berlin, Heidelberg, 2000.

[24] T. Yalcinoz and H. A. M. Uzam, "Economic dispatch solution using a genetic algorithm based on arithmetic crossover," in *Proceedings of the 2001 IEEE Porto Power Tech Proceedings (Cat. No. 01EX502)*, vol. 2, p. 4, Porto, Portugal, September 2001.

[25] W. M. Spearse, K. D. D. Jong, *On the Virtues of Parametrized Uniform Crossover*, Morgan Kaufman Publishing, Burlington, MA, USA, 1995.

[26] J. Hesser and R. Manner, "Towards an optimal mutation probability for genetic algorithms," in *Proceedings of the 1st Workshop on Parallel Problem Solving from Nature PPSN I*, pp. 23–32, Dortmund, Germany, October 1990.

[27] L. A. Zader, "Fuzzy logic, neural networks, and soft computing," *Communications of the ACM Association for Computing Machinery, Inc.*vol. 37, no. 3, pp. 77–85, 1994.

[28] E. H. Mamdani and S. Assilian, "An experiment in linguistic synthesis with a fuzzy logic controller," *International Journal of Man-Machine Studies*, Elsevier, vol. 7, no. 1, pp. 1–13, 1975.

[29] T. Tagaki and M. Sugeno, "Fuzzy identification of systems e its applications to modeling e control," *Institute of Electrical and Electronics Engineers Transactions on Systems, Man, E Cybernetics. Institute of Electrical and Electronics Engineers*, vol. 1, pp. 116–132, 1985.

[30] R. Eberhart and J. Kennedy, "A new optimizer using particle swarm theory," in *Proceedings of the IEEE Micro Machine e Human Science, 1995, MHS'95, Proceedings of the Sixth International Symposiu on*, pp. 39–43, Nagoya, Japan, October 1995.

[31] A. P. Engelbrecht, *Computational Intelligence: An Introduction*, John Wiley & Sons, Hoboken, NJ, USA, 2007.

Hindawi
International Journal of Antennas and Propagation
Volume 2021, Article ID 6658819, 7 pages
https://doi.org/10.1155/2021/6658819

Research Article

MTM- and SIW-Inspired Bowtie Antenna Loaded with AMC for 5G mm-Wave Applications

Ayman A. Althuwayb

Electrical Engineering Department, Jouf University, Sakaka, Aljouf 72388, Saudi Arabia

Correspondence should be addressed to Ayman A. Althuwayb; aaalthuwayb@ju.edu.sa

Received 13 November 2020; Revised 17 December 2020; Accepted 5 January 2021; Published 30 January 2021

Academic Editor: Luciano Mescia

This paper investigates a feasible configuration of slotted bowtie antenna based on MTM and SIW properties for 5G millimeter-wave applications. To realize the proposed slotted bowtie antenna in a compact dimension with high performances, the MTM and SIW concepts are implemented by applying the trapezoidal slots on the top surface of the antenna and metallic via holes through the substrate layer connecting the top surface to the ground plane. The antenna has been fed with a simple microstip-line which is connected to a waveguide-port. It is shown that the slotted bowtie antenna with a small dimension of $30 \times 16 \times 0.8\,\text{mm}^3$ operates over a measured wideband of 32–34.6 GHz with the fractional bandwidth, average gain, and radiation efficiency of 7.8%, 3.2 dBi, and 50%, respectively. To improve the antenna's performance, the artificial magnetic conductor (AMC) properties have been employed on the ground plane by loading vertical and linear slots with various lengths. The AMC slots are aligned under the trapezoidal slots on the top surface to transfer the maximum electromagnetic signals to them for optimum radiation. The proposed method enlarges the antenna's effective aperture area, keeping constant its physical dimensions. The proposed AMC-loaded antenna covers wider frequency range of 30–37 GHz in measurement, which corresponds to 21% fractional bandwidth. The average experimental gain and radiation efficiency have been increased to 5.5 dBi and 66.5%, respectively, which illustrate the effectiveness of the proposed AMC-loaded antenna. The results confirm that the proposed slotted bowtie antenna with advantages of compact dimension, wide bandwidth, high gain and efficiency, low profile, being cost-effective, simple design, and easy fabrication process, which makes it applicable for mass production, can be a good candidate for 5G millimeter-wave applications.

1. Introduction

The demand of high data rate wireless communication has become essential, and several approaches have been presented [1–3]. Broadband antenna methods have been paid the most attention for numerous benefits, such as immunity to multipath cancellation, low interference to legacy systems, increased communication operational security, and higher data rates [4–7]. The broadband antenna methods play a significant role in the short-range wireless communication systems. One of the difficulties to realize the broadband antennas is how to model them in a compact area with required electrical specifications in the desirable band [8–10]. Additionally, planar broadband antennas have gained attention for practical applications and mass productions because of their simple layout and easier-to-integrate as well as good impedance characteristics [11–13]. To implement a planar broadband antenna, the configuration of the antenna's patch, its ground plane, and feeding mechanism are important [14]. Various techniques such as the truncated slot on the surface of the antennas or their ground plane have been demonstrated to expand their frequency band [15–17]. Several planar broadband antennas introduced in [18–20] possess small dimension. However, they suffer from low gain and radiation efficiency, which are other very important properties in antenna systems that should be considered.

Composite right/left-handed transmission lines known as metamaterial transmission lines have been studied in recent years for many applications in microwave, millimeter-wave, terahertz, and optical domains [21–23]. These kinds of transmission lines are very helpful to design

antenna systems in a compact area with wide bandwidth and high radiation properties [24, 25]. Applications of metamaterial transmission lines in the design of antenna structures have been demonstrated in [26]. These transmission lines have implemented by four left-handed (LH) and right-handed (RH) parameters. It is worth to mention that, the LH components are manually realizable and controllable; however, the RH parameters are parasitic elements which are unwantedly available in the structure. These parameters are known as series LH capacitor (C_L), shunt LH inductor (L_L), shunt RH capacitance (C_R), and series RH inductance (L_R) [27–29].

Besides the metamaterial technique, the substrate integrated waveguide (SIW) and artificial magnetic conductor (AMC) approaches are other interesting ideas to suppress the substrate losses and surface waves to design antenna systems with favorable properties in a simple design structure [30–37].

The frequency bandwidth from 3 GHz to 300 GHz known as centimeter-wave (cm-wave) and millimeter-wave (mm-wave) spectra have attracted by fifth generation (5G) technology because it can provide the data rate up to numerous gigabit-per-second (Gbps). Other reason to select this area is that the lower band's availability has formerly been utilized by many wireless systems, while most of the spectrum's upper portion is not used and can be accessible for 5G technology [38, 39].

Therefore, in this paper, three effective approaches inspired MTM, SIW, and AMC have been presented and developed to design a slotted bowtie antenna with compact dimension, wide bandwidth, and high radiation properties for application to 5G wireless communication systems over millimeter-wave band. First, the metamaterial approach and substrate integrated waveguide techniques are applied to the structure of a bowtie antenna to increase its effective aperture area by employing the trapezoidal slots and metallic via holes through the substrate layer connecting the top surface to the ground plane, which diminish the surface waves and substrate losses. After applying the proposed methods, it is shown that the proposed antenna can cover a wide frequency band with high radiation properties. To achieve more improvements on the antenna's performance parameters, the AMC technique has been applied to antenna's ground plane by etching the linear and vertical slots with various lengths exactly aligned underneath the trapezoidal slots to coupling maximum electromagnetic energy to the top surface to have optimum radiation. The achievements in this paper confirm the effectiveness of the proposed approaches. In the next step, the antenna's design process is discussed in detail.

2. Slotted Bowtie Antenna Design Procedure

Figure 1 displays the proposed bowtie antenna which has tooled, designed and fabricated on the Rogers RT5880 substrate with thickness of 0.8 mm, dielectric constant of $\varepsilon_r = 2.2$, and $\tan\delta = 0.0009$. It is clear from Figure 1 that to realize the slotted bowtie configuration, the trapezoidal slots have been etched on the top surface of the antenna to enlarge the antenna's effective aperture area without expanding its physical dimensions. These two trapezoidal slots have been implemented in a series configuration using the properties of metamaterial transmission lines [29]. In other words, these two trapezoidal slots in a series configuration play the role of the series LH capacitances (C_L). Besides C_L implemented by the trapezoidal slots, another main component of the metamaterial structures is shunt LH inductance (L_L) which is implemented here via employing the substrate integrated waveguide (SIW) concept by realizing the metallic via holes at the edge of the structure. These metallic via holes have been modeled across the Rogers RT5880 dielectric substrate layer, and they connect the top surface of the antenna to its ground plane located on the back side. The main advantage of the SIW approach is that it reduces the substrate losses and suppresses the surface waves without increasing the physical dimensions, which has led to improve the antenna's performances such as impedance matching, impedance bandwidth, and radiation specifications.

It is worth to comment that the RH parasitic effects such as shunt RH capacitances (C_R) and series RH inductances (L_R) are usually unavoidable and excised in the structure. They have been established with existence of the gap distance between the top surface and the ground plane and flowing currents on the surface, respectively [40]. Hence, the purely LH materials are not available in the nature. Therefore, the proposed metamaterial-inspired bowtie antenna is named as composite right/left-handed- (CRLH-) based bowtie antenna structure. The equivalent circuit model of the proposed metamaterial-based bowtie antenna is shown in Figure 1 to better understand its LC behavior.

The simulated layouts and fabricated prototypes of the proposed slotted bowtie antenna-inspired MTM and SIW concepts with dimensions of $30 \times 16 \times 0.8\,\text{mm}^3$ are exhibited in Figure 1. Figure 2 shows that the proposed antenna operates over a wide frequency range between 32 GHz and 34.6 GHz, which corresponds to 9% fractional bandwidth. Besides the frequency bandwidth, it is exhibited in Figure 3 that the minimum, maximum, and average amounts of the radiation gain and efficiency of the proposed slotted bowtie antenna are 3 dBi, 3.5 dBi, and 3.2 dBi and 48%, 53%, and 50%, respectively. The proposed antenna has excited by a simple microstrip-line which is connected to a waveguide port. The proposed antenna was designed by 3D full-wave electromagnetic CST Microwave Studio.

To improve the antenna's performance, a simple and feasible approach based on the artificial magnetic conductor (AMC) concept [28, 33] has been applied to the antenna's ground plane by realizing the vertical and linear slots in various lengths, as shown in Figures 1(c) and 1(g). Besides the trapezoidal slots implemented on the top side, the AMC slots play the role of the series LH capacitance (C_L) as complementary parameter to improve the left-handed (LH) properties of the antenna structure (see Figure 1(h)). It is obvious that by loading the AMC slots, the antenna's physical size is not changed; however, its effective aperture area is expanded, which improves the performance

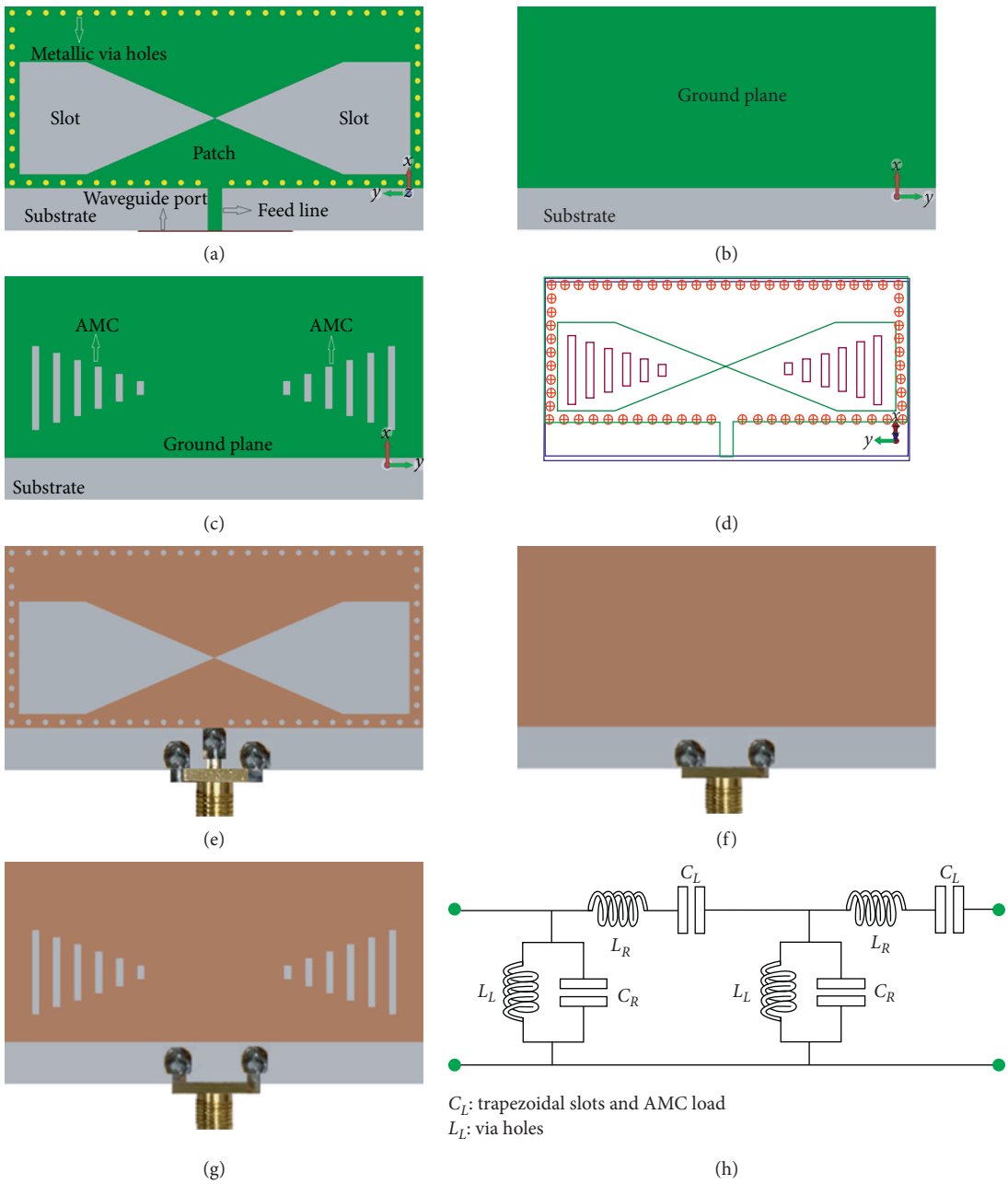

Figure 1: Configuration of the proposed bowtie antenna structure: (a) top view of the simulated layout based on the metamaterial properties and SIW concepts; (b) ground plane without AMC; (c) ground plane loaded with AMC; (d) schematic view to show all structural components designed on the top and bottom sides; (e) fabricated prototype (top view); (f) fabricated prototype without AMC load (back view); (g) fabricated prototype loaded with AMC (back view); (h) equivalent circuit model.

parameters such as bandwidth and radiation properties, which are shown in next steps. Furthermore, to transfer maximum electromagnetic energy from the bottom side to the top side, these AMC slots have been aligned exactly underneath the trapezoidal slots to accomplish the optimum radiation. In the following parts, the effectiveness of the AMC load is exhibited and elaborated in detail. The structural parameters of the antenna were optimized by the 3D full-wave electromagnetic CST Microwave Studio and are listed in Table 1.

The simulated and measured reflection coefficient responses ($S_{11} < -10$ dB) for both metamaterial- and SIW-based bowtie antennas without and with AMC load are plotted in Figure 2. It is obvious that the simulated and measured results for both antennas have good agreement with each other. This figure depicts that after loading the AMC slots to the ground plane, the antenna's bandwidth is expanded by 4.4 GHz, and so the AMC-loaded antenna supports the broader frequency band between 30 GHz and 37 GHz across the millimeter-wave area. Consequently, the

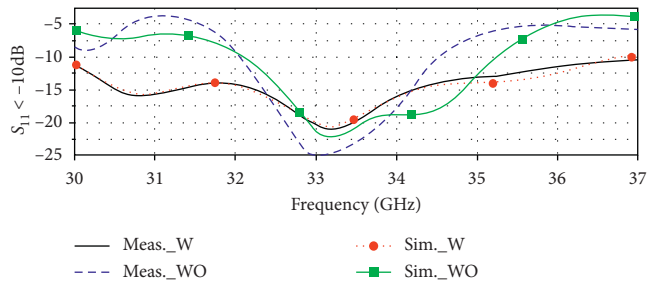

Figure 2: Simulated and measured reflection coefficient responses ($S_{11} < -10$ dB) before (WO) and after (W) applying artificial magnetic conductor (AMC) load.

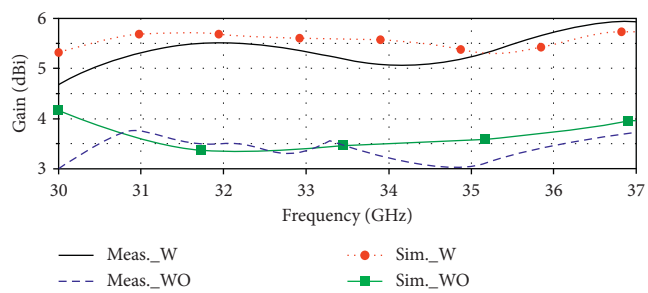

Figure 3: Simulated and measured radiation gain curves over the frequency band for both bowtie antennas without (WO) and with (W) AMC load.

Table 1: Bowtie antenna's structural parameters.

Bowtie antenna dimensions	$30 \times 16 \times 0.8\,\text{mm}^3$
Ground plane dimensions	$30 \times 13 \times 0.8\,\text{mm}^3$
Length of the trapezius slots	14 mm
Maximum width of the trapezius slots	$0\,\text{mm} < L \leq 8\,\text{mm}$
Radius of via holes	0.2 mm
Distance between via holes	0.4 mm
Length of AMC slots	$1\,\text{mm} \leq L \leq 6\,\text{mm}$
Width of AMC slots	0.5 mm
Distance between AMC slots	1 mm
Length of feed line	3 mm
Width of feed line	1 mm
Substrate height	0.8 mm

fractional bandwidth is enhanced to 21% which illustrates 13.2% improvement compared to the antenna without AMC load. Besides the frequency band, it is clear from Figure 2 that the antenna's bandwidth after AMC loading is more stable in comparison with the case without AMC load. To better understand the effectiveness of the AMC load on the antenna's bandwidth, the measured S-parameter results are summarized in Table 2.

Besides the frequency bandwidth, the radiation characteristics such as gain and efficiency are other main performance parameters that should be considered to design antenna systems. The simulated and measured radiation gain curves for both metamaterial- and SIW-inspired bowtie antennas before and after applying the AMC load are plotted in Figure 3. It is shown that the minimum, maximum, and average amounts of the radiation gain for the antenna loaded with AMC are 4.7 dBi, 6.0 dBi, and 5.5 dBi, respectively, which show 1.7 dBi (57%), 2.5 dBi (71.5%), and 2.3 dBi (72%) improvements in comparison with the bowtie antenna without AMC load. From Figure 3, it is clear that the simulated and measured results for both antennas have good coherence with each other. Additionally, after applying the AMC load, the gain curves are more stable than the case without AMC load. The radiation gain performances for both bowtie antennas without and with AMC load are summarized in Table 3.

The simulated and measured radiation efficiency curves for both bowtie antennas without and with AMC load are exhibited in Figure 4. Obviously, the simulated results have good agreement with the measured ones. It is shown that a significant improvement has been achieved after applying the AMC load across the operating bandwidth. The minimum, maximum, and average values of the radiation efficiency for the bowtie antenna loaded with AMC are 64%, 68%, and 66.5%, respectively, which explain the improvements of 16%, 15%, and 16.5% compared to the antenna without AMC load. To have a better understanding of the effectiveness of the AMC load on the radiation efficiency, Table 4 summarizes the radiation efficiency values before and after applying AMC load.

The results presented in Figures 2–4 and Tables 2–4 confirm the effectiveness of the AMC load on the antenna's performance parameters. These achievements show that the proposed slotted bowtie antenna realized based on the metamaterial, SIW, and artificial magnetic conductor (AMC) properties with the advantages of compact dimensions, wide bandwidth, high radiation gain and efficiency, low profile, being cost-effective, simple design, and easy fabrication process

Table 2: Effectiveness of AMC load on the antenna's reflection coefficient responses.

Measured frequency bandwidth	$S_{11} < -10$ dB	Frequency band length (GHz)	Fractional bandwidth (%)
Antenna without AMC	32–34.6 GHz	2.6	7.8
Antenna loaded with AMC	30–37 GHz	7	21
Improvement after AMC load		4.4 GHz	13.2

Table 3: Effectiveness of the AMC load on the radiation gain.

Measured radiation gain	Minimum	Maximum	Average
Antenna without AMC	3 dBi	3.5 dBi	3.2 dBi
Antenna loaded with AMC	4.7 dBi	6.0 dBi	5.5 dBi
Improvement after AMC load	1.7 dBi ≅ 57%	2.5 dBi ≅ 71.5%	2.3 dBi ≅ 72%

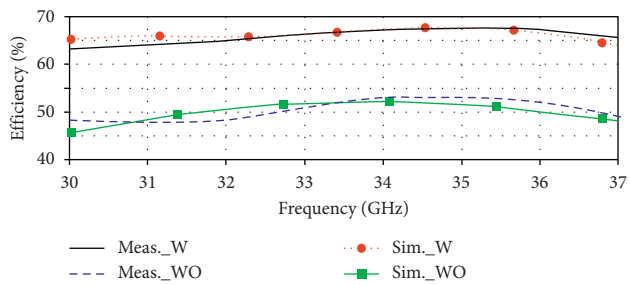

Figure 4: Simulated and measured radiation efficiency curves over the bandwidth for both bowtie antennas without (WO) and with (W) AMC load.

Table 4: Effectiveness of the AMC load on the radiation efficiency.

Measured radiation efficiency	Minimum (%)	Maximum (%)	Average (%)
Antenna without AMC	48	53	50
Antenna loaded with AMC	64	68	66.5
Improvement after AMC load	16	15	16.5

can be used for mass production in practice, and looking at its operating frequency band and radiation properties, it is a proper candidate for applications to 5G wireless communication systems over millimeter-wave band.

3. Conclusion

Feasibility of three simple but effective approaches inspired by metamaterial (MTM), substrate integrated waveguide (SIW), artificial magnetic conductor (AMC) contents has been studied and investigated in this research work to design an innovative configuration of a slotted bowtie antenna operating from 30 GHz to 37 GHz that is applicable to lower band of 5G millimeter-wave area. To create a bowtie layout, two trapezius-shaped slots have been realized in a series configuration. It is shown that after applying the MTM and SIW principles, a wide frequency bandwidth along with high radiation performances has been achieved without affecting the physical dimensions. Then, to achieve broader bandwidth with higher radiation specifications, the AMC technique has been applied to the ground plane, keeping constant the physical size. To have optimum radiation, the AMC slots have been exactly alighted underneath two trapezoidal slots. The results show that after applying AMC load, the antenna's measured bandwidth, fractional bandwidth, gain, and radiation efficiency have improved by 4.4 GHz, 13.2%, 2.3 dBi, and 16.5%, respectively, in a compact footprint area of 30×16×0.8 mm^3, which shows the effectiveness of the proposed approaches. Therefore, the proposed slotted bowtie antenna can be used for applications to 5G wireless communication systems in millimeter-wave region.

Data Availability

The data used to support the findings of this study are included within the article.

Conflicts of Interest

The author declares that there are no conflicts of interest.

References

[1] L. Rakotondrainibe, Y. Kokar, G. Zaharia, and G. El Zein, "Millimeter-wave system for high data rate indoor communications," in *Proceedings of the 2009 International Symposium on Signals, Circuits and Systems*, pp. 1–4, Iasi, Romania, July 2009.

[2] M. Alibakhshikenari, B. S. Virdee, C. H. See, and P. Shukla, "Study on improvement of the performance parameters of a novel 0.41–0.47 THz on-chip antenna based on metasurface concept realized on 50 μm GaAs-layer," *Scientific Reports*, vol. 10, Article ID 11034, 2020.

[3] M. Alibakhshikenari, B. S. Virdee, C. H. See et al., "High-gain metasurface in polyimide on-chip antenna based on CRLH-TL for sub terahertz integrated circuits," *Scientific Reports*, vol. 10, p. 4298, 2020.

[4] M. Alibakhshikenari, B. S. Virdee, P. Chukla et al., "Metamaterial-inspired antenna array for application in microwave breast imaging systems for tumor detection," *IEEE Access*, vol. 8, pp. 174667–174678, 2020.

[5] M. Alibakhshikenari, B. S. Virdee, M. Khalily et al., "High-gain on-chip antenna design on silicon layer with aperture excitation for terahertz applications," *IEEE Antennas and Wireless Propagation Letters*, vol. 19, no. 9, pp. 1576–1580, 2020.

[6] R. J. Fontana, "Recent system applications of short-pulse ultra-wideband (UWB) technology," *IEEE Transactions on Microwave Theory and Techniques*, vol. 52, no. 9, pp. 2087–2104, 2004.

[7] L. Li, Z.-L. Zhou, and J.-S. Hong, "Design and analysis of a novel compact wideband Antenna with two excited modes," *International Journal of Antennas and Propagation*, vol. 2012, Article ID 351038, 5 pages, 2012.

[8] M. Alibakhshikenari, E. Limiti, M. Naser-Moghadasi, B. S. Virdee, and R. A. Sadeghzadeh, "A new wideband planar antenna with band-notch functionality at GPS, bluetooth and WiFi bands for integration in portable wireless systems," *AEUE Elsevier- International Journal of Electronics and Communications*, vol. 72, pp. 79–85, 2017.

[9] T. Saeidi, I. Ismail, W. P. Wen, A. R. H. Alhawari, A. Mohammadi, and M. Ahmad, "Ultra-wideband Antennas for wireless communication applications," *International Journal of Antennas and Propagation*, vol. 2019, Article ID 7918765, 25 pages, 2019.

[10] C. A. Balanis, *Antenna Theory: "Analysis and Design"*, John Wiley, Hoboken, NJ, USA, 3rd edition, 2005.

[11] A. Azari, "A new super wideband fractal microstrip antenna," *IEEE Transactions on Antennas and Propagation*, vol. 59, no. 5, pp. 1724–1727, 2011.

[12] S. Dey and N. C. Karmakar, "Design of novel super wide band antenna close to the fundamental dimension limit theory," *Scientific Reports*, vol. 10, no. 1, p. 16306, 2020.

[13] T. Okan, "A compact octagonal-ring monopole antenna for super wideband applications," *Microwave and Optical Technology Letters*, vol. 62, no. 3, pp. 1237–1244, 2019.

[14] S. Kumar, G. H. Lee, D. H. Kim, N. S. Haunan, H. C. Choi, and K. W. Kim, "Compact planar super-wideband monopole antenna with four notched bands," *Electronics*, vol. 9, no. 8, p. 1204, 2020.

[15] C. Á. Figueroa-Torres, J. L. Medina-Monroy, H. Lobato-Morales, R. A. Chávez-Pérez, and A. Calvillo-Téllez, "A novel fractal antenna based on the Sierpinski structure for super wide-band applications," *Microwave and Optical Technology Letters*, vol. 59, no. 5, pp. 1148–1153, 2017.

[16] S. Singhal and A. K. Singh, "Modified star-star fractal (MSSF) super-wideband antenna," *Microwave and Optical Technology Letters*, vol. 59, no. 3, pp. 624–630, 2017.

[17] P. Okas, A. Sharma, G. Das, and R. K. Gangwar, "Elliptical slot loaded partially segmented circular monopole antenna for super wideband application," *AEU—International Journal of Electronics and Communications*, vol. 88, pp. 63–69, 2018.

[18] W. Balani, M. Sarvagya, T. Ali et al., "Design techniques of super-wideband antenna-existing and future prospective," *IEEE Access*, vol. 7, pp. 141241–141257, 2019.

[19] S. U. Rahman, Q. Cao, H. Ullah, and H. Khalil, "Compact design of trapezoid shape monopole antenna for SWB application," *Microwave and Optical Technology Letters*, vol. 61, no. 8, pp. 1931–1937, 2019.

[20] S. Singhal, "Asymmetrically fed octagonal Sierpinski band-notched super-wideband antenna," *Journal of Computational Electronics*, vol. 16, no. 1, pp. 210–219, 2017.

[21] M. Mohammadi, F. H. Kashani, and J. Ghalibafan, "Backfire-to-endfire scanning capability of a balanced metamaterial structure based on slotted ferrite-filled waveguide," *Waves Random Complex Media*, pp. 1–15, 2019.

[22] C. Caloz and T. Itoh, *Electromagnetic Metamaterials: Transmission Line Theory and Microwave Applications*, Wiley-IEEE Press, Hoboken, NJ, USA, 2005.

[23] M. Alibakhshikenari, B. S. Virdee, L. Azpilicueta et al., "A comprehensive survey of "metamaterial transmission-line based antennas: design, challenges, and applications"" *IEEE Access*, vol. 8, pp. 144778–144808, 2020.

[24] M. Shirkolaei and J. Ghalibafan, "Unbalanced CRLH behavior of ferrite-loaded waveguide operated below cutoff frequency," *Waves in Random and Complex Media*, 2020.

[25] M. Alibakhshi-Kenari, M. Naser-Moghadasi, and R. A. Sadeghzadeh, "Composite right-left-handed-based antenna with wide applications in very-high frequency-ultra-high frequency bands for radio transceivers," *IET Microwaves, Antennas & Propagation*, vol. 9, no. 15, pp. 1713–1726, 2015.

[26] K. L. Chung, "High-performance circularly polarized antenna array using metamaterial-line based feed network," *IEEE Transactions on Antennas and Propagation*, vol. 61, no. 12, pp. 6233–6237, 2013.

[27] M. Mohammadi, F. H. Kashani, and J. Ghalibafan, "A partially ferrite-filled rectangular waveguide with CRLH response and its application to a magnetically scannable antenna," *Journal of Magnetism and Magnetic Materials*, vol. 491, Article ID 165551, 2019.

[28] M. Alibakhshi-Kenari, M. Naser-Moghadasi, R. A. Sadeghzadeh et al., "Bandwidth and radiation specifications enhancement of monopole antennas loaded with split ring resonators," *IET Microwaves, Antennas & Propagation*, vol. 9, no. 14, pp. 1487–1496, 2015.

[29] K. L. Chung, X. Yan, S. Chaimool, B. Feng, and Y. Li, "On the surface susceptibilities and effective parameters of metasurfaces composed of isolated metallic unit-cells," *International Journal of RF and Microwave Computer-Aided Engineering*, vol. 31, no. 2, 2020.

[30] K. Kumar, S. Dwari, and S. Priya, "Dual band dual polarized cavity backed cross slot half mode substrate integrated waveguide antenna," in *Proceedings of the 2017 IEEE Applied Electromagnetics Conference (AEMC)*, pp. 1-2, Aurangabad, India, December 2017.

[31] M. Alibakhshikenari, B. S. Virdee, C. H. See et al., "Beam-scanning leaky-wave antenna based on CRLH-metamaterial for millimeter-wave applications," *IET Microwaves, Antennas & Propagation*, vol. 13, no. 8, pp. 1129–1133, 2019.

[32] R. Bayderkhani, K. Forooraghi, and B. Abbasi-Arand, "Gain-enhanced SIW cavity-backed slot antenna with arbitrary levels of inclined polarization," *IEEE Antennas and Wireless Propagation Letters*, vol. 14, pp. 931–934, 2015.

[33] M. Alibakhshikenari, B. S. Virdee, M. Khalily et al., "New approach to suppress mutual coupling between longitudinal-slotted arrays based on SIW antenna loaded with metal-fences

working on VHF/UHF frequency-bands: study, investigation, and principle," in *Proceedings of the 2018 Asia-Pacific Microwave Conference (APMC)*, pp. 1564–1566, Kyoto, Japan, November 2018.

[34] S. Mukherjee and A. Biswas, "Design of dual band and dual-polarised dual band SIW cavity backed bow-tie slot antennas," *IET Microwaves, Antennas & Propagation*, vol. 10, no. 9, pp. 1002–1009, 2016.

[35] M. Alibakhshikenari, B. S. Virdee, C. H. See et al., "Mutual-coupling reduction in metamaterial substrate integrated waveguide slotted antenna arrays using metal fence isolators for SAR and MIMO applications," in *Proceedings of the 2018 12th International Congress on Artificial Materials for Novel Wave Phenomena (Metamaterials)*, pp. 13–15, Espoo, Finland, August 2018.

[36] M. Mbaye, J. Hautcoeur, L. Talbi, and K. Hettak, "Bandwidth broadening of dual-slot antenna using substrate integrated waveguide (SIW)," *IEEE Antennas and Wireless Propagation Letters*, vol. 12, pp. 1169–1171, 2013.

[37] M. Alibakhshi-Kenari, M. Naser-Moghadasi, R. A. Sadeghzadeh, B. S. Virdee, and E. Limiti, "Periodic array of complementary artificial magnetic conductor metamaterials-based multiband Antennas for broadband wireless transceivers," *IET Microwaves, Antennas & Propagation*, vol. 10, no. 15, pp. 1682–1691, 2016.

[38] B. Feng, Y. Tu, J. Chen, S. Yin, and K. L. Chung, "Dual linearly-polarized antenna array with high gain and high isolation for 5G millimeter-wave applications," *IEEE Access*, vol. 8, pp. 82471–82480, 2020.

[39] D. A. Sehrai, M. Abdullah, A. Altaf et al., "A novel high gain wideband MIMO antenna for 5G millimeter wave applications," *Electronics*, vol. 9, no. 6, p. 1031, 2020.

[40] B. Feng, J. Lai, Q. Zeng, and K. L. Chung, "A dual-wideband and high gain magneto-electric dipole antenna and its 3D MIMO system with metasurface for 5G/WiMAX/WLAN/X-Band Applications," *IEEE Access*, vol. 6, pp. 33387–33398, 2018.

Hindawi
International Journal of Antennas and Propagation
Volume 2020, Article ID 6653095, 9 pages
https://doi.org/10.1155/2020/6653095

Research Article

On-Chip Antenna Design Using the Concepts of Metamaterial and SIW Principles Applicable to Terahertz Integrated Circuits Operating over 0.6–0.622 THz

Ayman A. Althuwayb

Electrical Engineering Department, Jouf University, Sakaka, Aljouf 72388, Saudi Arabia

Correspondence should be addressed to Ayman A. Althuwayb; aaalthuwayb@ju.edu.sa

Received 28 October 2020; Revised 10 November 2020; Accepted 22 November 2020; Published 8 December 2020

Academic Editor: Diego Caratelli

This research work presents the investigation of realizing an on-chip antenna based on the metamaterial concept, which is working over the terahertz (THz) band for applications in integrated circuits. The proposed on-chip antenna is constructed of five stacked layers of polyimide and aluminum as top and bottom substrates, radiation patches, ground plane, and feed line. The four square-shaped radiation patches are implemented on the 50 μm top-polyimide substrate, and the feed line is realized on the 50 μm bottom-polyimide layer by designing the simple square microstrip lines, which are all connected to each other and then excited by waveguide port. The ground plane including a coupling square slot has sandwiched between the top- and bottom-polyimide layers. The coupling square slot etched on the ground plane is exactly placed under the patch to optimum transfer the electromagnetic signal from the bottom feed line to the top radiation patch. To achieve high performance parameters without increasing the antenna's physical dimensions, the metamaterial and substrate integrated waveguide properties have been applied to the antenna structure by implementing linear tapered slots on the patch top surfaces and metallic via holes throughout the middle ground plane connecting top and bottom substrates to each other. The slots play the role of series left-handed (LH) capacitors (C_L) and the via holes act as shunt LH inductors (L_L). The overall dimension of the proposed metamaterial-based on-chip antenna is $1000 \times 1000 \times 100\,\mu m^3$. This antenna can cover the frequency band from 0.6 THz to 0.622 THz, which is equal to 20 GHz bandwidth. The radiation gain and efficiency across the operating frequency band varies from 1.1 dBi to 1.8 dBi, and from 58% to 60.5%, respectively. The results confirm that the proposed on-chip antenna with compact dimensions, wide bandwidth over the terahertz domain, low profile, cost effective, simple configuration, and easy to manufacture can be potentially appropriate for terahertz integrated circuits.

1. Introduction

The millimeter-wave (mmW) and terahertz (THz) systems are being utilized for radio astronomy and imaging applications. Enhancing the requests for low-cost circuits and more data transfer at these bands has caused potential commercial applications such as automotive radars and high data rate systems [1–4]. These bands are attractive since with the reducing wavelengths the components physical size can be decreased, so in a specific physical area denser arrays can be constructed. These applications become practical only if the solutions can be effective and highly integrated and at low cost [5–7].

In addition to the size decrement benefit, moving toward higher bands brings new tasks. Lossy silicon layers are not pleasantly suitable for realizing effective antennas, and for the devices operating over the microwave band, the antenna sizes make them the largest elements of the system that create them infeasible to produce on-chip. Antennas can operate effectively on low-loss printed circuit boards (PCB) that need interconnects between the antenna and the chips.

Although, as the frequency moves higher, the matching networks and interconnects become lossier. Bond-wire interconnects restrict the functionality as they decrease the frequency band because of parasitic reactance. An alternative, flip-chip bonding enhances the cost. Hence, possible low-cost on-chip antenna solutions are of great interest [8, 9].

On-chip antennas enable system-on-chip (SoC) solutions, omitting the demand for conventional 50-ohm interfaces and lossy RF interconnects [10]. Although, on-chip antennas present major difficulties because of physical constraints, low resistivity (10 Ω·cm) silicon, that is, the typical layer of commercial integrated circuit processes forbids the effective antenna implementation. As well as, a considerable amount of power is coupled to the surface-wave modes on silicon substrates [11, 12]. Although, typical integrated circuit processes enable an oxide layer thickness of ~10 μm that is still not sufficient in mm-W and THz bands, off-chip radiator and lens based solutions have been introduced in [13–15]. Off-chip radiators need post-manufacture steps on other layers, and lenses are bulky in comparison with the size of the chips. Utilizing high-permittivity superstrates provides a solution without the demand of additional manufacture steps and still achieves high efficiency on-chip antennas [16]. The main drawback of this method is the complexity of the design process and not applicable for mass production in a cost-effective method. Additionally, the on-chip antennas are operating on a narrow bandwidth.

Therefore, in this paper an on-chip antenna has proposed which is implemented on 50 μm polyimide layers. The antenna structure has constructed from five stacked layers of two polyimide substrates and three aluminum layers as radiation patches, middle ground plane, and bottom feed line. The radiating patches have been isolated from the lossy polyimide by a ground plane, which eliminates the polyimide loss effect and causes the antenna to have a very thin substrate degrading the frequency bandwidth, radiation gain, and efficiency, which also makes the antenna unidirectional. The antenna excited by a microstrip feed line was placed on the bottom polyimide layer through coupling the electromagnetic signals to the top radiation patch through the coupling slot etched on the sandwiched ground plane realized between the two top- and bottom-polyimide substrates. The metallic via-hole-inspired substrate integrated waveguides (SIW) are also implemented to connect both polyimide layers to each other to reduce their losses and suppress the surface waves. Additionally, the metamaterial (MTM) property has employed to the radiation patches to extend their effective aperture area to improve the performance parameters. It is shown, after applying both SIW and MTM approaches, the on-chip antenna with simple design structure and compact dimensions exhibits wide bandwidth over terahertz (THz) territory, high radiation gain, and efficiency over the operating bandwidth. The design process of the proposed on-chip antenna has been presented and investigated in Section 2. The results confirm that the proposed on-chip antenna can be applicable for integration in THz circuits.

2. Design Process of the 50 μm Polyimide Layer-Based On-Chip Antenna Design-Inspired MTM and SIW Properties for THz-Integrated Circuit Applications

The configuration of the proposed on-chip antenna has been shown in Figure 1. The proposed antenna has constructed of five stacked layers of aluminum (radiation patches)-polyimide substrate aluminum (sandwiched ground plane)-polyimide substrate aluminum (microstrip feed line). The thickness, dielectric constant, and tangent loss of the polyimide substrates are 50 μm, 3.5, and 0.0027, respectively. As it is obvious from Figure 1(a), on the top polyimide layer, four radiation patches with square shape have modeled, which all have been connected to each other by simple linear microstrip lines, since the antenna is excited only by one waveguide port. Underneath of the top polyimide substrate, the antenna's ground plane (GND) has been implemented, as shown in Figure 1(b). By realizing this GND layer, the antenna structure can be isolated from the lossy polyimide layer, which causes to improve the radiation properties and impedance matching of the antenna. Besides that, a square slot has been etched inside the GND layer as a coupling slot to transfer the electromagnetic (EM) energy to the top radiation patches. This slot is exactly aligned under the radiation patch to couple the optimum EM signal for the radiation process. The GND layer from its bottom side has been connected to the second polyimide layer as the bottom substrate with the same specifications with the top polyimide substrate. As it is displayed in Figure 1(c), underneath the bottom-polyimide substrate, a simple microstrip line is realized as the feeding line that, from its one side, has connected to the waveguide port to excite the structure. The schematic view of the proposed structure is shown in Figure 1(d), which clearly explains that this feeding line is exactly placed underneath the coupling slot etched inside the GND to transfer the maximum EM signal to the coupling slot, and consequently coupling the maximum EM signal from the GND's slot to the radiation patches on the top side of the top polyimide substrate to have optimum signal radiation. To suppress the substrate losses and diminish the surface waves, the SIW concept has been applied by implementing metallic via holes on the edges of the structure throughout the GND layer connecting both top- and bottom-

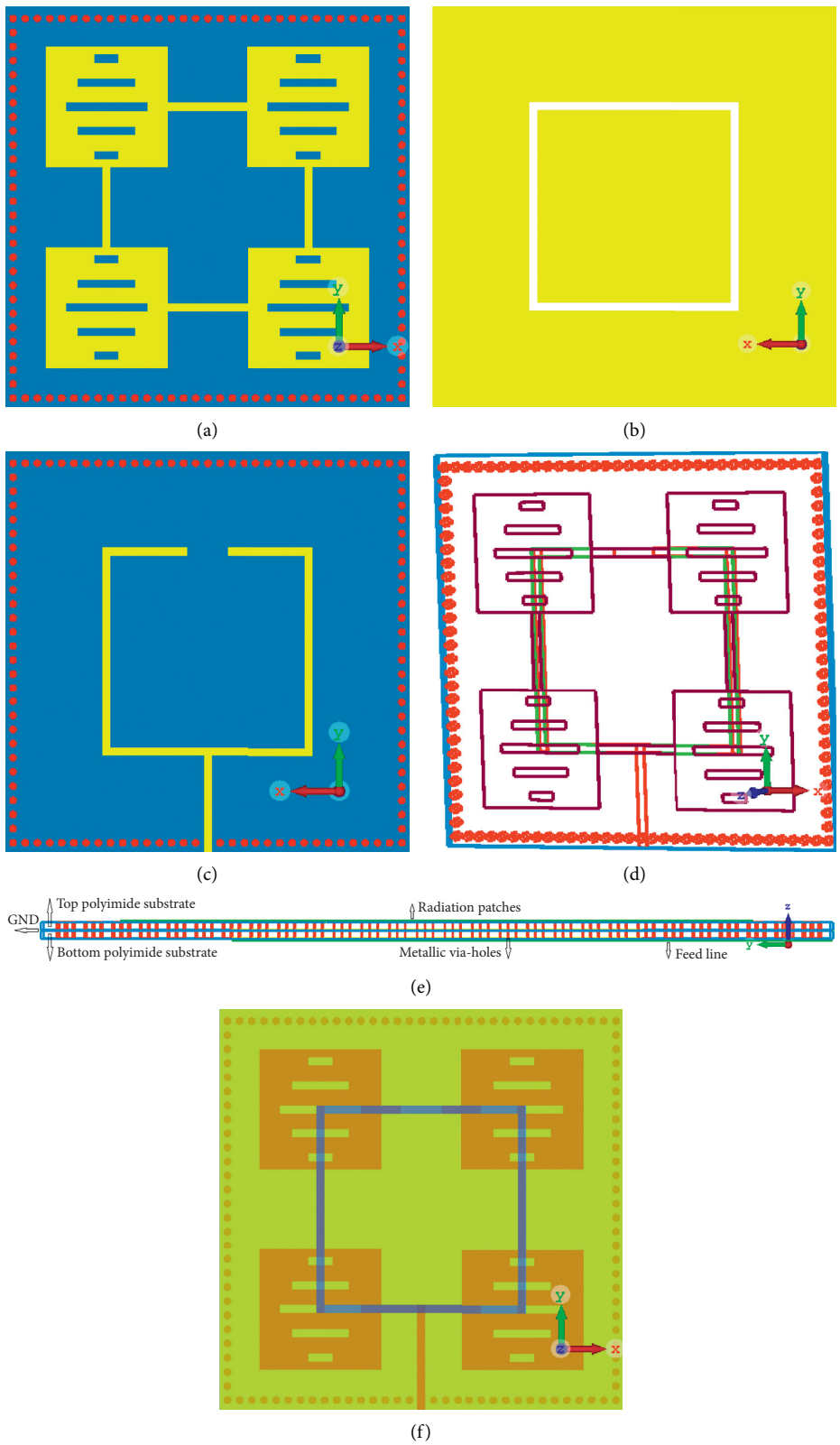

Figure 1: SIW- and MTM-based on-chip antenna configuration. (a) Top view, (b) middle GND, (c) back view, (d) schematic view, (e) side view, and (f) overall view to show all components realized on the top, middle, and bottom layers.

polyimide layers to each other, as shown in Figure 1(e). This technique has been applied to the antenna structure with keeping constant physical dimensions. Figure 1(e) exhibits a side view of the five layers stacked on-chip antenna, on which all layers are connected to each other by the metallic via-hole-inspired SIW content. The reductions in the substrate losses and surface waves will cause to improve the performance parameters such as impedance matching, frequency bandwidth, gain, and radiation efficiency. Figure 1(f) displays the GND layer with its coupling slot which is sandwiched between the top- and bottom-polyimide substrates along with an overall view of the antenna structure showing all structural parameters such as radiation patches on the top-polyimide substrate, the microstrip lines connecting the patches to each others, the microstrip feed line on the bottom-polyimide layer, and metallic via-holes throughout the GND layers connecting both polyimide substrates to each other.

As shown in Figure 1, besides the SIW approach, the metamaterial (MTM) concept has been employed to the radiation patches to achieve more improvements on the performance parameters of the on-chip antenna, without extending its physical dimensions. In this method, the tapered slots have been engraved on the top surface of the square patches. Five linear slots have been etched on each patch which has expanded the effective aperture area of the patches without increasing their physical sizes, which will lead to increase in the radiation properties and extend in the frequency band.

The overall dimensions of the proposed on-chip antenna-inspired SIW and MTM properties is $1000 \times 1000 \times 100\,\mu m^3$, so its structural parameters have been listed in Table 1. It is worth to comment that the proposed antenna has been modeled, tooled, and designed by the two 3D full-wave electromagnetic software of CST Microwave Studio and High-Frequency Structure Simulator (HFSS). To validate the antenna design process, the results achieved from both electromagnetic software have been presented and compared in Table 1, which show an excellent coherence with each other.

The reflection coefficient responses (S_{11}<-15 dB) of the proposed on-chip antenna based on the SIW and MTM approaches are plotted in Figure 2. To validate the results, Figure 2 shows the frequency bandwidths achieved from both CST and HFSS 3D full-wave EM simulators. It is shown that the on-chip antenna can cover the frequency band from 0.600 THz to 0.622 THz, which is corresponding to a wide bandwidth of 22 GHz and a fractional bandwidth of 3.6%. Besides the impedance bandwidth, it is obvious that the proposed antenna applying SIW and MTM concepts shows an average impedance matching better than 25 dB across the entire frequency band. The S-parameter responses achieved from both EM simulators are listed in Table 2. It is shown that both CST and HFSS results have excellent agreement with each other, which confirm the effectiveness of the proposed approaches.

Besides the frequency bandwidth, the radiation specifications are other important parameters to design antenna structures. Figures 3 and 4 depict the radiation gain and efficiency curves over the operating frequency bandwidth. As it is shown in Figure 3, the radiation gains achieved by CST and HFSS software vary from 1.1 dBi to 1.8 dBi throughout the operating frequency band. The results from both simulators are summarized in Table 3. It is exhibited that there is an excellent coherence between both CST and HFSS curves.

Figure 4 shows the radiation efficiency curves obtained by the CST and HFSS simulators over the frequency band. Both curves exhibit that the radiation efficiency changes from 58% to 60.5%. The results from both simulators are presented in Table 4. There is a good agreement between the CST and HFSS results.

The radiation patterns of the proposed on-antenna in the *xy*- and *xz*-planes at 0.60 THz, 0.61 THz, and 0.62 THz are shown in Figure 5. The antenna's radiation energy is mainly focused in the *x*-direction. The beamwidth is narrower in the *xy*-plane. The radiation pattern is stable and symmetrical within the operating band of the antenna.

3. Comparison Section

In this section, the proposed on-chip antenna has been compared with other published papers available in the literature in terms of proposed approaches, dimensions, frequency band, gain, and radiation efficiency. The results are listed in Table 5. It is obvious that the proposed on-chip antenna with a compact dimension is operating over a much higher frequency band exhibiting comparable radiation gain and efficiency in comparison with other cited works in Table 5.

Therefore, the results confirm that the proposed on-chip antenna based on the MTM and SIW concepts with compact dimensions of $1 \times 1 \times 0.1\,mm^3$ operating over 0.600 THz to 0.622 THz with the average gain and radiation efficiency of 1.5 dBi and 60% can be good candidate for integration to utilize in THz circuits. Other advantages of the proposed antenna are its low profile, simple design, easy fabrication process, and low cost, which make it applicable for mass production.

Table 1: Structural parameters of the proposed on-chip antenna-inspired SIW and MTM properties.

On-chip antenna dimensions	$1000 \times 1000 \times 100\,\mu m^3$
Ground plane	$1000 \times 1000\,\mu m^2$
Radiation patches dimensions	$300 \times 300\,\mu m^2$
Polyimide substrates thickness	$50\,\mu m$
Length variations of the slots etched on the patches	$60\,\mu m \leq L \leq 200\,\mu m$
Width of the slots etched on the patches	$20\,\mu m$
Length of the lines connecting the patches	$200\,\mu m$
Width of the lines connecting the patches	$20\,\mu m$
Radius of the metallic via-holes	$10\,\mu m$
Distance between the metallic via-holes	$5\,\mu m$
Length of each side of the square slot etched on the ground plane	$520\,\mu m$
Width of the square slot etched on the ground plane	$20\,\mu m$
Width of the feed line	$20\,\mu m$

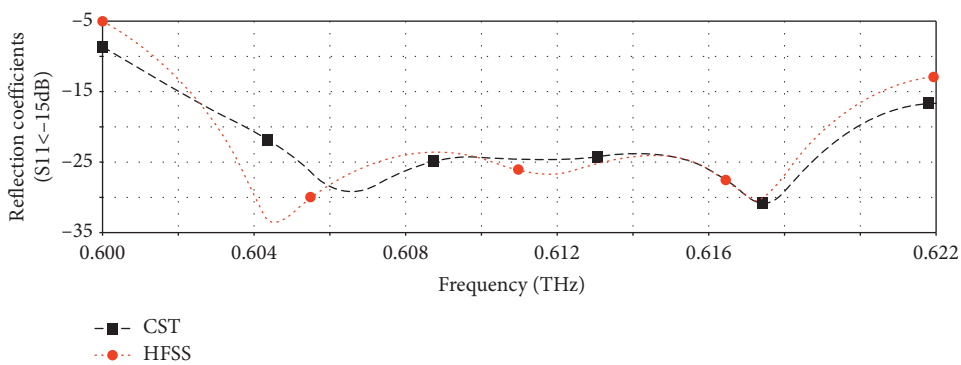

Figure 2: Reflection coefficient responses (S_{11}<-15 dB) achieved by the CST and HFSS EM simulators.

Table 2: S-parameter responses of the proposed antenna.

CST microwave studio	
Frequency band	0.6–0.622 THz
Bandwidth	22 GHz
Fractional bandwidth	3.6%
Resonance frequencies	$f_{r1} = 606.5$ GHz and $f_{r2} = 617.5$ GHz
Impedance matching	25 dB
HFSS	
Frequency band	0.601–0.622 THz
Bandwidth	21 GHz
Fractional bandwidth	3.43%
Resonance frequencies	$f_{r1} = 605$ GHz and $f_{r2} = 617.3$ GHz
Impedance matching	25 dB

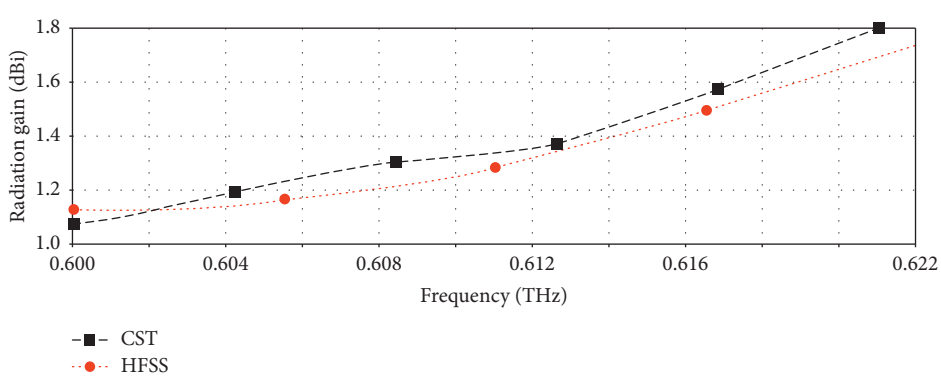

Figure 3: Radiation gain curves over the operating frequency band analyzed by the CST and HFSS EM simulators.

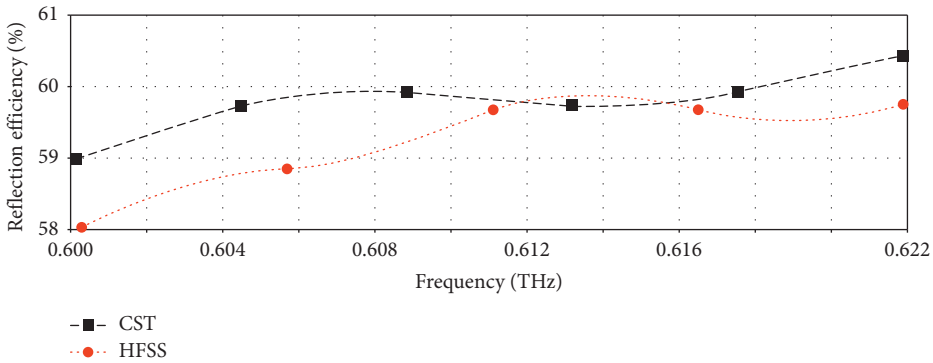

Figure 4: Radiation efficiency curves over the operating frequency band analyzed by the CST and HFSS EM simulators.

Table 3: Radiation gain specifications of the proposed antenna.

CST microwave studio	
Minimum gain	1.1 dBi
Maximum gain	1.8 dBi
Average gain	1.4 dBi
HFSS	
Minimum gain	1.14 dBi
Maximum gain	1.75 dBi
Average gain	1.35 dBi

Table 4: Radiation efficiency specifications of the proposed antenna.

CST microwave studio	
Minimum gain	59%
Maximum gain	60.4%
Average gain	59.8%
HFSS	
Minimum gain	58.3%
Maximum gain	59.9%
Average gain	59.2%

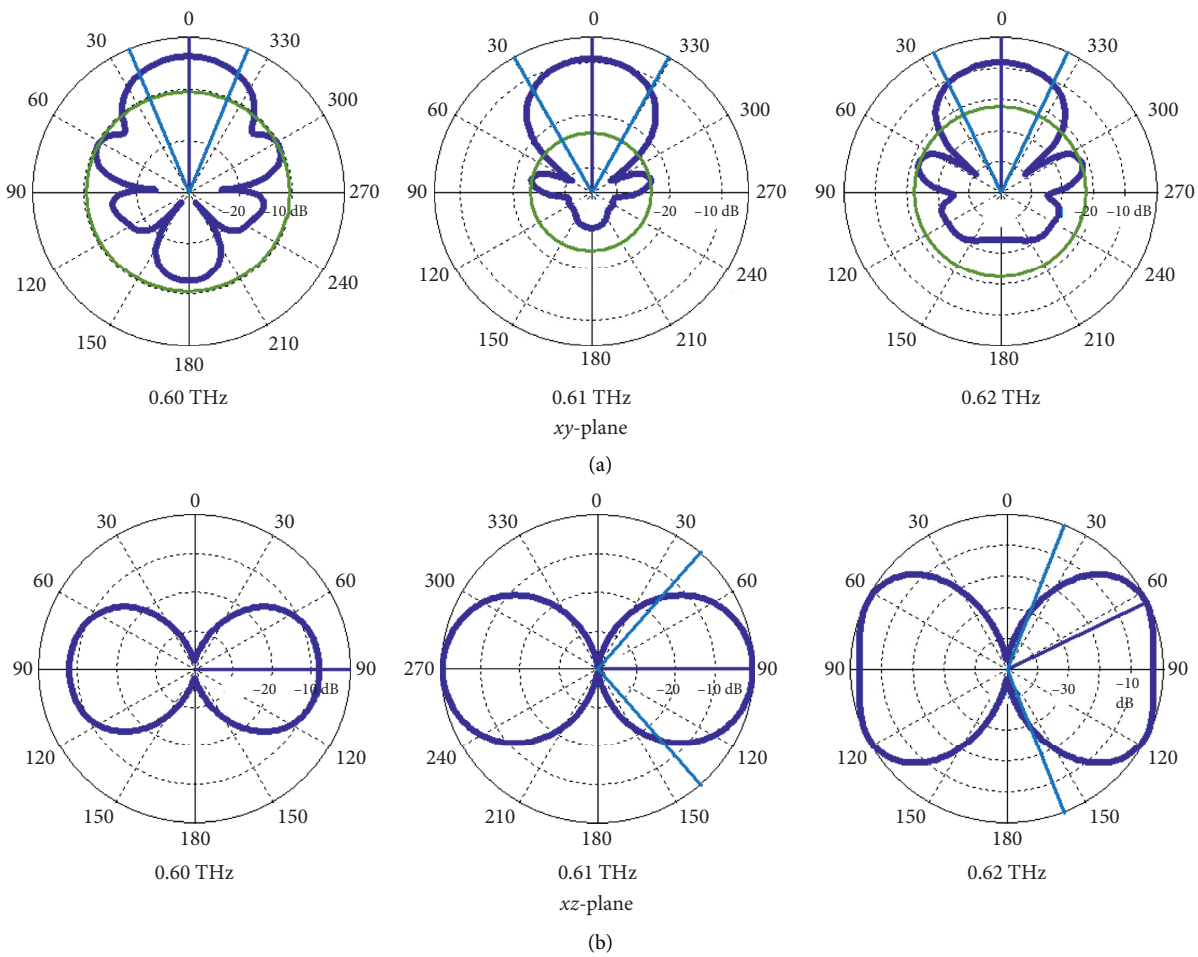

Figure 5: Radiation patterns (normalized) of the antenna in the *xy*-plane and *xz*-plane at spot frequencies of 0.60 THz, 0.61 THz, and 0.62 THz. (a) *xy*-plane (0.60 THz, 0.61 THz, and 0.62 THz). (b) *xz*-plane (0.60 THz, 0.61 THz, and 0.62 THz).

Table 5: State-of-the-art comparison.

References	Antenna type	Bandwidth (GHz)	Gain (dBi)	Efficiency (%)	Size (mm^3) or (mm^2)
[4]-a	OSAR antenna	317–330	1.4	41	0.5×0.5
[4]-b	1×2 antenna	303–320	4.1	38	0.5×1
[17]	Bowtie slot	90–105	≤−1.78	-	0.71 × 0.31 × 0.65
[18]	Differential-fed circularly polarized	50–70	≤−3.2	-	1.5 × 1.5 × 0.3
[19]	Ring-shaped monopole	50–70	≤0.02	≤35	-
[20]	Circular open loop	57–67	≤−4.4	-	1.8 × 1.8 × 0.3
[21]	AMC-embedded squared slot antenna	15–66	≤ 2	-	1.44 × 1.1
[22]	Monopole	45–70	≤4.96	-	1.9 × 1.9 × 0.25
[23]	Loop antenna	65–69	≤8	≤96	0.7 × 1.25
[24]	Dipole antenna	95–102	≤4.8	-	-
[25]	Tab monopole	45–75	≤0.1	≤42	1.5 × 1
[26]	Patch antenna	340 (working frequency)	−5.5	6.5	0.194 × 0.023
[27]	Circular-polarized SIW antenna	251–283	−0.5	21.41	0.99 × 0.99
[28]	SIW slot antenna	410 (working frequency)	−0.5	49.8	0.2 × 0.2
[29]	Dipole loaded AMC	200–281	0	63	0.25 × 0.41
[30]	DRA	340 (working frequency)	10	80	0.7 × 0.7 × 0.73
[31]	2 × 2 slot antenna array	320 (working frequency)	7.9	-	0.86 × 0.86
[32]	2 × 2 cavity-backed rectangular slot loop antenna array	340 (working frequency)	7.7	39	1.1 × 1.1
[33]	2 × 2 DRA array	334–350	8.65	54	1.1 × 1.5 × 1.269
This work	MTM and SIW	600–622	≥1	≥58	1 × 1 × 0.1

4. Conclusion

In this paper, the design process of a 50 μm polyimide layer based on-chip antenna has been proposed and demonstrated, which is working over the higher frequency band of terahertz area from 0.600 THz to 0.622 THz. The proposed structure has been constructed of five stacked layers. It has been excited by a simple coupling feeding mechanism, which is based on the transferring the EM signal from the bottom layer to the top layer throughout the middle GND layer having a coupling slot. To improve the performance parameters of the antenna, the feasible approaches based on the metamaterial (MTM) and substrate-integrated waveguide (SIW) concepts have been employed by realizing the tapered slots on the radiation patches and metallic via-holes on the edges of the structure throughout the GND layer connecting top- and bottom-polyimide substrates to each other, without increasing the physical dimensions of the structure. The proposed on-chip antenna with dimensions of $1000 \times 1000 \times 100\,\mu\text{m}^3$ can operate over a wide frequency range of 0.600 THz to 0.622 THz, which is related to 22 GHz. Across the entire frequency band, the antenna has an average gain and efficiency of 1.5 dBi and 60%, respectively. The results affirm that the proposed antenna with low profile, simple design process, and cost effective can be applicable to use in THz integrated circuits.

Data Availability

The data used to support the findings of this study are available in the manuscript and from the corresponding author upon request.

Conflicts of Interest

The author declares no conflicts of interest.

References

[1] Y. He, Y. Chen, L. Zhang, S.-W. Wong, and Z. N. Chen, "An overview of terahertz antennas," *China Communications*, vol. 17, no. 7, pp. 124–165, 2020.

[2] N. Buadana, S. Jameson, and E. Socher, "A multiport chip-scale dielectric resonator antenna for CMOS THz transmitters," *IEEE Transactions on Microwave Theory and Techniques*, vol. 68, no. 9, pp. 3621–3632, 2020.

[3] M. M. Honari, P. Mousavi, and K. Sarabandi, "Miniaturized-element frequency selective surface metamaterials: a solution to enhance radiation of RFICs," *IEEE Transactions on Antennas and Propagation*, vol. 68, no. 3, pp. 1962–1972, 2020.

[4] H. Zhu, X. Li, Z. Qi, and J. Xiao, "A 320 GHz octagonal shorted annular ring on-chip antenna array," *IEEE Access*, vol. 8, pp. 84282–84289, 2020.

[5] Ozan Dogan Gurbuz, *High-Efficiency On-Chip Antennas for Mm-Wave and THz Frequencies and Tunable RF MEMS Circuits for Wireless Communications*, Ph.D. dissertation, UC San Diego Electronic Theses and Dissertations, San Diego, CA, USA, 2015.

[6] M. Alibakhshikenari, B. S. Virdee, L. Azpilicueta et al., "A comprehensive survey of metamaterial transmission-line based antennas: design, challenges, and applications," *IEEE Access*, vol. 8, pp. 144778–144808, 2020.

[7] E. Limiti, "High-gain on-chip antenna design on silicon layer with aperture excitation for terahertz applications," *IEEE Antennas and Wireless Propagation Letters*, vol. 19, no. 9, pp. 1576–1580, 2020.

[8] H. M. Cheema and A. Shamim, "The last barrier: on-chip antennas," *IEEE Microwave Magazine*, vol. 14, no. 1, pp. 79–91, 2013.

[9] B. S. Virdee, "Study on improvement of the performance parameters of a novel 0.41-0.47 THz on-chip antenna based on metasurface concept realized on 50μm GaAs-layer," *Scientific Reports*, vol. 10, p. 11034, 2020.

[10] A. Mohammad, S. V. Bal, H. S. Chan, R. A. Abd-Alhameed, F. Francisco, and L. Ernesto, "High-ain Metasurface in Polyimide On-hip Antenna Based on CRLH-L for Sub Terahertz Integrated Circuits", Scientific Reports, vol. 10, p. 4298, 2020.

[11] A. Babakhani, X. Guan, A. Komijani, A. Natarajan, and A. Hajimiri, "A 77-ghz phased-array transceiver with on-chip antennas in silicon: receiver and antennas," *IEEE Journal of Solid-State Circuits*, vol. 41, no. 12, pp. 2795–2806, 2006.

[12] J. Edwards and G. Rebeiz, "High-efficiency silicon rfic millimeter-wave elliptical slot-antenna with a quartz lens," in *Proceedings of the IEEE AP-S/URSI International Symposium on Antennas and Propagation*, pp. 899–902, Boston, MA, July 2011.

[13] R. Alhalabi and G. Rebeiz, "Design of high-efficiency millimeter-wave microstrip antennas for silicon rfic applications," in *Proceedings of the IEEE AP-S/URSI International Symposium on Antennas and Propagation*, pp. 2055–2058, Boston, MA, July 2011.

[14] Y.-C. Ou and G. M. Rebeiz, "Differential microstrip and slot-ring antennas for millimeter-wave silicon systems," *IEEE Transactions on Antennas and Propagation*, vol. 60, no. 6, pp. 2611–2619, 2012.

[15] Y. C. Ou and G. M. Rebeiz, "On-chip slot-ring and high-gain horn antennas for millimeter-wave wafer-scale silicon systems," *IEEE Transactions on Microwave Theory and Techniques*, vol. 59, no. 8, pp. 1963–1972, 2011.

[16] J. M. Edwards and G. M. Rebeiz, "High-efficiency elliptical slot antennas with quartz superstrates for silicon rfics," *IEEE Transactions on Antennas and Propagation*, vol. 60, no. 11, pp. 5010–5020, 2012.

[17] M. S. Khan, F. A. Tahir, and H. M. Cheema, "Design of bowtie-slot on-chip antenna backed with E-shaped FSS at 94 GHz," in *Proceedings of the 10th European Conference on Antennas and Propagation (EuCAP)*, Davos, Switzerland, April 2016.

[18] L. Wang and W. Z. Sun, "A 60-GHz differential-fed circularly polarized on-chip antenna based on 0.18-μm COMS technology with AMC structure," in *Proceedings of the IET International Radar Conference*, pp. 1–4, Hangzhou, China, October 2015.

[19] H. T. Huang et al., "A circular ring-shape monopole on-chip antenna with artificial magnetic conductor," *IEEE APMC*, vol. 1-3, 2015.

[20] X.-Y. Bao, Y.-X. Guo, and Y.-Z. Xiong, "60-GHz AMC-based circularly polarized on-chip antenna using standard 0.18-μm CMOS technology," *IEEE Transactions on Antennas and Propagation*, vol. 60, no. 5, pp. 2234–2241, 2012.

[21] F. Lin and B. L. Ooi, "Integrated Millimeter-Wave On-Chip Antenna Design Employing Artificial Magnetic Conductor," in *Proceedings of the IEEE International Symposium on Radio-Frequency*, pp. 174–177, Singapore, 2009.

[22] S. Upadhyay and S. Srivastava, "A 60-GHz on-chip monopole antenna using silicon technology," *IEEE AEMC*, vol. 1-2, 2013.

[23] Y. Song et al., "The design of a high gain on-chip antenna for SoC application," in *Proceedings of the IEEE MTT-S International Microwave Workshop Series on Advanced Materials and Processes for RF and THz Applications (IMWS-AMP)*, Suzhou, China, July 2015.

[24] M. Nafe, "Gain enhancement of low profile on-chip dipole antenna via Artificial Magnetic Conductor at 94 GHz," *IEEE Antennas and Wireless Propagation Letters*, vol. 16, pp. 2844–2847, 2015.

[25] W. Yang, K. Ma, K. S. Yeo, and W. M. Lim, "A 60GHz on-chip antenna in standard CMOS silicon Technology," in *Proceedings of the 2012 IEEE Asia Pacific Conference on Circuits and Systems*, pp. 252–255, Kaohsiung, Taiwan, 2012.

[26] C.-H. Li, C.-L. Ko, M.-C. Kuo, and D.-C. Chang, "A 340-GHz heterodyne receiver front end in 40-nm CMOS for THz biomedical imaging applications," *IEEE Transactions on Terahertz Science and Technology*, vol. 6, no. 4, pp. 625–636, 2016.

[27] Y. Shang, H. Yu, H. Fu, and W. M. Lim, "A 239–281 GHz CMOS receiver with on-chip circular-polarized substrate integrated waveguide antenna for sub-terahertz imaging," *IEEE Transactions on Terahertz Science and Technology*, vol. 4, no. 6, pp. 686–695, 2014.

[28] S. Hu, Y.-Z. Xiong, B. Zhang et al., "A SiGe BiCMOS transmitter/receiver chipset with on-chip SIW antennas for terahertz applications," *IEEE Journal of Solid-State Circuits*, vol. 47, no. 11, pp. 2654–2664, 2012.

[29] M. Nafe, A. Syed, and A. Shamim, "Gain-enhanced on-chip folded dipole antenna utilizing artificial magnetic conductor at 94 GHz," *IEEE Antennas and Wireless Propagation Letters*, vol. 16, pp. 2844–2847, 2017.

[30] X.-D. Deng, Y. Li, C. Liu, W. Wu, and Y.-Z. Xiong, "340 GHz on-chip 3-D antenna with 10 dBi gain and 80% radiation efficiency," *IEEE Transactions on Terahertz Science and Technology*, vol. 5, no. 4, pp. 619–627, 2015.

[31] Z. J. Hou, Y. Yang, X. Zhu, S. Liao, S. K. Man, and Q. Xue, "A 320 GHz on-chip slot antenna array using CBCPW feeding network in 0.13- μm SiGe technology," in *Proceedings of the IEEE MTT-S Int. Microw. Symp. Dig.*, pp. 843–846, Honolulu, Hawaii, USA, June 2017.

[32] X.-D. Deng, Y. Li, W. Wu, and Y.-Z. Xiong, "340-GHz SIW cavity-backed magnetic rectangular slot loop antennas and arrays in silicon technology," *IEEE Transactions on Antennas and Propagation*, vol. 63, no. 12, pp. 5272–5279, 2015.

[33] C.-H. Li and T.-Y. Chiu, "Single flip-chip packaged dielectric resonator antenna for CMOS terahertz antenna array gain enhancement," *IEEE Access*, vol. 7, pp. 7737–7746, 2019.

Hindawi
International Journal of Antennas and Propagation
Volume 2020, Article ID 6478272, 10 pages
https://doi.org/10.1155/2020/6478272

Research Article

Miniature Dual-Band Substrate Integrated Waveguide Slotted Antenna Array for Millimeter-Wave 5G Applications

Fei-Peng Lai, Lu-Wu Chang, and Yen-Sheng Chen

Department of Electronic Engineering, National Taipei University of Technology, Taipei 10608, Taiwan

Correspondence should be addressed to Yen-Sheng Chen; yschen@ntut.edu.tw

Received 28 July 2020; Revised 8 September 2020; Accepted 30 September 2020; Published 12 October 2020

Academic Editor: Diego Caratelli

A compact substrate integrated waveguide (SIW) antenna array that operates at 28 GHz and 38 GHz is proposed for fifth generation (5G) applications. The proposed array consists of four SIW cavities fabricated on one single layer of substrate. Each cavity implements a rhombic slot and a triangular-split-ring slot, resonating on TE_{101} and TE_{102} modes at 28 GHz and 38 GHz, respectively. In comparison with dual-band SIW antennas in the literature, the proposed configuration depicts a miniature footprint ($28.7 \times 30.8\ mm^2$) without stacking substrates. To excite the four cavities with equal power, a broadband power divider that supports the propagation of TE_{10} mode is designed. Accordingly, the impedance bandwidths are 26.6–28.3 GHz and 36.8–38.9 GHz. The measured realized peak gain over the lower and higher bands is 9.3–10.9 dBi and 8.7–12.1 dBi, respectively. The measured half-power beam widths (HPBWs) at 28 GHz and 38 GHz are 20.7° and 15.0°, respectively. Considering these characteristics, including dual bands, high gain, narrow beam widths, miniaturization, and single layer, the proposed antenna array is a suitable candidate for millimeter-wave 5G communication systems with the flexibility in switching operating frequency bands against channel quality variations.

1. Introduction

The millimeter-wave fifth generation (5G) communications have gathered great importance in recent years. As relatively broad bandwidths are available at 28 GHz and 38 GHz, millimeter-wave communications provide higher data capacity. To feed a millimeter-wave antenna, waveguide structures are particularly suitable due to low loss and high power handling capability. However, classical waveguides with solid walls have difficulty to be integrated with printed circuit boards (PCBs). In this situation, substrate integrated waveguide (SIW) feeds can be fabricated with PCBs seamlessly, showing the advantages of low material and fabrication cost, low profile, and excellent shielding properties. Thus, SIW antennas depict great potential for 5G millimeter-wave applications.

Although considerable attention has been paid to the development of 5G millimeter-wave SIW antennas, earlier studies put more emphasis on single-band design at 28 GHz [1–10]. Simultaneous realization of 28-GHz and 38-GHz resonances can reduce the cost and space, but such dual-band designs are relatively lacking [11–14]. The performance of these dual-band SIW antenna arrays is shown in Table 1. Several arrays are implemented through multiple layers of substrates [11–13], which increase the complexity and cost of integration. On the other hand, the single-layer design depicts relatively large dimensions, and the impedance bandwidths are too narrow to cover the 5G specification [14].

The goal of this paper is to present a miniature dual-band SIW slotted array fabricated on one single layer of substrate for millimeter-wave 5G applications. This SIW antenna consists of four cavities arranged as a linear array. The novelty of the proposed antenna array is threefold. First, while SIW slotted arrays have been constructed by conventional thin slots [4, 6–8, 12, 14], square rings [3, 5], quarter-mode resonant cavities [13], triangular-split-ring slots [10], and spoon-shaped slots [9], this study proposes a cavity that consists of new resonant topologies, including a rhombic slot and a triangular-split-ring slot. This new

Table 1: Comparison of dual-band SIW antenna arrays (28/38 GHz).

No.	Number of cavities	Antenna footprint (mm^2)	Multiple layers?	Impedance bandwidths (GHz)
[11]	2×2	105.0×83.7	Yes	24.2–27.8, 36.9–42.8
[12]	2×2	32.0×40.2	Yes	26.3–32.3, 37.4–38.4
[13]	1×4	27.5×28.5	Yes	26.7–30.4, 36.6–38.8
[14]	1×4	40.0×27.5	No	28.0–28.3, 37.3–39.1
This study	1×4	28.7×30.8	No	26.6–28.3, 36.8–38.9

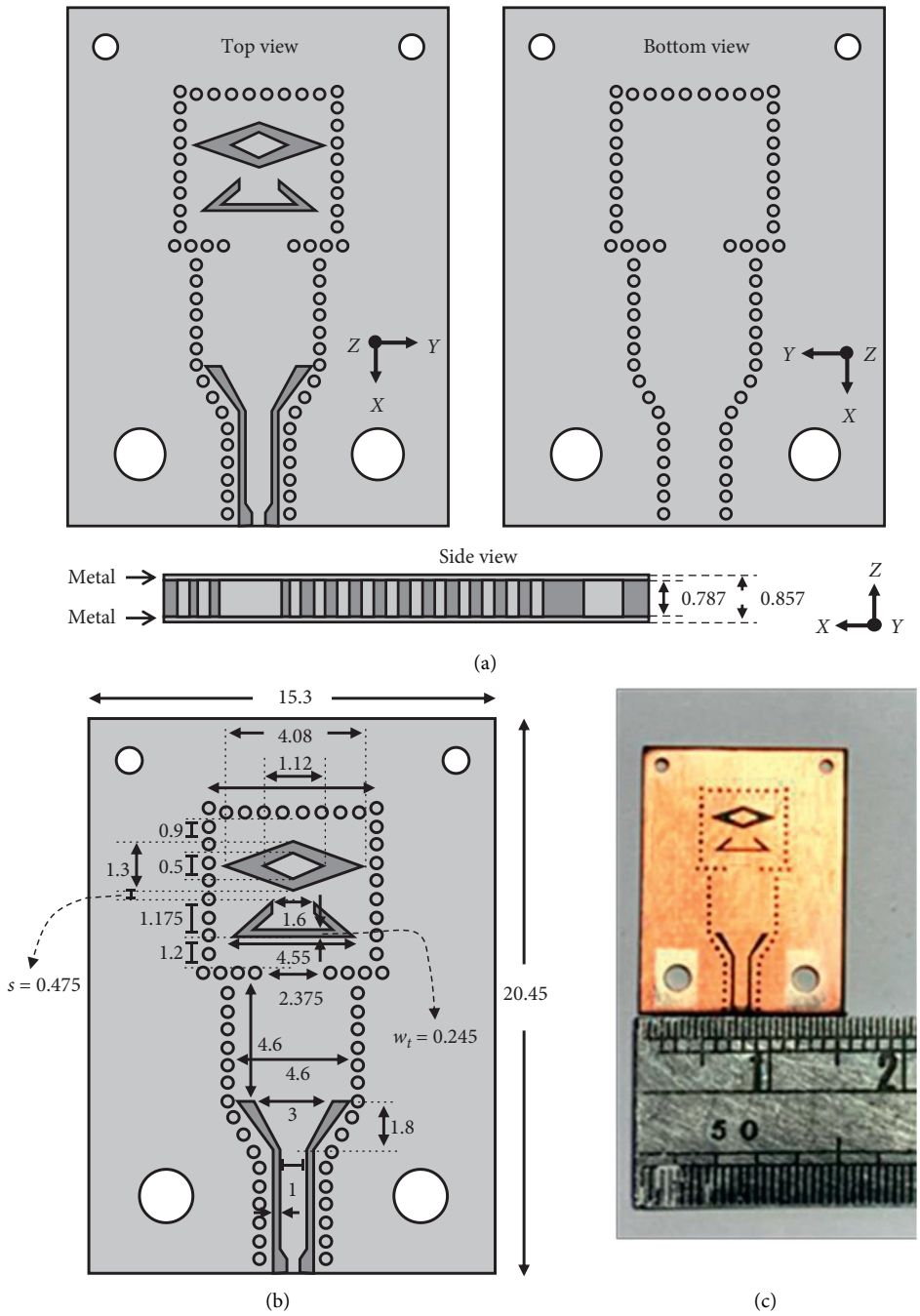

Figure 1: (a) Geometry, (b) detailed dimensions, and (c) photograph of the proposed unit element (unit: mm).

topology miniaturizes the antenna footprint, providing straightforward integration with the microwave electronics of a transceiver. Next, the proposed antenna is a single-layer design, reducing cost and complexity from multilayer PCBs [11–13]. Third, although a miniature and low-profile antenna is developed, the antenna still provides sufficient

impedance bandwidths and high broadside gain. The operating mechanism of the antenna will be explained, and optimized performances supplemented with simulated and measured results will be demonstrated.

2. Unit Element

While the proposed antenna is a 1×4 linear array, this section presents the design and analysis of a unit element. Figure 1 exhibits the geometry and detailed dimensions of the proposed unit element. The antenna is fabricated on one layer of RT/Duroid 5880 substrate (dielectric constant $\varepsilon_r = 2.2$ and loss tangent $\tan\delta = 0.003$). The SIW is fabricated by metallic via arrays, where the separation between adjacent vias is 0.675 mm and the diameter is 0.4 mm. A tapered SIW-to-grounded co-planar waveguide (GCPW) transition is designed to enable dual-band features. The GCPW is terminated with a 50 Ω end launcher, which is utilized to excite the cavity.

The proposed unit element consists of a SIW cavity with a rhombic slot and a triangular-split-ring slot. To explain the principle of dual-band resonances, Figure 2 exhibits the distributions of E-fields simulated using Ansoft HFSS. With the SIW-to-GCPW transition, the TEM mode in the GCPW can be converted into TE_{10} fundamental mode in the SIW. More explicitly, Figure 3 demonstrates the E-field distributions of the cavity at 28 GHz and 38 GHz. The maximum magnitude at 28 GHz is associated with both the resonators. The E-field of the rhombic slot is closely coupled with that of the triangular-split-ring slot, leading to mode bifurcation at the resonant frequency. The cavity resonates on TE_{101} mode. At 38 GHz, the maximum magnitude is majorly radiated through the triangular-split-ring slot, and the cavity resonates on TE_{102} mode.

The operating principle explained above can be validated through parametric studies. Figure 4 indicates that the impedance characteristics at 28 GHz and 38 GHz are affected by the variation of the width of the triangular-split-ring slot, namely, w_t. The larger the w_t, the higher the resonant frequencies are for both the dual bands. In addition, when the separation between the two slots, namely, s, is varied over 0.425 mm, 0.475 mm, and 0.525 mm, the impedance matching at 28 GHz is unaffected. Meanwhile, the resonant frequency at the higher frequency band can be controlled by tuning s; the associated resonant frequencies are 38.8 GHz, 38.6 GHz, and 38.2 GHz, respectively. According to these results, the design rule of the proposed unit element involves two steps. The first step is to tune the geometric parameters to cover the lower frequency band. When the bandwidth requirement of the lower band is met, the second step is to tune the geometric parameters of the triangular-split-ring slot so that the bandwidth of the higher frequency band covers the specification and that of the lower band remains unvaried. These design guidelines offer us a systematic method to obtain the configuration of the rhombic slot and the triangular-split-ring slot. In addition, our parametric studies suggest that the maximum

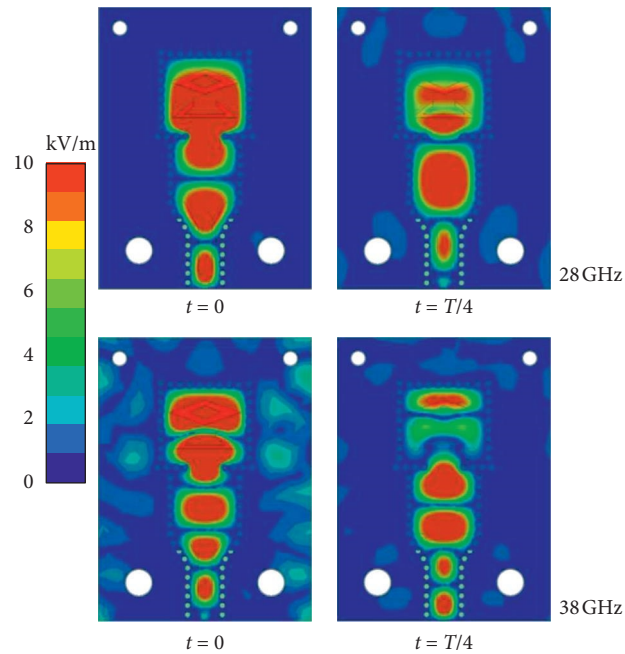

Figure 2: Distributions of the E-field of the proposed unit element.

dimension of the triangular-split-ring slot should be larger than 3.2 mm to cover the lower frequency band. Similarly, the maximum dimension of the rhombic slot should be larger than 4.3 mm to cover the higher frequency band.

The prototype of the proposed unit element is fabricated and tested. The impedance characteristics are tested using a vector network analyzer (VNA) N52227A from Keysight. Figure 5 shows the simulated and measured reflection coefficients. In terms of the −10 dB threshold, the simulated impedance bandwidths are 27.7–28.4 GHz and 37.7–40.1 GHz, whereas the measured ones are 26.7–27.7 GHz and 36.7–38.2 GHz. There are frequency shifts between the simulated and measured results. The discrepancy could be due to the manufacturing errors including the variation of the substrate thickness and the soldering of the end launcher. As the thickness of the substrate increases, the resonant frequency shifts to a lower level. The measured response agrees very well with the antenna designed with a 0.82 mm-height substrate. On the other hand, the model in full-wave simulation does not include the end launcher, which causes differences between the simulated and measured results. The sensitive nature of millimeter-wave cavity and resonator geometry also incurs additional errors.

Figure 6 exhibits the simulated and measured realized peak gain and antenna efficiency. For the lower frequency band, the simulated (measured) realized peak gain is 7.6–8.5 (7.0–8.7) dBi. At the resonant frequency, the simulated and measured antenna efficiencies are 84% and 82%, respectively. For the higher frequency band, the simulated (measured) realized peak gain varies over 7.0–8.0 (3.9–6.8) dBi. At the resonant frequency, the simulated and measured antenna efficiencies are 76% and

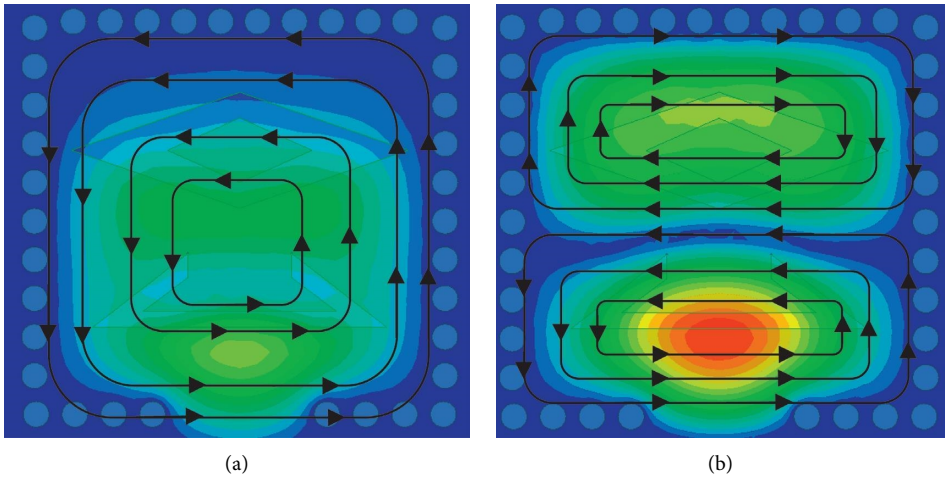

Figure 3: Distributions of the E-field inside the cavity: (a) TE_{101} at 28 GHz and (b) TE_{102} at 38 GHz.

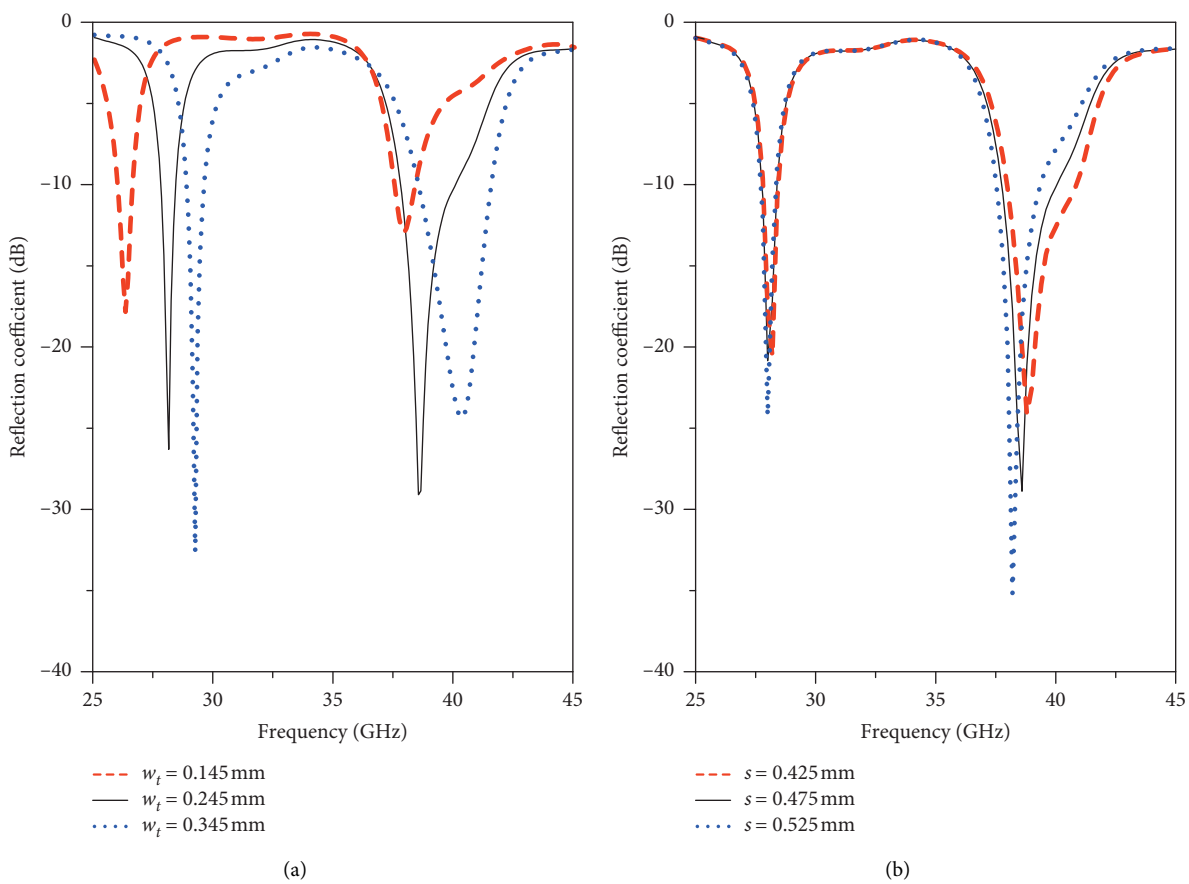

Figure 4: Parametric analysis of the proposed unit element. Effect of the variation of (a) w_t and (b) s.

37%, respectively. The far-field experiments are performed in an anechoic chamber based on compact antenna test range (CATR), as shown in Figure 7. The discrepancy between the simulated efficiency and the measured one is noticeable at the 38 GHz band. This difference is attributed to three issues. First, as will be shown in Figure 8, the pattern of the unit element is not highly directional, and the half-power beam widths (HPBWs) are greater than 70°. Thus, mutual coupling between the AUT and the transmitting horn antenna may occur, reducing the radiation efficiency of the AUT. Second, serrated structures are not implemented in the available CATR anechoic chamber, so diffraction effects may reduce the measurement resolution and the antenna

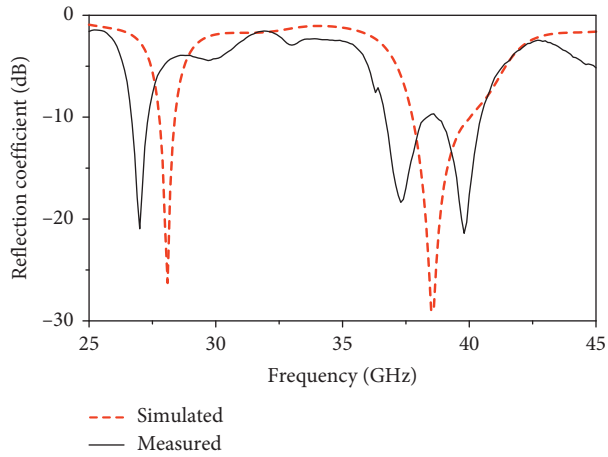

Figure 5: Simulated and measured reflection coefficients of the proposed unit element.

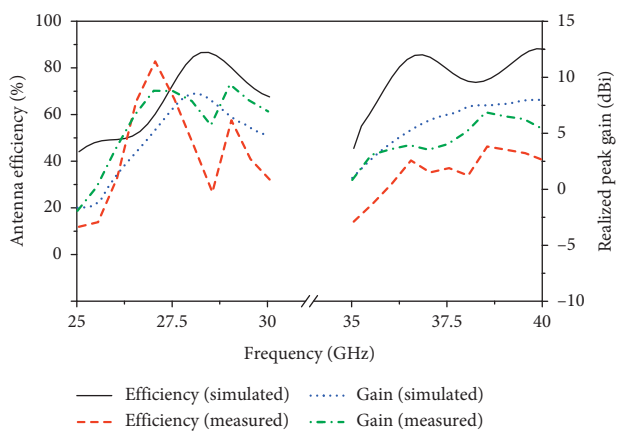

Figure 6: Antenna efficiency and realized peak gain of the proposed unit element.

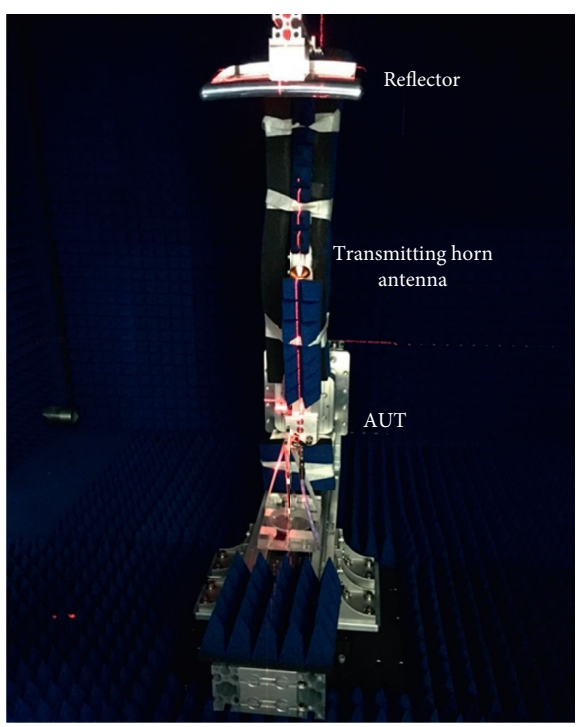

Figure 7: Far-field measurement setup in a compact-range anechoic chamber.

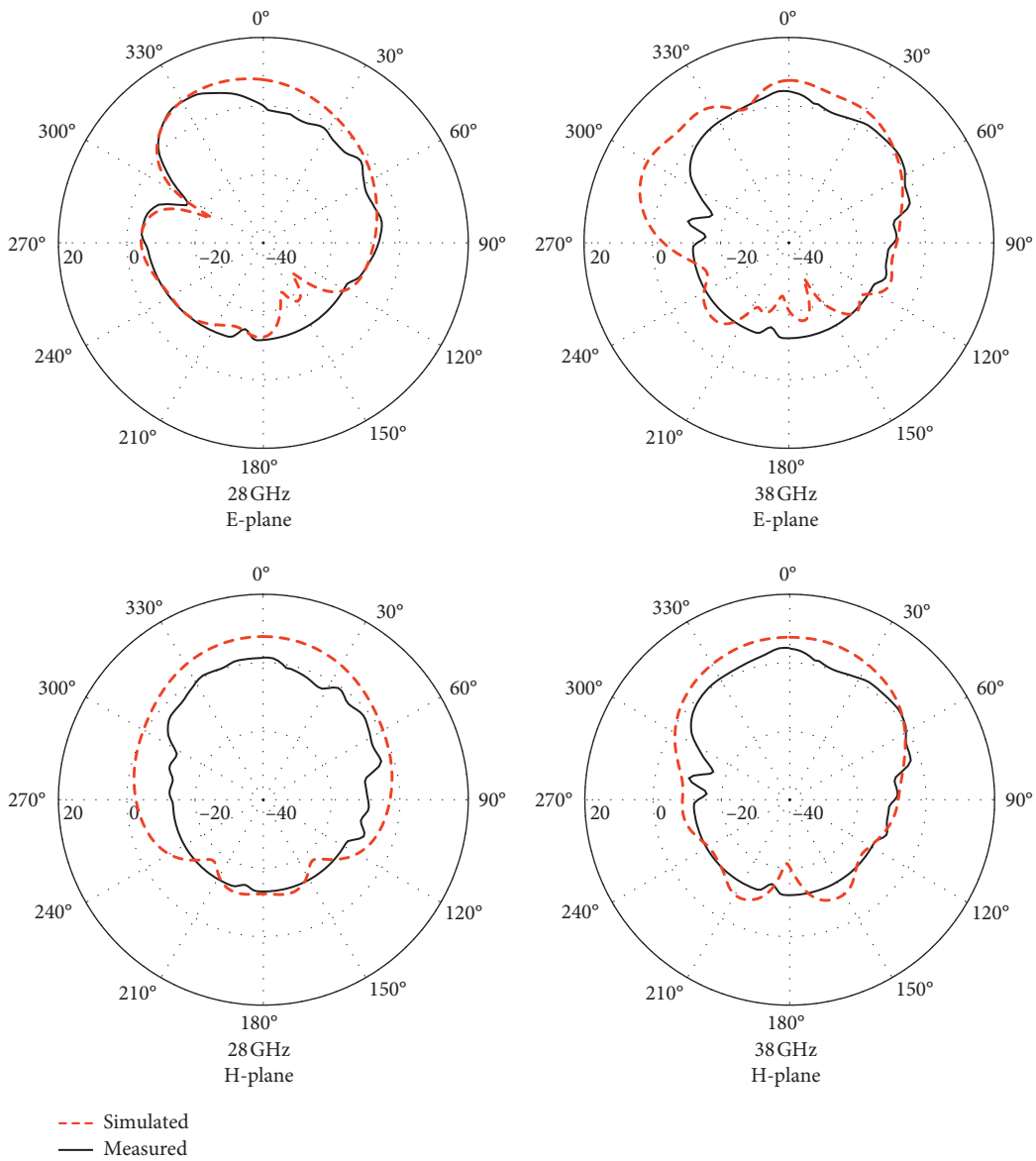

Figure 8: Simulated and measured radiation patterns of the proposed unit element (unit: dBi).

efficiency. Third, the simulated efficiency does not include the loss due to the end launcher, but the imperfect conductivity of the connector may incur additional loss, especially at 38 GHz.

More explicitly, Figure 8 demonstrates the simulated and measured radiation patterns. The main beam is directed at the broadside direction. The simulated (measured) HPBWs at the resonant frequencies of the lower and higher bands are 70.5° (76.0°) and 76.2° (74.7°), respectively. These impedance and radiation characteristics validate the proposed unit element.

3. Antenna Array

After investigating the performance of the unit element, four identical unit elements are integrated as a linear array. Figure 9 exhibits the geometry and detailed dimensions of the proposed 1°×°4 slotted SIW antenna array. The four cavities are cascaded in a shunt-fed manner. All design parameters regarding a single cavity are the same as those described in the previous section.

A broadband power divider is designed to excite the four cavities. The design is created by the duplicate of multiple 2-way dividers. Considering a 2-way power divider, tailoring the vertical segments leads to the equality of output power at each port, and adjusting the spacing between horizontal segments results in an antiphase between adjacent ports. The E-field distributions of the power divider are shown in Figure 10. As compared to the E-field of the unit element, the proposed slotted array still can be excited by the TE_{10} mode. In addition, this power divider avoids multilevel divider configurations, splitting input energy into 4-way output straightforwardly.

For verification, the proposed SIW slotted antenna array is tested in terms of impedance and radiation characteristics.

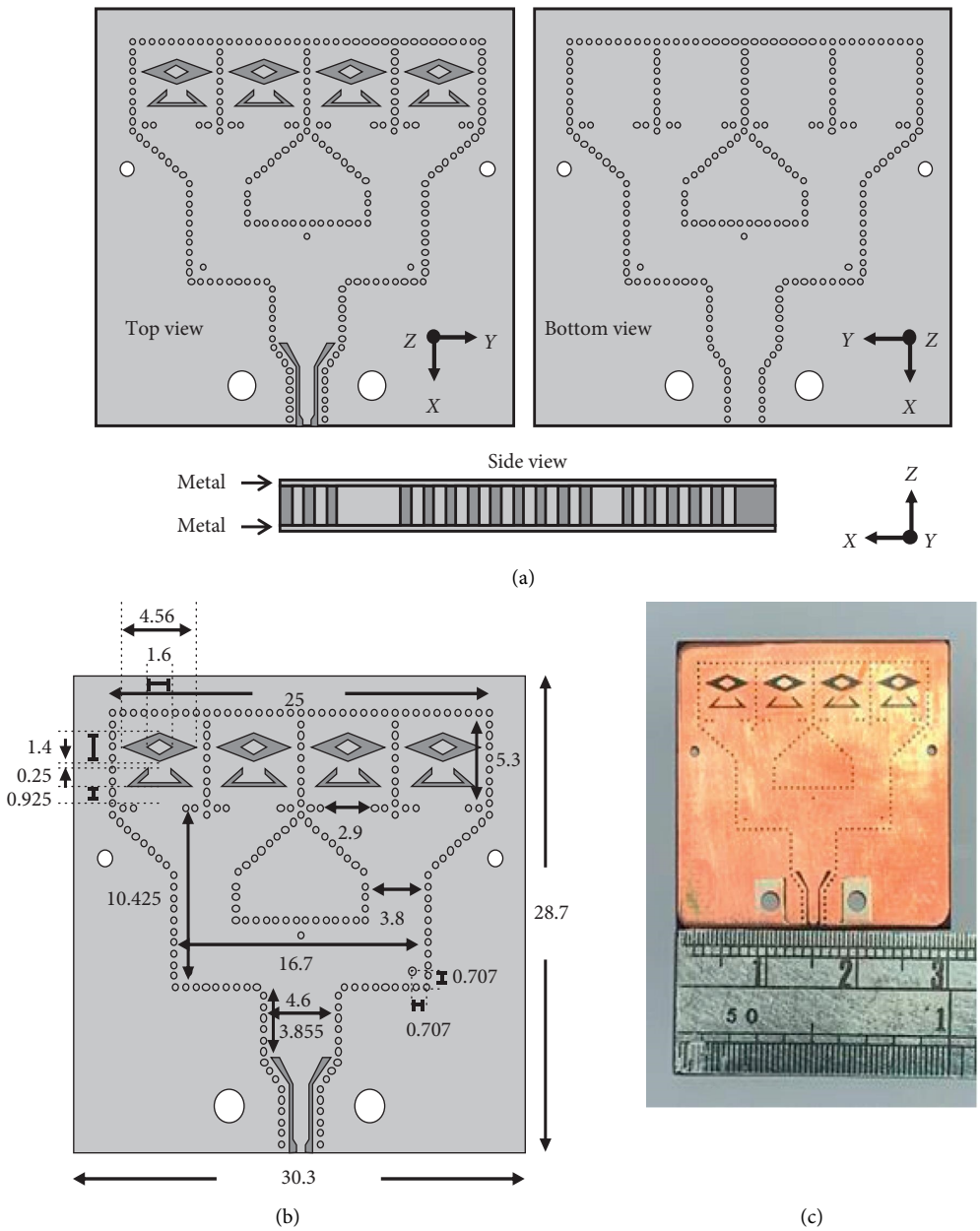

Figure 9: (a) Geometry, (b) detailed dimensions, and (c) photograph of the proposed SIW slotted antenna array (unit: mm).

The simulated (measured) reflection coefficients, provided in Figure 11, indicate that the impedance bandwidths are 26.6–28.4 GHz and 37.8–39.3 GHz (26.6–28.3 GHz and 36.8–38.9 GHz). Minor discrepancies are observed, and they are attributed to the experimental manufacturing techniques. However, both the millimeter-wave 5G frequency bands can be covered by the proposed antenna array.

Figure 12 depicts the realized peak gain and antenna efficiency. The simulated peak gain and measured peak gain over the lower frequency band are 8.5–11.8 dBi and 9.3–10.9 dBi, respectively, whereas the simulated and measured results over the higher frequency band are 13.5–14.3 dBi and 8.7–12.1 dBi. The simulated (measured) antenna efficiency at the resonant frequencies of the lower and higher bands is 66% (45%) and 72% (41%), respectively.

Figure 13 exhibits radiation patterns at 28 GHz and 38 GHz. The broadside gain at 28 GHz and 38 GHz is 9.2 dBi and 8.7 dBi, respectively. In particular, at 28 GHz, the simulated and measured HPBWs on the H-plane are 20.4° and 20.7°, respectively. At 38 GHz, the simulated and measured HPBWs on the H-plane are 15.3° and 15.0°, respectively. Additional studies are performed to investigate the radiation performance of the proposed 1×4 layout and that of a 2×2 series-fed SIW slotted array. The proposed design demonstrates desirable broadside radiation, whereas the 2×2 series-fed layout suffers from the deflation angle of main beams. Since dual-band performance is pursued,

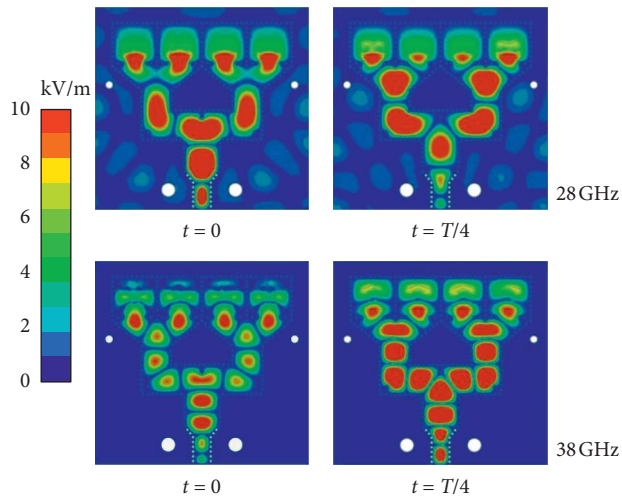

Figure 10: Distributions of the E-field of the proposed antenna array.

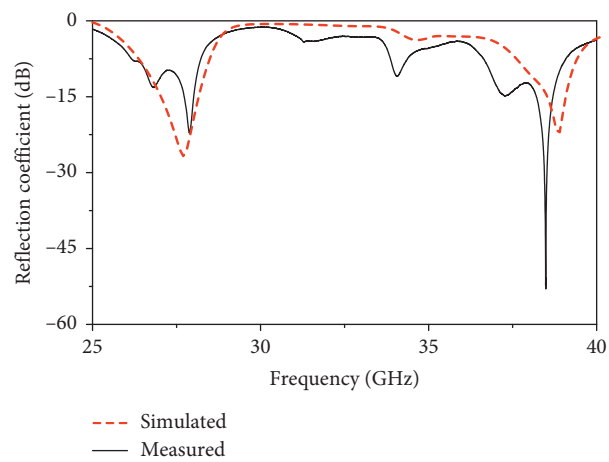

Figure 11: Simulated and measured reflection coefficients of the proposed antenna array.

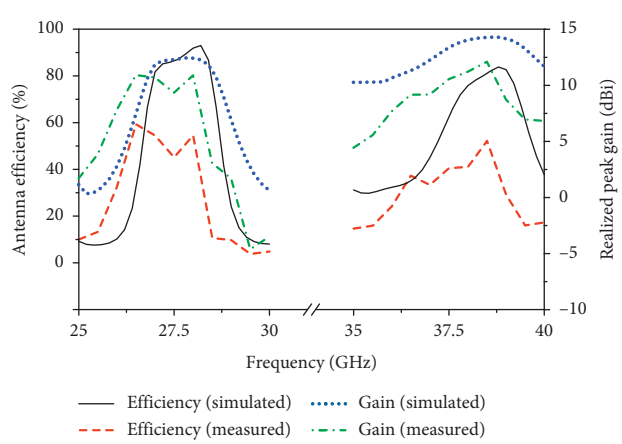

Figure 12: Antenna efficiency and realized peak gain of the proposed antenna array.

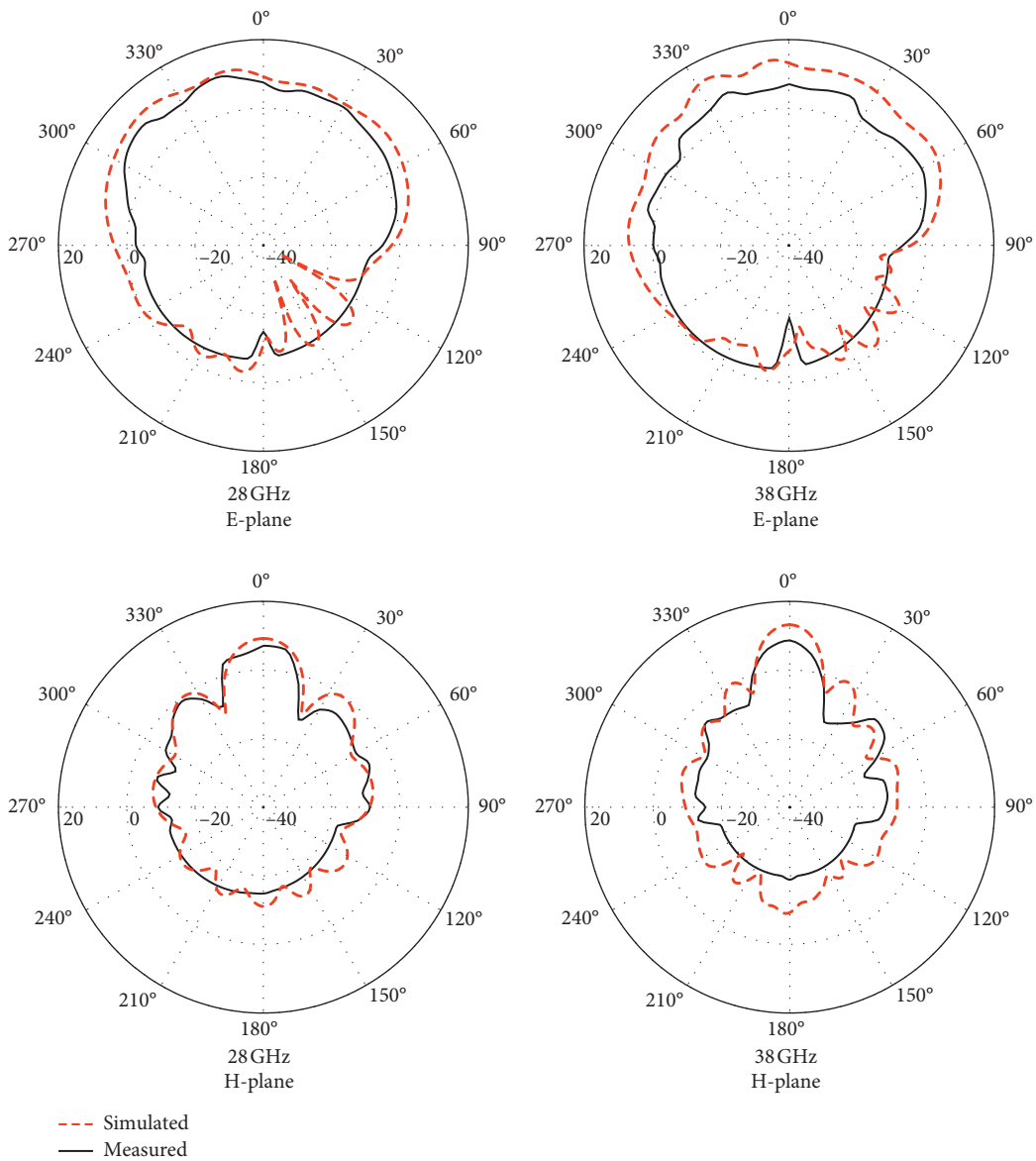

Figure 13: Simulated and measured radiation patterns of the proposed antenna array (unit: dBi).

creating in-phase excitations for longitudinal adjacent elements on both the frequency bands is challenging. These results indicate that the proposed antenna achieves dual-band, high-gain, and narrow-beam features.

4. Conclusion

A dual-band SIW slotted antenna array that implements four cavities comprised of rhombic and triangular-split-ring slots has been presented. The proposed topology has three distinct features. First, the 1×4 antenna array demonstrates a compact footprint ($28.7 \times 30.8\,\text{mm}^2$) with single-layer construction, reducing manufacturing complexity and providing straightforward integration. Second, a systematic design method is developed for the proposed antenna. The resonance at the lower frequency band is generated by the mode bifurcation of the rhombic and triangular-split-ring slots, whereas the higher resonant frequency can be controlled by tuning the triangular-split-ring slot alone. Third, the proposed design not only shows manufacturing simplicity, but it also provides sufficient impedance bandwidths (26.6–28.3 GHz and 36.8–38.9 GHz) and high realized gain (10.9 dBi and 12.1 dBi for the lower and higher frequency bands, respectively). These results make the proposed SIW slotted antenna array a suitable candidate for 5G dual-band communication systems.

Data Availability

The simulated and measured data used to support the findings of this study are included within the article.

Conflicts of Interest

The authors declare that there are no conflicts of interest regarding the publication of this paper.

Acknowledgments

This study was supported in part by the National Taipei University of Technology, Taiwan, under contract NTUT-SZU-109-08 and in part by the Ministry of Science and Technology, Taiwan, under contract MOST 109-2636-E-027-004.

References

[1] K. S. Sultan, H. H. Abdullah, E. A. Abdallah, and H. S. El-Hennawy, "Metasurface-based dual polarized MIMO antenna for 5G smartphones using CMA," *IEEE Access*, vol. 8, pp. 37250–37264, 2020.

[2] N. Al-Fadhali, H. A. Majid, R. Omar, M. K. A. Rahim, S. M. Shah, and B. A. F. Esmail, "Wideband (22–30 GHz) Mm-wave substrate integrated waveguide (SIW) antenna for 5G applications," in *Proceedings of the IEEE Conference on Antenna Measurements & Applications (CAMA)*, pp. 1–4, Kuta, Indonesia, October 2019.

[3] R. Parthasarathy, A. Chandrasekar, and P. G. V Ramesh, "Design of linear 2×2 array using substrate-integrated-waveguide patch antenna for 28 GHz Mm-wave applications," in *Proceedings of the 2019 TEQIP III Sponsored International Conference on Microwave Integrated Circuits, Photonics and Wireless Networks (IMICPW)*, pp. 44–49, Tiruchirappalli, India, May 2019.

[4] R. B. Di Renna, V. P. R. Magri Souza, T. N. Ferreira, L. J. Matos, J. A. M. Souza, and G. L. Siqueira, "A new double-sided substrate-integrated waveguide slot array antenna for 5G applications," *Microwave and Optical Technology Letters*, vol. 61, no. 3, pp. 682–687, 2019.

[5] M. Shirichian, G. Moradi, R. S. Shirazi, and V. Hassanzade, "Design a circularly polarized SIW slot antenna for 5G base stations," in *Proceedings of the 2018 Fifth International Conference on Millimeter-Wave and Terahertz Technologies (MMWaTT)*, pp. 82–85, Tehran, Iran, December 2018.

[6] P. Jing, B. Li, B. Wu, N. Zhang, Y. Xu, and X. Lv, "A millimeterwave SIW slot antenna array for 5G communication," in *Proceedings of the 2018 International Conference on Microwave and Millimeter Wave Technology (ICMMT)*, pp. 1–3, Chengdu, China,, May 2018.

[7] S. Ho-Quang, S. X. Ta, P. Huynh-Nguyen-Bao, K. Nguyen-Khac, and C. Dao-Ngoc, "Compact circularly polarized slotted SIW cavity antenna for 5G application," in *Proceedings of the 2017 International Conference on Advanced Technologies for Communications (ATC)*, pp. 75–79, Quy Nhon, Vietnam, October 2017.

[8] M. Asaadi and A. Sebak, "High-gain low-profile circularly polarized slotted SIW cavity antenna for MMW applications," *IEEE Antennas and Wireless Propagation Letters*, vol. 16, pp. 752–755, 2016.

[9] Q. Wu, H. Wang, C. Yu, and W. Hong, "Low-profile circularly polarized cavity-backed antennas using SIW techniques," *IEEE Transactions on Antennas and Propagation*, vol. 64, no. 7, pp. 2832–2839, 2016.

[10] P. N. Choubey, W. Hong, Z.-C. Hao, P. Chen, T.-V. Duong, and J. Mei, "A wideband dual-mode SIW cavity-backed triangular-complimentary-split-ring-slot (TCSRS) antenna," *IEEE Transactions on Antennas and Propagation*, vol. 64, no. 6, pp. 2541–2545, 2016.

[11] B. Feng, X. He, J.-C. Cheng, and C.-Y.-D. Sim, "Dual-wideband dual-polarized metasurface antenna array for the 5G millimeter wave communications based on characteristic mode theory," *IEEE Access*, vol. 8, pp. 21589–21601, 2020.

[12] T. Hong, Z. Zhao, W. Jiang, S. Xia, Y. Liu, and S. Gong, "Dual-band SIW cavity-backed slot array using TM020 and TM120 modes for 5G applications," *IEEE Transactions on Antennas and Propagation*, vol. 67, no. 5, pp. 3490–3495, 2019.

[13] T. Deckmyn, M. Cauwe, D. Vande Ginste, H. Rogier, and S. Agneessens, "Dual-band (28, 38) GHz coupled quarter-mode substrate-integrated waveguide antenna array for next-generation wireless systems," *IEEE Transactions on Antennas and Propagation*, vol. 67, no. 4, pp. 2405–2412, 2019.

[14] N. Ashraf, O. Haraz, M. A. Ashraf, and S. Alshebeili, "28/38-GHz dualband millimeter wave SIW array antenna with EBG structures for 5G applications," in *Proceedings of the Information and Communication Technology Research (ICTRC)*, pp. 5–8, Abu Dhabi, United Arab Emirates, May 2015.

Hindawi
International Journal of Antennas and Propagation
Volume 2020, Article ID 5495846, 7 pages
https://doi.org/10.1155/2020/5495846

Research Article

Synthesis of Uniformly Excited Concentric Ring Arrays by the Strategy of Partial Density Tapering and the Algorithm of Differential Evolution

Xin-Kuan Wang, Gui-Bao Wang, Jianke Jia, and Chao-Jun Huang

School of Physics and Telecommunication Engineering, Shaanxi University of Technology, Hanzhong 723001, China

Correspondence should be addressed to Xin-Kuan Wang; wxkuan@snut.edu.cn

Received 21 July 2020; Revised 10 September 2020; Accepted 29 September 2020; Published 10 October 2020

Academic Editor: Luciano Mescia

A new strategy of density tapering called the partial density tapering (PDT) accompanied with the algorithm of differential evolution (DE) is proposed to suppress the peak sidelobe level (PSL) of uniform excited concentric ring arrays (UECRA) with isotropic elements. Through performing the PDT, a sound starting solution for DE can be generated. Then, the ring filling factor (RFF) is introduced so that the optimization of the number of elements can be transformed into the optimization of RFFs within the tapered thresholds, and thereby the real coding can be directly used with respect to the consideration of parallel encoding strategy. Finally, the UECRA featuring improved PSL performance can be obtained by limited runs of conventional DE. Several numerical instances for UECRA, with aperture sizes ranging from small to large scale, confirmed the outperformance of the proposed method.

1. Introduction

For the capability of achieving rotationally symmetrical beam pattern, concentric ring array (CRA) had found the applications in radar, direction finding, radio-astronomy, satellite communications, and so on [1–3]. Therefore, the synthesis for CRA had been a topic of considerable study by many investigators [1–17]. In particular, most of the previous efforts focused on the uniform excited (equal feed) CRA due to the simplified feeding network and maximized efficiency of DC-to-RF power conversion, as it is compared to the use of amplitude tapering technique. According to the literatures, we can retrieve mainly three types of methods which are developed to design concentric ring arrays (CRAs). The first is deterministic approaches (DAs) [3–9], which usually refer to emulating the continuous reference aperture distribution where a proper rule of density tapering [4–7] is employed to determine the element locations. In the past few years, several new forms of DAs are proposed to design UECRA. Angeletti et al. [3] presented a method where both locations and dimensions of the radiating elements are jointly optimized to improve the aperture efficiency of UECRA. In literature [8], Morabito and Nicolaci described a way to the optimal power synthesis of mask-constrained shaped beams. In literature [9], by utilizing the characteristics of first kind Bessel functions for representing the array factor, Kedar presented a technique for synthesis of wideband wide-scan UECRA with low sidelobe level. In all, the DAs have a fast calculation speed, which could be used for the synthesis of very large UECRA. However, this type of approaches cannot guarantee the methods which converge to the global optima.

The second type of method is the use of biologically inspired global optimization procedures such as the genetic algorithm (GA) [10] and its improved forms [11–13]. Haupt [10] earlier described the way to optimize the element placement in a UECRA to obtain the low PSL by using the GA. Then, Chen et al. [11] presented a modified real GA (MGA) which makes ring radii as the only optimal variables to suppress the PSL of UECRA. For the same issue, Jiang

et al. [12] proposed an improved integer genetic algorithm (IIGA). In literature [13], a multiobjective GA (MOGA) is described and proved to be effective for designing the CRA, where both the half-power-beamwidth (HPBW) and PSL of the CRAs at different scanning directions are optimized.

The third type of approaches for designing UECRA is the hybrid algorithms (HAs) [2, 14–17]. By combining the advantages of some traditional optimization strategies, the deterministic procedures, the global optimization tools, etc., the use of this type of methods may achieve global optimization at a relative low-computational burden. Some typical contributions are reviewed below. Carlin et al. [2] delivered a two-step methodology which determines the sparsest auxiliary layout of concentric current rings matching a user-defined reference pattern through a Bayesian compressive sensing method and then yields the concentric ring isophoric array by strategy of density tapering. Furthermore, through splitting the synthesis of circular array into a global optimization procedure on a strongly reduced search space and a convex programming problem, Bucci and Pinchera [14] presented a hybrid approach which is proved effective for the synthesis of high-directivity pencil beam patterns. Other notable HAs such as the method in [15] which combines a convex optimization and a determined approach together, the strategy [16] by using weighting density tapering and GA, the approach [17] integrating an improved discrete cuckoo search algorithm (IDCSA), and a cuckoo search-invasive weed algorithm (CSIWA) [17].

Of all the previous efforts, the biological-based methods such as GA [10–12] and MOGA [13] have the advantages of global optimization, but are only suitable for dealing with small arrays. Actually, the reports for synthesizing UECRA of large scale by a limited runs of GA [10] are proved to be time consuming, and thereby local minima is resulted. The global optima may be obtained by many runs of the method, which means the needing of huge computational efforts. According to the authors' opinion, improving the quality of the initial solution is a reasonable way to speed up the convergence speed of the stochastic algorithms. In view of this point and with the purpose of suppressing the PSL of UECRA with isotropic elements, a new strategy of density tapering, named partial density tapering (PDT), is proposed in this paper. The idea of PDT is derived from the technique of amplitude tapering, typical as the solution when performing Taylor tapering to achieve an ultralow sidelobe array. The amplitudes of element excitations show a tapered distribution from the center of array to the outermost. In particular, for the elements located near the center of the array, the normalized excited amplitudes are almost equal and close to 1. For this reason, we first divide the aperture of UECRA into M concentric rings, where a total of m_0 rings (m_0 is the nearest integer less than or equal to $M/2$) close to the center of the array are set to be equal-spaced, and the interspacings of remaining $(M - m_0)$ rings are set to be sequentially increased from the inside to the outside of the array. Then, we initialize the element distribution of m_0 inner rings to be fully populated, while the ring filling factor (RFF, defined as the ratio of the current number of elements of a ring to the number of elements when the ring is fully populated) of the rest rings are constrained by a proper tapered thresholds. For this reason, we name the strategy as PDT.

After the implementation of PDT, both the ring radii and RFF of the outer $(M - m_0)$ rings are optimized by a conventional algorithm of DE; thus, we call the method PDT-DE. Unlike the IIGA [12] where a parallel encoding strategy is adopted, this method transforms the number of elements on a ring into the value of RFF between (0,1), and thereby real coding can be directly used in the optimization procedure.

The paper is organized as follows. Section 2 describes the formulation of the proposed method. Section 3 provides *a* set of numerical examples to validate the effectiveness of the PDT-DE. Finally, the conclusion of this work is summarized in Section 4.

2. Formulation of the Proposed Method

For a single element at the center, the array factor of a UECRA with isotropic elements can be represented by

$$F(u,v) = 1 + \sum_{m=1}^{M}\sum_{n=1}^{N_m} e^{jkr_m\left(u\cos\phi_{mn}+v\sin\phi_{mn}\right)}, \tag{1}$$

where r_m $(m = 1, 2, \ldots, M)$ is the radius of ring m that consists of N_m isotropic elements. M denotes the total number of rings and k is the wave number. ϕ_{mn} depicts the angular location of element n in ring m, which is expressed by $\phi_{mn} = 2\pi(n-1)/N_m$. $u = \sin\theta\cos\phi$ and $v = \sin\theta\sin\phi$, θ and ϕ are the elevation and azimuth angles in spherical coordinates.

For a given ring, we specify that the minimum arc length interval between adjacent elements is 0.5λ (λ denotes the wavelength). Then, the maximum number of elements that can be filled in ring m (we mean that the ring m is fully populated) is given by

$$N_m^{\max} = \operatorname{int}\left(\frac{2\pi r_m}{0.5\lambda}\right), \quad m = 1, 2, \ldots, M, \tag{2}$$

where $\operatorname{int}(A)$ denotes the function that rounds the value of A to the nearest integer less than or equal to A.

Suppose a UECRA consisting of M rings is synthesized using the PDT-DE within a circular aperture of radius R; thus, the detailed procedures of the proposed method are depicted as follows.

2.1. Aperture Division. Divide the aperture into M concentric rings, where both R and M should conform to the relationship:

$$\begin{cases} \epsilon = R - M\cdot d_0, \\ \text{s.t. } \varepsilon \geq 0.5\lambda, \quad d_0 \in (0.5\lambda, 0.6\lambda), \end{cases} \tag{3}$$

where ϵ is the difference of the radii between aperture radius and the outermost ring when we assume that all the rings are spaced at d_0. For convenience, rewrite d_0 as

$$d_0 = (0.5 + 0.1\sigma)\lambda, \tag{4}$$

where σ is a randomly selected value from interval (0,1). Furthermore, we force $m_0 = \text{int}(M/2)$, and the radii of m_0 rings close to the center of the aperture can be expressed by

$$r_m = m \cdot d_0, \quad m = 1, 2, \ldots, m_0. \tag{5}$$

For the rest $(M - m_0)$ rings located away from the center of the aperture, the radii are specified by

$$\begin{cases} r_{m_0+q} = (m_0 + q) \cdot d_0 + \Delta d_q, \\ \text{s.t. } 0 < \Delta d_q < \epsilon, \quad q = 1, 2, \ldots M - m_0. \end{cases} \tag{6}$$

For convenience, a vector is introduced to describe the collection of $\Delta d_q, \quad q = 1, 2, \ldots, M - m_0$, as

$$\Delta \mathbf{d} = \left\{\Delta d_1, \Delta d_2, \ldots, \Delta d_{M-m_0}\right\}. \tag{7}$$

Let $\Delta r_m = r_m - r_{m-1}$, which means the difference of radii between mth and $(m-1)$th rings; then, we have

$$\begin{cases} \Delta r_m = d_0, \quad \text{for } 2 \le m \le m_0, \\ \Delta r_m > d_0, \quad \text{for } m_0 < m \le M. \end{cases} \tag{8}$$

According to equations (6) and (7) and in order to meet the requirement of density tapering, the variables in vector $\Delta\mathbf{d}$ need to be arranged in ascending order. To determine $\Delta\mathbf{d}$, a new vector is defined as

$$\boldsymbol{\tau} = \left\{\tau_1, \tau_2, \ldots, \tau_{M-m_0}, \tau_{1+M-m_0}, \tau_{2+M-m_0}, \ldots, \tau_{L+M-m_0}\right\}, \tag{9}$$

where L is an integer that is randomly selected from 0 to 5 and $\tau_i \quad (1 \le i \le L + M - m_0)$ is the random number uniformly distributed within (0,1). Through sorting $\{\tau_i\}$ in ascending order, we get a distinct vector:

$$\boldsymbol{\tau}' = \left\{\tau'_1, \tau'_2, \ldots \tau'_{M-m_0}, \tau'_{1+M-m_0}, \tau'_{2+M-m_0}, \ldots, \tau'_{L+M-m_0}\right\}. \tag{10}$$

Based on (3) and (10), we divide ϵ into $(L + M - m_0)$ unequal parts, and the value of each part is described by

$$\delta_i = \frac{\epsilon}{\sum_{i=1}^{M-m_0+L} \tau'_i} \cdot \tau'_i, \quad i = 1, 2, \ldots, L + M - m_0. \tag{11}$$

Let a new vector to record (11) be

$$\boldsymbol{\delta} = \left\{\delta_1, \delta_2, \ldots, \delta_L, \delta_{L+1}, \ldots, \delta_{L+M-m_0}\right\}. \tag{12}$$

Previous derivation shows that $\delta_i \quad (i = 1, 2, \ldots, L + M - m_0)$ increases sequentially with the increment of subscripts. Furthermore, we split δ into two vectors (denoted as δ' and δ'') and record them as

$$\boldsymbol{\delta}' = \{\delta_1, \delta_2, \ldots, \delta_L\}, \tag{13}$$

$$\boldsymbol{\delta}'' = \left\{\delta_{L+1}, \ldots, \delta_{L+M-m_0}\right\}. \tag{14}$$

Let $\Delta\mathbf{d} = \delta''$; therefore, $\Delta d_q = \delta_{L+q} \quad (q = 1, 2, \ldots, M - m_0)$.

After the implementation of equations (3)–(14), all the ring radii of UECRA are determined. For rings from 1th to m_0th, the spacings are equal to d_0. Differently, for rings from $(m_0 + 1)$th to Mth, the ring intervals are greater than d_0, and they are gradually increased from the inside to the outside of the array.

The use of vector δ' is to make a slight adjustment to the radius of outermost ring so that $r_M \le R$. In particular, when $L = 0$, δ' becomes to an empty set; thus, we have $r_M = R$, or else $r_M < R$. The operation helps to meet the design targets under possible smallest aperture radius.

2.2. Initialize the Element Distribution. Firstly, the rings from 1th to m_0th are fully populated, and the number of elements for each ring is determined by (2). The total number of elements in the full structure is recorded as $\sum_{m=1}^{m_0} N_m^{\max}$. For the rest rings, the ring filling factors (RFFs) are expressed by

$$f_q = \frac{N_{m_0+q}}{N_{m_0+q}^{\max}} \times 100\%, \quad q = 1, 2, \ldots, M - m_0, \tag{15}$$

where N_{m_0+q} denotes the current number of elements in ring $m_0 + q$ and $N_{m_0+q}^{\max}$ is determined by (2). We set a new vector to describe (15) as

$$\mathbf{f}_{\text{RFF}} = \left\{f_1, f_2, f_3, \ldots, f_{M-m_0}\right\}, \tag{16}$$

where $f_q \quad (q = 1, 2, \ldots, M - m_0)$ are bounded by

$$f_q^{\min} < f_q < f_q^{\max}, \quad q = 1, 2, \ldots, M - m_0. \tag{17}$$

For convenience, the collections of $\left\{f_q^{\min}\right\}$ and $\left\{f_q^{\max}\right\}$ are, respectively, labeled as

$$\mathbf{f}_{\text{RFF}}^{\min} = \left\{f_1^{\min}, f_2^{\min}, f_3^{\min}, \ldots, f_{M-m_0}^{\min}\right\}, \tag{18}$$

$$\mathbf{f}_{\text{RFF}}^{\max} = \left\{f_1^{\max}, f_2^{\max}, f_3^{\max}, \ldots, f_{M-m_0}^{\max}\right\}. \tag{19}$$

Both $\mathbf{f}_{\text{RFF}}^{\max}$ and $\mathbf{f}_{\text{RFF}}^{\min}$ constitute the upper and lower filling thresholds for $\mathbf{f}_{\text{RFF}}$. In order to meet the requirement of density tapering, the variables of the two vectors should be given in descending order, respectively. In more detail, we set $f_q^{\min} \quad (q = 1, 2, \ldots, M - m_0)$ to be arranged in descending order within the interval [0.25, 0.8], and accordingly $f_q^{\max} \quad (q = 1, 2, \ldots, M - m_0)$ are determined by

$$\begin{cases} f_q^{\max} = f_q^{\min} + \eta_1, \quad \text{when } f_q^{\min} \ge 0.75, \\ f_q^{\max} = f_q^{\min} + \eta_2, \quad \text{otherwise}, \end{cases} \tag{20}$$

where we specify $\eta_1 \in [0.1, 0.2]$, $\eta_2 \in [0.1, 0.25]$ so that the RFFs for rings from $(m_0 + 1)$th to Mth are less than 1.0. Not only that, the curves of RFF thresholds need to have a relatively gentle tapering to expand the solution space and enhance the capability of global convergence of the algorithm. Therefore, a scope $0.05 \le \eta_2 - \eta_1 \le 0.1$ is recommended. However, the parameters of η_1 and η_2 are not strictly limited, as long as the values ensure that the RFFs are less than 1.0 and both the RFF thresholds satisfies a proper tapering distribution.

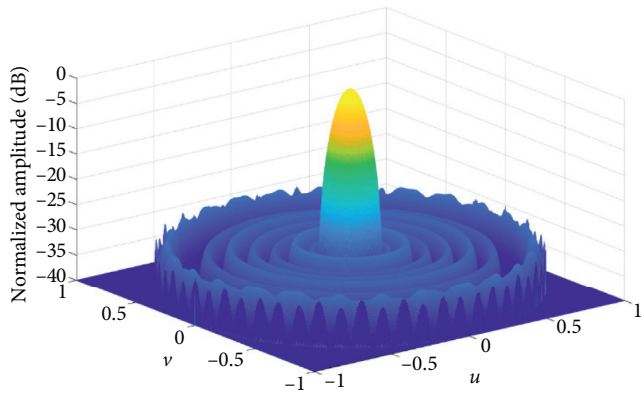

Figure 1: 3D pattern of the UECRA when $N = 142$.

2.3. DE Optimizing. The individual vector of the population is constituted by σ, τ, and $\mathbf{f_{RFF}}$, which can be described as

$$\mathbf{X} = \{\sigma, \boldsymbol{\tau}, \mathbf{f_{RFF}}\}, \tag{21}$$

with

$$\begin{cases} 0 < \sigma < 1, \\ 0 < \tau_i < 1, \quad i = 1, 2, \ldots, L + M - m_0, \\ f_q^{\min} < f_q < f_q^{\max}, \quad q = 1, 2, \ldots, M - m_0. \end{cases} \tag{22}$$

Both σ and τ are used to adjust the ring radii of UECRA, while $\mathbf{f}_{\mathrm{RFF}}$ determines the number of elements that can be filled in different rings. Suppose $\tau_{\max} = \{1, 1, \ldots, 1\}$ and $\tau_{\min} = \{0, 0, \ldots, 0\}$ and both the two vectors have the same length with τ. Correspondingly, the upper and lower thresholds for $\mathbf{X}$ can be expressed by

$$\begin{cases} \mathbf{X}_{\max} = \{0, \boldsymbol{\tau}_{\max}, \mathbf{f}_{\mathrm{RFF}}^{\max}\}, \\ \mathbf{X}_{\min} = \{1, \boldsymbol{\tau}_{\min}, \mathbf{f}_{\mathrm{RFF}}^{\min}\}. \end{cases} \tag{23}$$

According to (23), more individuals of DE are generated through the equation:

$$\mathbf{X} = \mathbf{X}_{\min} + \mathbf{R}_{\mathrm{and}} \cdot (\mathbf{X}_{\max} - \mathbf{X}_{\min}), \tag{24}$$

where $\mathbf{R_{and}}$ is a random vector that has the same length with $\mathbf{X}$, and the variables in $\mathbf{R_{and}}$ are the random numbers uniformly distributed within (0,1). The fitness function are defined as

$$\min \mathrm{PSL} = \zeta(\mathbf{X}), \tag{25}$$

where $\zeta(\mathbf{X})$ denotes the UECRA that can be obtained with minimum PSL (the fitness value). After the whole population is formed, the individuals are optimized by a conventional DE and evaluated by the fitness function described in (25). Simultaneously, the elite strategy is adopted so that the UECRA featuring minimum PSL is retained.

3. Numerical Examples

The proposed method is applied to the design cases similar to that taken from [10–12, 16], where a single element is existed at the center of UECRA. The parameters involved in the method, including the population size, the maximum number of iterations in each generation, and crossover probability, as well as the scaling factor, are equal to 50, 20, 0.9, and 0.8, respectively.

In the first case, a circular aperture with radius of 4.5λ is considered, among which the array consists of 7 rings and 142 elements. According to the proposed method, the inner three rings are fully populated. For the four outer rings, we renumbered them from inside to the outside as 1#, 2#, 3#, and 4#. Theoretically, the upper and lower thresholds for filling factors of the four rings should be prespecified, as are described by (18)–(20). However, since the total number of elements is given in advance, only the RFF thresholds of 1#~3# rings need to be predetermined. The number of elements in the 4# ring is equal to the difference between 141 and the total number of elements included in the remaining six rings. We specify the lower and upper RFF thresholds as [0.8, 0.65, 0.5] and [1.0, 0.9, 0.75], respectively. The obtained array after 50 runs of the PDT-DE has the PSL of −29.95 dB, which is 2.13 dB lower than the value obtained by the GA [10] and 1.62 dB lower than the report obtained by the MGA [11]. Not only that, compared with the report in [10], the aperture radius is reduced from 4.7λ to 4.26λ, and the directivity (denoted as D) is lost by 0.7 dB.

Similarly, when we increase the total number of elements in UECRA to 183 and the number of rings to 8, the PSL of synthesized array is equal to -27.86 dB, which shows a PSL reduction of 2.28 dB with a little sacrifice at directivity, as it is compared to the value demonstrated by GA [10]. Described in Figures 1 and 2 are the 3D pattern of previous two instances, where N denotes the total number of elements. In addition, for the case when $N = 201$, the best array after 50 runs of the PDT-DE has a PSL equal to −30.34 dB. The performance of the array shows a PSL suppression of 1.21 dB compared to the value obtained by the MGA [11] and a PSL suppression of 6.13 dB compared to that demonstrated by the IFT-DE [18]. More detailed results, including the ring radii and the number of elements in each ring, are given in Table 1.

In the fourth case, we consider a circular array with aperture radius of 15λ, and the total number of elements of 1302. Then, we set the maximum number of runs equal to 20 to alleviate the computational burden. The best fitness value

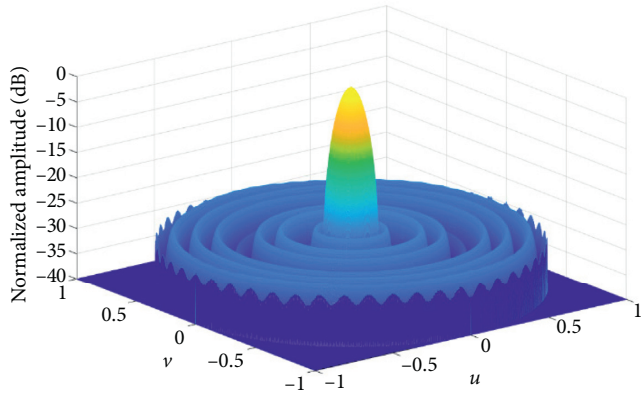

Figure 2: 3D pattern of the UECRA when $N = 183$.

Table 1: Synthesis results obtained by PDT-DE for the cases $N = 142$, 183, and 201.

$R(\lambda)$	N	PSL (dB)	D (dB)	m	1	2	3	4	5	6	7	8
4.26	142	−29.95	28.19	$r_m(\lambda)$	0.5	1.0	1.5	2.06	2.68	3.45	4.26	—
				N_m	6	12	18	21	29	26	29	—
4.5	183	−27.86	28.39	$r_m(\lambda)$	0.5	1.0	1.5	2.0	2.5	3.07	3.68	4.5
				N_m	6	12	18	25	25	28	25	43
5.0	201	−30.34	29.30	$r_m(\lambda)$	0.5	1.0	1.5	2.0	2.65	3.36	4.11	5.0
				N_m	6	12	18	25	33	35	31	40

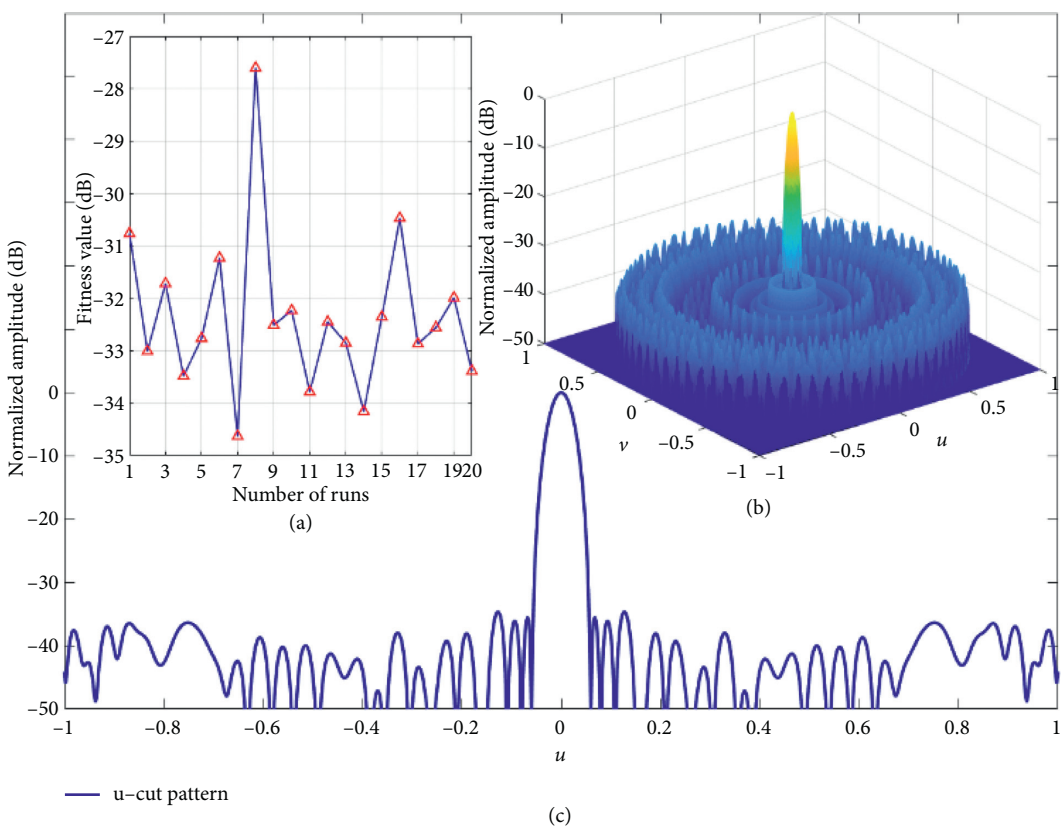

Figure 3: (a) Convergence of fitness value, (b) 3D pattern, and (c) u-cut.

is obtained at the 7th run, where the array has the PSL of −34.63 dB, as shown in Figure 3(a). The value is 1.67 dB lower than the report demonstrated by IIGA [12] with a 0.11 dB loss of directivity. Correspondingly, a reduction of aperture radius about 0.36λ is resulted. Figures 3(b) and 3(c) describe the 3D and u-cut pattern of the array, respectively.

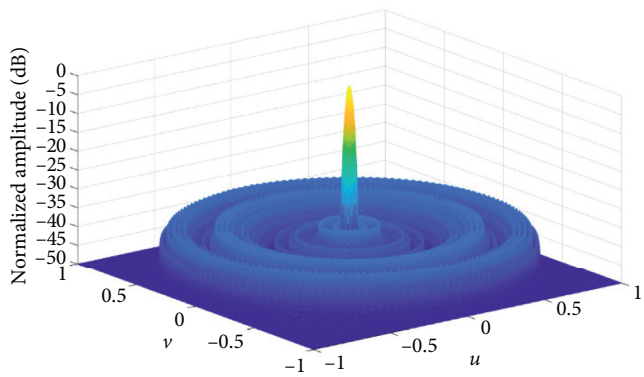

Figure 4: 3D pattern of the UECRA when $N = 2256$.

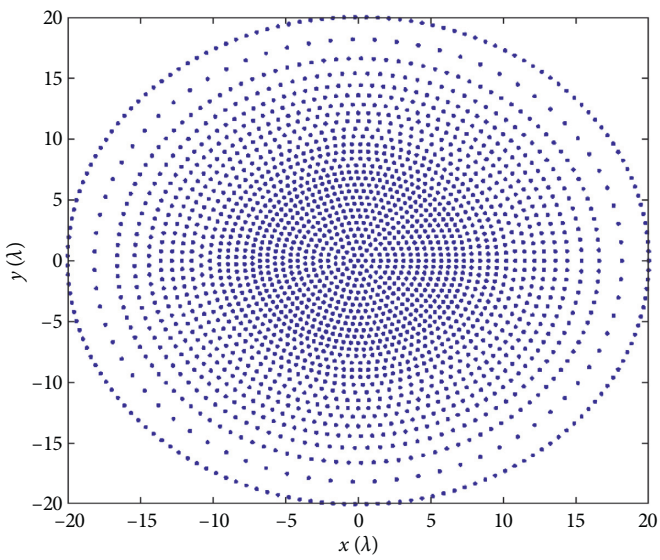

Figure 5: Element distribution of the UECRA when $N = 2256$.

Furthermore, the method is extended for the synthesis of large-scale UECRA within an aperture radius of 20λ, among which the array consist of 2256 elements and 29 rings. The best array by 20 runs of the PDT-DE has the PSL of −36.33 dB and directivity of 39.54 dB, which show about 2.25 dB PSL reduction with only 0.12 dB loss of directivity, as compared to the reports obtained by HS [16].

Figures 4 and 5 depict the 3D pattern and element distribution within the aperture of the UECRA, respectively. For the same array, the ring radii and the number of elements in each ring are tabulated in Table 2. More synthesis results by using different methods are compared in Table 3, where we can conclude that the PDT-DE has the advantages in PSL suppression of UECRA with respect to other methods, and the PSL performance of the array become more impressive for large scale UECRA by using the proposed method. All the numerical results mentioned above are obtained by using a PC equipped with an 8 GB RAM, and the Intel I7-6700 processor that operates at 3.4 GHz.

Table 2: Results of ring radii (r_m) and number of elements (N_m) for the UECRA including 2256 elements.

m	r_m	N_m	m	r_m	N_m	m	r_m	N_m
1	0.52	6	11	5.72	71	21	11.46	96
2	1.04	13	12	6.24	78	22	12.13	108
3	1.56	19	13	6.76	84	23	12.81	106
4	2.08	26	14	7.28	91	24	13.58	112
5	2.60	32	15	7.82	87	25	14.40	117
6	3.12	39	16	8.39	89	26	15.38	111
7	3.64	45	17	8.97	101	27	16.59	121
8	4.16	52	18	9.56	105	28	18.16	75
9	4.68	58	19	10.19	98	29	20.0	163
10	5.20	65	20	10.81	87	—	—	—

Table 3: Comparative results by using different methods.

$R(\lambda)$	N	Methods	PSL (dB)	D (dB)	3dB beamwidth (Δu)
4.70	142	GA [10]	−27.82	28.89	—
4.70		MGA [11]	−28.33	—	—
4.26		PDT-DE	−29.95	28.19	0.128
4.5	183	GA [10]	−25.58	28.5	—
4.5		PDT-DE	−27.86	28.39	0.115
4.98	201	MGA [11]	−29.13	—	—
5.0		IFT-DE [18]	−24.21	—	—
5.0		PDT-DE	−30.34	29.30	0.108
10	623	IIGA [12]	−32.44	34.75	0.0569
10		PDT-DE	−33.60	34.33	0.06
15	1302	IIGA [12]	−32.96	37.49	0.0388
14.64		PDT-DE	−34.63	37.38	0.04
20	2256	HS [16]	−34.08	39.66	0.0296
20		PDT-DE	−36.33	39.54	0.032
25	3465	IIGA [12]	−33.64	41.37	0.0236
24.78		PDT-DE	−35.58	41.19	0.024

4. Conclusion

The proposed method is capable of achieving UECRA with lower PSL than the published reports, and the loss of directivity can be neglected. Not only that, it has the advantage

of easy encoding with respect to IIGA. Therefore, the PDT-DE provides an effective way for the synthesis of UECRA with aperture sizes ranging from small to large scale. Furthermore, by some modifications, the method can also be extended for the sidelobe suppression of sparse linear arrays.

Data Availability

The data used to support the findings of this study are available from the corresponding author upon request.

Conflicts of Interest

The authors declare that they have no conflicts of interest.

Acknowledgments

This work was supported in part by the National Natural Science Foundation of China under Grant nos. 61601272, 61772398, and 61972239, Key Research and Development Program Projects of Shaanxi Province under Grant no. 2019SF-257, Scientific Research Plan of Shaanxi Provincial Education Department under Grant no. 19JK0175, and Scientific Research Plan of Shaanxi University of Technology under Grant no. SLGRCQD2009.

References

[1] H. EI-Kamchouchi, "Ultra-low-sidelobe-level concentric-ring-array pattern synthesis using Bessel neural networks," *IEEE Antennas and Propagation Magazine*, vol. 52, no. 4, pp. 102–105, 2010.

[2] M. Carlin, G. Oliveri, and A. Massa, "Hybrid BCS-deterministic approach for sparse concentric ring isophoric arrays," *IEEE Transactions on Antennas and Propagation*, vol. 63, no. 1, pp. 378–383, 2015.

[3] P. Angeletti, G. Toso, and G. Ruggerini, "Array antennas with jointly optimized elements positions and dimensions part II: planar circular arrays," *IEEE Transactions on Antennas and Propagation*, vol. 62, no. 4, pp. 1627–1639, 2014.

[4] R. Willey, "Space tapaering of linear and planar arrays," *IRE Transactions on Antennas and Propagation*, vol. 10, no. 4, pp. 369–377, 1962.

[5] T. A. Milligan, "Space-tapered circular (ring) array," *IEEE Antennas and Propagation Magazine*, vol. 46, no. 3, pp. 70–73, 2004.

[6] O. M. Bucci and S. Perna, "A deterministic two dimensional density taper approach for fast design of uniform amplitude pencil beams arrays," *IEEE Transactions on Antennas and Propagation*, vol. 59, no. 8, pp. 2852–2861, 2011.

[7] Y. Jiang and S. Zhang, "An innovative strategy for synthesis of uniformly weighted circular aperture antenna array based on the weighting density method," *IEEE Antennas and Wireless Propagation Letters*, vol. 12, pp. 725–728, 2013.

[8] A. F. Morabito and P. G. Nicolaci, "Optimal synthesis of shaped beams through concentric ring isophoric sparse arrays," *IEEE Antennas and Wireless Propagation Letters*, vol. 16, pp. 979–982, 2017.

[9] A. Kedar, "Deterministic synthesis of wide scanning sparse concentric ring antenna arrays," *IEEE Transactions on Antennas and Propagation*, vol. 67, no. 12, pp. 7387–7395, 2019.

[10] R. L. Haupt, "Optimized element spacing for low sidelobe concentric ring arrays," *IEEE Transactions on Antennas and Propagation*, vol. 56, no. 1, pp. 266–268, 2008.

[11] K.-S. Chen, Y.-Y. Zhu, X.-L. Ni, and H. Chen, "Low sidelobe sparse concentric ring arrays optimization using modified GA," *International Journal of Antennas and Propagation*, vol. 2015, pp. 1–5, 2015.

[12] Y. Jiang, S. Zhang, Q. Guo, and M. Li, "Synthesis of uniformly excited concentric ring arrays using the improved integer GA," *IEEE Antennas and Wireless Propagation Letters*, vol. 15, pp. 1124–1127, 2016.

[13] D. Bianchi, S. Genovesi, and A. Monorchio, "Constrained pareto optimization of wide band and steerable concentric ring arrays," *IEEE Transactions on Antennas and Propagation*, vol. 60, no. 7, pp. 3195–3204, 2012.

[14] O. M. Bucci and D. Pinchera, "A generalized hybrid approach for the synthesis of uniform amplitude pencil beam ring-arrays," *IEEE Transactions on Antennas and Propagation*, vol. 60, no. 1, pp. 174–183, 2012.

[15] X. Zhao, Q. Yang, and Y. Zhang, "A hybrid method for the optimal synthesis of 3-D patterns of sparse concentric ring arrays," *IEEE Transactions on Antennas and Propagation*, vol. 64, no. 2, pp. 515–524, 2016.

[16] Y. Jiang, S. Zhang, Q. Guo, and X. Luan, "A hybrid strategy based on weighting density and genetic algorithm for the synthesis of uniformly weighted concentric ring arrays," *IEEE Antennas and Wireless Propagation Letters*, vol. 16, pp. 186–189, 2017.

[17] G. Sun, Y. Liu, Z. Chen, S. Liang, A. Wang, and Y. Zhang, "Radiation beam pattern synthesis of concentric circular antenna arrays using hybrid approach based on cuckoo search," *IEEE Transactions on Antennas and Propagation*, vol. 66, no. 9, pp. 4563–4576, 2018.

[18] L. Wang, X.-K. Wang, G. Wang, and J.-K. Jia, "A two-step method for the low-sidelobe synthesis of uniform amplitude planar sparse arrays," *Progress In Electromagnetics Research M*, vol. 86, pp. 153–162, 2019.